Using Transient Computational Analysis to Aid Microwave Ablation Device Design for Liver Tissue

Prifysgol Abertawe
Swansea University

Faculty of Science and Engineering

Swansea University

Submitted to Swansea University in fulfilment of the requirements of the Degree of Doctor of Philosophy

Dale Kernot

January 1, 2025

Abstract

Microwave ablation (MWA) therapy, a minimally invasive approach utilizing electromagnetic waves to induce cytotoxic temperatures within tumors, is the focus of this thesis. This thesis gives a comprehensive background of the theory underpinning established computational models and uses these models to perform a novel comparative analysis of various 2D MWA probe designs and to explore the efficacy of internally cooled probes. The aim is to enhance the knowledge of MWA by providing a detailed understanding of probe-tissue interactions.

The initial segment of the research uses a two-dimensional axisymmetric finite element model to systematically examine different MWA probe geometries. This study specifically addresses the changes in dielectric properties of tissues at elevated temperatures and their impact on the thermal and electric field distributions. Highlighting the importance of their consideration in modelling of MWA and the transient influence they have on the shape and size of ablation fields.

The second part of the thesis presents a detailed parametric study of internally cooled MWA probes. This study examines the effects of coolant system configuration, including the internal position of the cooling system, coolant flow rate, and coolant temperature on the probe's performance. These factors are critically analyzed to determine their influence on maintaining targeted tissue heating, preventing excessive heating, and potential damage to surrounding healthy tissues.

This thesis demonstrates the creation of a custom multiphysics model for microwave ablation, developed using the open-source NGSolve software. This approach enabled precise modeling of complex probe-tissue interactions, illustrating the power of open-source tools in advancing medical device research.

Declaration

This work has not previously been accepted in substance for any degree and is not being concurrently submitted in candidature for any degree.

Signed: Dale Kernot - [redacted]
Date: 01/01/2025

This thesis is the result of my own investigations, except where otherwise stated. Other sources are acknowledged by footnotes giving explicit references. A bibliography is appended.

Signed: Dale Kernot - [redacted]
Date: 01/01/2025

I hereby give consent for my thesis, if accepted, to be available for electronic sharing.

Signed: Dale Kernot - [redacted]
Date: 01/01/2025

The University's ethical procedures have been followed and, where appropriate, that ethical approval has been granted.

Signed: Dale Kernot - [redacted]
Date: 01/01/2025

Dale Kernot
January 2025

Acknowledgements

I would like to extend my deepest gratitude to my supervisors, Dr. Raoul van Loon and Dr. Hari Arora, for their invaluable guidance throughout my research journey. Their endless support has been essential, without which I would not have reached this point.

I am also grateful for the general support from those in my personal network who have provided encouragement during this process, especially when it was needed the most.

Additionally, I acknowledge the financial support provided by Olympus Medical Technologies Europe and the Welsh Government, which was instrumental in the completion of my studies.

Lastly, I dedicate this achievement to my family, who have always believed in me. To my parents, this is for you.

Peer-reviewed papers published during PhD candidature

D. Kernot, J. Yang, N. Williams, et al. Transient changes during microwave ablation simulation : a comparative shape analysis. Biomech Model Mechanobiol (2022). https://doi.org/10.1007/s10237-022-01646-6

Conference contributions during PhD candidature

D. Kernot, T. Thomas, T.H.J. Yang, D.N. Williams, P. Ledger, H. Arora, R. van Loon, Axisymmetric modelling of microwave ablation in biological tissue, UKACM, Loughborough, 2021 - Conference contribution
https://doi.org/10.17028/rd.lboro.14588538.v1

D. Kernot, T. Thomas, T.H.J. Yang, D.N. Williams, P. Ledger, H. Arora, R. van Loon, Modelling and shape analysis of microwave ablation, BioMedEng21, Sheffield, 2021 - Presentation

Contents

List of Figures

List of Tables

Nomenclature

Variable Summary		
Symbol	Name	Unit
Electromagnetic Variables		
$\mathbf{D}$	Electric flux density	$C.m^{-2}$
$\mathbf{B}$	Magnetic flux density	$Wb.m^{-2}$
$\mathbf{E}$	Electric field	$V.m^{-1}$
$\mathbf{H}$	Magnetic field	$A.m^{-1}$
$\mathbf{J}$	Current density	$A.m^{-2}$
ρ	Charge density	$C.m^{-3}$
ε	Electrical permittivity	$F.m^{-1}$
μ	Electrical permeability	$H.m^{-1}$
ω	Angular frequency	$rad.s^{-1}$
σ	Electrical conductivity	$S.m^{-1}$
j	Imaginary unit	-
k_0	Free space wavenumber	m^{-1}
$\mathbf{n}$	Surface normal vector	-
Thermal Variables		
ρ_l	Mass density	$kg.m^{-3}$
C_l	Specific heat capacity	$J.kg^{-1}.K^{-1}$
k_l	Thermal conductivity	$W.m^{-1}.K^{-1}$
$\varepsilon_r(T)$	Temperature-dependent relative permittivity	-
$\sigma(T)$	Temperature-dependent conductivity	$S.m^{-1}$
Q_p	Heat loss due to perfusion	$W.m^{-3}$
Q_{SAR}	Heat source from electromagnetic absorption	$W.m^{-3}$
Q_m	Metabolic heat source	$W.m^{-3}$
T	Temperature	K or $°C$
T_b	Blood temperature	K or $°C$
Geometric and Computational Parameters		
h	Mesh element size	m

Variable Summary		
Symbol	Name	Unit
p	Polynomial order	-
γ_0	Propagation constant for TEM mode	m^{-1}
Physical Constants		
c	Speed of light	$m.s^{-1}$
ε_0	Permittivity of free space	$F.m^{-1}$
μ_0	Permeability of free space	$H.m^{-1}$

List of Acronyms

BMI	Body Mass Index
RFA	Radiofrequency Ablation
RF	Radiofrequency
ILT	Interstitial Laser Thermotherapy
MWA	Microwave Ablation
MRI	Magnetic Resonance Imaging
CT	Computed Tomography
HIFU	High Intensity Focused Ultrasound
HCC	Hepatocellular Carcinoma
FEM	Finite Element Method
CFD	Computational Fluid Dynamics
SAR	Specific Absorption Rate
EM	Electromagnetic

1 Introduction

1.1 Background

In 2020, nearly 10 million deaths were caused by cancer worldwide, making it one of the largest killers globally [3]. Cancer can be defined broadly as a group of diseases characterised by abnormal cell growth within the body, that has the potential to spread from its origin. This divergence from ordinary cell proliferation to a state of uncontrolled growth can lead to the formation of lumps of tissue called tumours. Cancer has the potential to arise in most parts of the body and can cause serious symptoms or death. While many types are now treatable to some degree, the most common cancers leading to death are those of the lung (1.8 million), colon and rectum (904 thousand), liver (758 thousand), breast (666 thousand), and stomach (660 thousand).

The global burden of cancer is heavily influenced by a range of modifiable risk factors. The leading risk factors that contribute to cancer deaths include smoking, alcohol use, and high BMI [4]. Avoiding action can be taken to limit exposure to such factors, and in turn lower the risk of developing cancer, however for patients that do develop the disease a treatment is highly sought after. Therapeutic approaches include surgical resection, chemotherapy, radiotherapy, drug targeted therapy, to name a few [5]. The global prevalence of cancer maintains the drive to seek new and ever-improving treatment methods that can yield a positive outcome for patients.

Although established treatments such as Radiotherapy and Chemotherapy can prove successful in certain cases [6], currently in medicine, after diagnosis of a focal tumour the most common method of treatment is the surgical removal of the diseased tissue. However, this open surgery can often bring adverse effects which, in some instances, lead to the medical risks outweighing the benefits of tumour removal. Surgery can be traumatic, often requiring a hospital stay followed by a period of rehabilitation and recovery along with the probable need for anaesthetic during the procedure [7, 8, 9]. Furthermore, research has suggested that the surgical removal of tumours can inadvertently create an environment whereby the process of metastasis could be accelerated [10, 11]. In addition

to these risks, the cost of open surgery is relatively high and consequently, there has been a drive to seek alternative therapeutic methods that are both cost-efficient and effective.

1.2 Thermal ablation

One particular branch of cancer treatment is localized ablation therapy, a minimally invasive procedure characterized by small incisions or injections to access the tumour site, significantly reducing tissue trauma compared to traditional surgery [12]. This technique uses targeted cytotoxic temperatures to induce cell necrosis and death within tumours. These cytotoxic temperatures typically range between -40°C to -196°C for cryoablation and 50°C to 100°C for thermal ablation, depending on the method used [13, 14]. Cell death is influenced not only by the absolute temperatures reached but also by the duration of exposure to these temperatures. These temperatures, which may be either hypothermic or hyperthermic, are precisely focused on the tumour and a portion of the surrounding healthy tissue, forming what is known as a 'resection margin', which is the boundary of normal tissue around the tumour that is also treated to ensure complete cancer eradication [15, 16]. Unlike surgical procedures that involve the physical removal of diseased tissue, ablation techniques destroy cancer cells and leave them in situ. Following treatment, the dead tissue undergoes a process called 'resorption', where it is gradually broken down and assimilated or expelled by the body's immune system over the subsequent months [17]. Thermal ablation techniques can initiate immune responses by exposing tumour antigens, leading to systemic anti-tumour effects that may target distant metastases [18]. However, these effects are often not robust enough to prevent tumour recurrence on their own.

Additionally, the use of advanced imaging and computational tools not only enhances the precision and efficacy of ablation treatments but also significantly reduces the risk of complications. These complications, often seen in conventional surgery, such as infections, significant bleeding, and prolonged hospital stays, are notably diminished in ablation therapies. For instance, ablation avoids large surgical incisions, thereby reducing the risk of surgical wound infections and postoperative haemorrhaging. Moreover,

the precision of thermal ablation minimizes damage to surrounding healthy tissues, lowering the incidence of adverse effects related to tissue damage [19].

The potential advantages gained with procedures of this kind lie in their percutaneous nature, reducing recovery times and cost in comparison to open surgery [7]. Within the hyperthermic branch of ablation therapy, multiple methods for heat generation and delivery have developed. These include Radiofrequency ablation (RFA), Interstitial Laser Thermotherapy (ILT), Microwave ablation (MWA), and High-Intensity Focussed Ultrasound (HIFU) ablation [20]. These all provide heat to the focal area however the mechanisms of generation and delivery are different. RFA is the most common modality but has some limitations that the MWA therapy has the potential to overcome. These types of ablation will be explored in more detail in the following section, along with a hypothermic approach - cryoablation therapy.

1.3 Ablation Modalities

1.3.1 High Intensity Focussed Ultrasound

Similarly to how a microscope can be used to focus sunlight on a particular spot, HIFU involves using an acoustic lens to focus ultrasonic sound waves to a particular target volume within the body, creating a point of increased wave intensity whereby the pressure generates heat at the focal point [21].

Imaging techniques such as ultrasound or MRI are necessary throughout the procedure for monitoring the accuracy of the focal point to the target tissue. Though potentially beneficial due to the relative abundance of existing ultrasound equipment within medicine, HIFU is limited by the types of tissue suitable for treatment since hard tissues such as bone with high acoustic attenuation characteristics, and empty cavities containing air impede the travel of the ultrasound waves. Nevertheless, research for using HIFU in the application of treatment of prostate cancer is advanced [22], and holds potential for treatment of other types of such as rectal, cervical, pancreatic, and breast cancer.

1.3.2 Cryoablation

Cryoablation differs from the other modalities mentioned as it is a hypothermic treatment. Typically involving the use of hollow, needle-like cryoprobes, that are inserted percutaneously directly into malignant tissue under imaging guidance. Once correctly located, cooled fluids or gases such as liquid nitrogen[23], or compressed argon[24], can be circulated through the probe's internal structure. Due to the temperature and thermally conductive nature of the chosen cooling fluid, freezing temperatures are created in a region surrounding the probe, therefore freezing the diseased tissue [25].

If the tissue is frozen, ice crystals within the cells themselves cause damage to the cell membrane and hence, kill the cells. If tissue is not frozen, however, death can still be initiated by the lower temperatures through coagulation of blood that would otherwise be supplying the cells, or by inducing cell apoptosis through the stressful conditions [26]. Cryoablation is particularly effective for liver and kidney tumours due

to the organs' ability to tolerate the freezing process [27, 28]. It is also used for lung tumours where real-time monitoring of ice formation can ensure safety around critical vascular structures [29]. Additionally, cryoablation is beneficial for prostate and breast cancers due to its minimally invasive nature [30, 31, 32]. However, limitations exist for tumours less sensitive to cold or near large blood vessels where the risk of damaging these structures can outweigh benefits [33].

1.4 Electromagnetic properties of biological tissues

Understanding the electromagnetic properties of biological tissues is fundamental for their application in fields ranging from diagnostic imaging to therapeutic treatments like RFA and MWA, therefore it is necessary to discuss these before moving on to the electromagnetic ablation modalities. These interactions are primarily governed by the dielectric properties of the materials.

The dielectric properties of a material, such as permittivity (ε) and permeability (μ), explain how the material interacts with electromagnetic fields. These properties are complex and frequency-dependent, and can be expressed in complex form to account for the phase differences between the applied field and the material response:

$$\varepsilon = \varepsilon' - j\varepsilon'',$$
$$\mu = \mu' - j\mu''.$$

Here, ε' and μ' represent the real parts that indicate the capacity of the material to store electric and magnetic energy, respectively. Whilst ε'' and μ'', are the imaginary parts, corresponding to the dissipation of energy within the material, primarily as heat. In biological tissues, permeability (μ) is often approximated to that of free space (μ_0) and therefore does not influence the magnetic field [34]. However, the complex permittivity (ε) plays a significant role.

To help conceptualise this in the context of biological tissue, the complex permittivity of tissues is analogous to a lossy capacitor. Ideal capacitors store and release electrical energy without losses. However, real (lossy) capacitors, like biological tissues, dissipate energy as heat due to the imaginary part of permittivity (ε''). The

imaginary part of permittivity relates closely to the tissue's electrical conductivity (σ), which quantifies how electromagnetic wave energy is converted into heat. A non-zero conductivity in biological tissues implies significant energy absorption [35]. This principle is crucial for applications such as RFA or MWA, where controlled heating is required.

The real part of complex permittivity (ε'), often referred to as ε_r in scientific contexts, represents the capacity of a material to store electrical energy. It quantifies how much energy can be held in the electric field of the material relative to a vacuum, which is the free space permittivity (ε_0). This storage capability is crucial because it determines how effectively the material can interact with and respond to electromagnetic fields without directly contributing to energy loss.

Understanding how tissue responds under varying frequencies of electromagnetic signals is essential for applications like ablation modalities. This interaction is modelled using the Cole-Cole model, an enhancement of the simpler Debye model designed to address the complex patterns by which material dipoles return to equilibrium after being disturbed—a process known as "relaxation behaviours"[36]. The Cole-Cole model adeptly captures how permittivity, which measures a material's reaction to an electric field, varies with frequency. This phenomenon, termed dispersion, is crucial for understanding tissue interactions with electromagnetic fields.

To quantitatively describe how permittivity changes with frequency, the mathematical representation of the Cole-Cole model [37] is:

$$\varepsilon(\omega) = \varepsilon_\infty + \frac{\varepsilon_s - \varepsilon_\infty}{1 + (i\omega\tau)^\alpha} \tag{1.1}$$

where $\varepsilon(\omega)$ represents the frequency-dependent permittivity, ε_∞ is the high-frequency limit of permittivity, ε_s is the static permittivity at zero frequency, ω is the angular frequency, τ is the characteristic relaxation time, and α ($0 \leq \alpha < 1$) is a dimensionless parameter that modifies the sharpness of the relaxation spectrum, reflecting the distribution of molecular relaxation times within the tissue[37, 36].

Empirical studies presented in [38, 39] validated the Cole-Cole model's applicabil-

ity, providing detailed insights into how dispersion varies across different biological tissues over a broad frequency range from 10 Hz to 20 GHz. Using measurement methodologies such as network analyzers to assess signal transmission and reflection, this research has meticulously mapped how permittivity changes across alpha, beta, gamma, and delta dispersion regions. This work not only confirms the model's relevance but also highlights the unique biological processes associated with each dispersion type, thereby enriching our understanding of tissue interactions with electromagnetic fields.

Dispersion behaviours reflect the complex interactions between electromagnetic fields and tissue constituents, notably water molecules and ions. Each dispersion region is linked to specific biological and physical processes:

- **Alpha dispersion** occurs below 100 kHz, associated with interfacial polarization at cell membranes.
- **Beta dispersion** spans from 100 kHz to 100 MHz, arising from the polarization of cellular components smaller than the cell membrane.
- **Gamma dispersion**, significant at frequencies above 1 GHz, stems from the orientation polarization of water molecules. This region is especially pertinent to MWA, which operates at frequencies like 900 MHz and 2.45 GHz.
- **Delta dispersion**, within the microwave range, relates to the relaxation of free water molecules, critical for the MWA process.

Gabriel's work also specifically addresses the parametric models developed to encapsulate these dispersion behaviours, based on extensive empirical data. These models provide a structured representation of tissue dielectric properties, highlighting the crucial role of molecular and ionic processes across the four dispersion regions [40].

For MWA frequencies of 900 MHz and 2.45 GHz, gamma and delta dispersions are particularly important. Research presented in [40] demonstrates how varying tissue compositions—distinguished by different contents of water molecules—affect dielectric properties through these dispersion behaviours. Specifically, tissues with a high content of free water predominantly exhibit delta dispersion at these frequencies, influencing

the relative permittivity and, consequently, the efficiency of energy absorption crucial for MWA's effectiveness. Conversely, tissues characterized by higher concentrations of bound water or denser cellular structures are more influenced by gamma dispersion. This variation in dispersion behaviour directly impacts the dielectric properties of tissues, leading to distinct energy absorption patterns during MWA, thereby affecting the ablation efficacy and precision across different tissue types [41].

In the context of varying dielectric properties across different tissue types, [42] provides valuable insights into the impact of fat layers on MWA outcomes. The research showed that fat layers can significantly modify the size and shape of the ablation zone, by acting as a barrier and reflector of electromagnetic energy, due to the difference in dielectric properties between tissue types. Furthermore, [43] investigates how respiratory movements affect MWA's effectiveness in lung cancer treatment. The study reveals that changes in lung tissue's dielectric properties during breathing significantly alter power dissipation and temperature distribution.

It is important also to account for the highly temperature-sensitive nature of biological material. Data on the linear temperature dependence of dielectric properties up to 70 °C across a frequency range of 0.5 to 20 GHz were provided in [44], but this work also highlighted the limitation of linear models, especially at temperatures approaching 70 °C, a point commonly exceeded in MWA procedures. It was shown in [45] that it is feasible to measure tissue dielectric properties during thermal ablation, highlighting the severe changes that occur as temperatures approach 100 °C. This work involved embedding an open-ended coaxial probe within a piece of tissue, measuring the reflection coefficient with a vector network analyser, and computing the dielectric properties from these values. This work laid the groundwork for considering dynamic changes in tissue properties in simulation models.

Building upon these foundational studies, Ji and Brace took a significant step forward by measuring the dielectric properties of liver tissue during high-temperature microwave heating and incorporating these measurements into a novel sigmoidal model

[46]. Their approach acknowledges the rapid and non-linear changes in tissue properties at temperatures above 70 °C, particularly near the critical 100 °C mark where tissue undergoes substantial structural changes and water loss through evaporation, which is responsible for the decrease in dielectric properties [44, 47]. This work underscores the complexity of thermal ablation processes and the necessity of incorporating dynamic changes in tissue properties into simulation models [48].

Understanding and accurately modelling these properties are therefore paramount in optimizing MWA strategies.

1.5 Radiofrequency ablation

Given the focus of this thesis on MWA, it is logical to begin by exploring RFA in detail. Although RFA has demonstrated certain limitations not present in MWA — each method with its unique challenges — it serves as an important context for understanding the advancements and distinctions of the microwave technique.

To begin, D'Arsonval described how a tissue became warmed when a radio frequency alternating current was passed through it to complete a closed circuit between the RF generator and the tissue, the warming occurred without stimulation of the neuromuscular system [9]. This became the foundation on which electrosurgery grew, the first significant tool being the development of the Bovie knife, a surgical instrument that uses electrical energy in the form of a radio frequency alternating current for cutting and cauterization of tissue. Cutting is achieved by maintaining a near-constant current and cauterization by a pulsing current [49]. Subsequently, this technique laid the groundwork for the development of RFA treatments.

In RFA, a radiofrequency current typically between 350 – 500 kHz is applied through the patient to complete an electrical circuit. This setup involves two electrodes: an active electrode at the end of an insulated probe and a grounding pad on the patient's skin. RF ablation systems typically start at lower power settings around 40 watts and can provide power up to 200 watts, ensuring adequate tissue heating without

immediate tissue charring. Power is adjusted based on tissue impedance to optimize the heating effect [50]. The grounding pads facilitate the return of the RF current, ensuring effective energy delivery across the targeted area [51, 52].

Before inserting the RF probe, surgical preparation typically involves the use of imaging guidance, such as ultrasound, CT, or MRI, to accurately position the probe. A small incision or puncture is made at the site where the probe is to be inserted. Local anaesthesia is applied at the insertion site to minimize discomfort, and in some cases, conscious sedation may be used, similar to other interventional radiology procedures [50].

The heating in RFA results from the motion of charged molecules, particularly ions, within the tissue. When the RF current is applied, it induces ionic agitation in the tissues immediately surrounding the active electrode. The chosen frequency range of 350 to 500 kHz is crucial for several reasons. Firstly, at this frequency range, the ionic movement is most effective for generating heat due to resistive (ohmic) losses. This is because the ion oscillation matches the rate at which energy can be efficiently absorbed and converted into heat. Secondly, this frequency is high enough to avoid neuromuscular excitation, which can occur at lower frequencies, thus preventing any unintended muscle contractions or nerve stimulation during the procedure [53].

Moreover, frequencies outside this optimum range result in less effective heating. At lower frequencies, the ion movement is not rapid enough to produce sufficient thermal energy, leading to ineffective tissue ablation. At higher frequencies, the electrical current may pass through the tissue too quickly, reducing its interaction with the ions and consequently diminishing the heat generated [52].

This method of heating elevates tissue temperatures to therapeutic levels, effectively targeting the desired area without direct heating from the probe itself. This ensures that the ablation is both precise and confined to the intended treatment zone. A visual representation of ion movement under RF current is provided in Fig 1.1. Besides thermal effects, RF ablation may also cause non-thermal effects, such as electroporation,

where the electric field increases the permeability of the cell membrane, potentially leading to cell death without significant temperature increases.

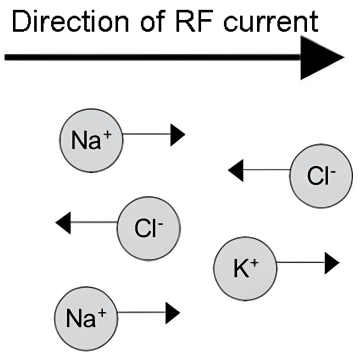

Figure 1.1: The Ionic movement caused in the presence of the radio frequency current during an RF ablation, causing frictional heating of the tissue. Reprinted from Biophysics of Radiofrequency Ablation, by Haemmerich, Dieter. in Critical reviews in biomedical engineering, 38, 53-63 (2010) [52].

By this process, the tissue in the focal area of the probe can be damaged through heating, but it is necessary to avoid this effect at the point where RF current exits the body, at the surface grounding pads. Their relatively large surface area and use of multiple pads ensure the energy flux at the contact surface is sufficiently low as to not cause heating to such a level that skin burns occur, however, this does still happen, and skin burns are one of the limiting factors in the amount of power (typically in the region of 40-80W) that can be used during RFA procedures [54].

Effectively, the body makes the link to form a closed system between the ablation probe inserted in the focal area for ablation and the grounding pads on the patient's skin. This is illustrated in Fig 1.2.

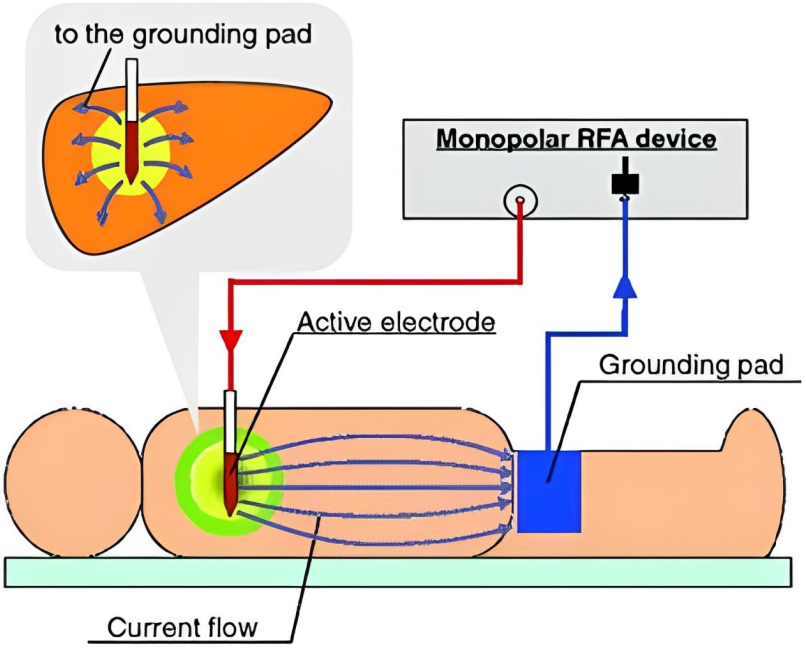

Figure 1.2: A diagram showing the elements involved in RF ablation using a monopolar device, where the grounding pads are typically placed on the patient's thighs. Reprinted from "Clinical effectiveness of bipolar radiofrequency ablation for small liver cancers," as presented in [55].

RFA is the most frequently used modality of thermal ablation worldwide, due to its effectiveness at destroying the targeted tumour tissue, accompanied by a low level of complication [56]. It also comes with relatively low technical demand when compared to the methods of Cryoablation or laser ablation [57].

However, this modality does come with its drawbacks, a limitation of the RFA process is its dependency on the thermal and electrical conductivity of the tissue, good conductivity of both is required for effective ablation. Application of a high level of power too quickly to the tissue can cause desiccation around the active tip of the probe, desiccated or charred tissue has poor conductivity so the probe is effectively insulated from transmission of radiofrequency energy into the tissue, preventing any further ablation from being completed. This is also true of water vapour, which can be created due to high temperatures near the RFA probe [58]. As such, it is important to achieve the correct temperature but also the correct exposure time in RF ablation therapy. A slower and calculated energy deposition can be more effective at enlarging

a tissue ablation than a fast temperature rise. The temperature ranges used can vary between 65 and 100°C [59, 60].

Figure 1.3 shows the variation caused by a slow versus fast temperature rise in the target tissue. It can be seen that the slower deposition of energy yields a larger ablated area before desiccation occurs, compared to the fast deposition where desiccation begins earlier, limiting the outer boundary of hyperthermia.

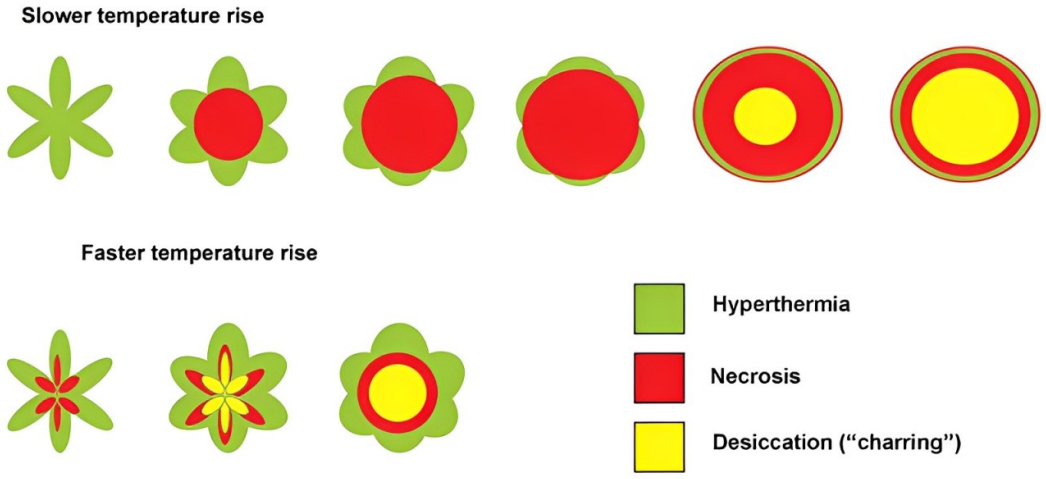

Figure 1.3: A comparison of different heating rates. Reprinted from Radiofrequency ablation: Mechanism of action and Devices, by Kelvin Hong and Christos Georgiade in Journal of Vascular and Interventional Radiology, Volume 21, Issue 8, Pages S179-S186, (2010) [51].

To navigate these challenges, temperature control during the procedure is important to limit vaporization or charring of tissue. The energy applied from the generator must be varied to achieve this, employing methods such as power control, temperature control, and impedance control. Power control adjusts the voltage to the applicator in such a way as to keep the RF power constant. Temperature control, on the other hand, uses one or more temperature sensors such as thermocouples or thermistors, integrated into the applicator near the active tip. The feedback from the temperature sensors enables modulation of power in order to control the measured temperature in the tissue [59]. Impedance control measures the tissue impedance as ablation takes place, this

measurement takes place between the active electrode and the grounding pad. An increase in impedance, indicative of vaporizing tissue, triggers a reduction in power until impedance stabilizes, allowing for the reapplication of power at a lower level. This is an automated process built into some devices, such as the resistance-controlled automatic power (RCAP) system in CELON Power generators for example [61]. The resulting power and impedance are shown in Fig 1.4. Moreover, innovations such as

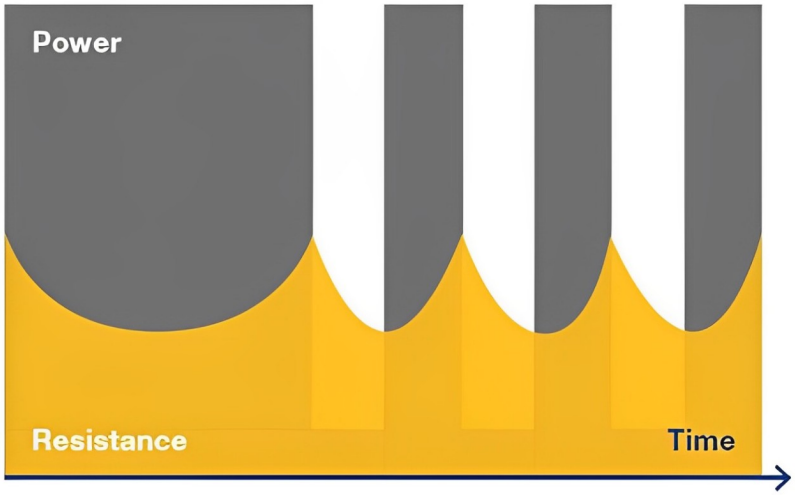

Figure 1.4: An illustration that conceptualises the power against time balance for applicators with impedance monitoring and adjustment. An increase in impedance would be suggestive that water vapour is being created, but this vapour will disperse or recondense, thus the impedance reduces again and power application can be resumed. Reprinted from Olympus Europa, available at: www.olympus-europa.com/medical/en/Products-and-Solutions/Products/Product/CELON-Power-System.html, accessed in Nov 2018.

cooling the probe to slow heating immediately around it [62], or perfusing the tissue with an electrically conducting fluid from the probe itself [63], have been developed to mitigate issues of charring and maintaining conductivity.

There is considerable heterogeneity in heat deposition through tissue under RFA due to the variability of vasculature within the tissue. The size of the ablated area hinges on the balance between the energy deposited into the local tissue via the ablation probe and the energy dissipated due to cooling effects, notably the 'heat sink' effect from nearby blood vessels. This heat-sink effect, where blood flow in adjacent vessels

larger than 3mm limits significant temperature changes in nearby tissue [64], thus keeping it 'cooler', poses a challenge to the efficacy of all hyperthermic thermal ablation techniques. Consequently, this dynamic can limit the ablation's reach, potentially leaving viable tumour cells close to the vessel wall and raising the risk of subsequent tumour progression[65]. Since this effect can lead to insufficient ablation with an individual probe and a single dose of treatment, a larger volume of necrotic tissue can be made by using multiple probes arranged in an array, whose ablated regions overlap to result in an overall larger ablation [66, 67]. Alternatively, other techniques have in some cases regulated the blood flow to the tissue region where ablation is to be carried out, thus reducing or removing the heat sink associated with blood flow for a period during RFA application [68, 69].

Other factors which can influence the likelihood of tumour progression after RF ablation are tumour-related, such as the size, location, and orientation along with the organ it lies within. Technical factors like the power setting, time, and electrodes used can also be important factors in ablation success [70, 71, 54]. Precise placement of the ablation probe into the target tissue is essential in creating the correct ablation volume, as such the guidance of the needle-like RFA applicators is monitored and checked by imaging systems. Most commonly, ultrasound or non-contrast CT imaging is used because of its sufficient detection of both the applicator probe and the lesion created by treatment. Neither, however, can exactly show the ablated margin during the treatment [72]. Alternatively, MRI along with temperature-sensitive imaging could be used if accompanied by specialized equipment that is compatible with the MRI scanner, but this is more expensive. A typical scan from an ablation procedure is shown in Fig 1.5.

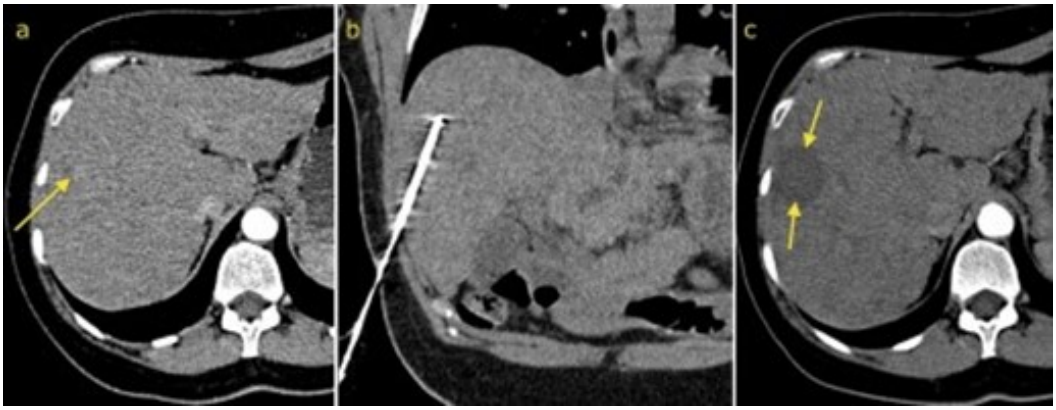

Figure 1.5: CT scans from before (a), during (b), and after (c) the ablation of a hepatocellular carcinoma. The ablated tissue is clear to see in (c) as the area of lower density. Reprinted from Radiology, St. Vincent's University Hospital at http://www.svuhradiology.ie/case-study/radiofrequency-ablation-hcc/, accessed in Nov 2018 [73].

2 Microwave ablation

In this chapter we will discuss Microwave ablation therapy, its mechanism of action, advantages and disadvantages compared to other techniques, and the approaches used to model this ablation modality, setting the scene for the research carried out in this thesis.

2.1 Microwave ablation mechanism

Microwaves, occupying the frequency range of the electromagnetic spectrum from 300 MHz to 300 GHz [74], are used in MWA to treat various medical conditions. Unlike RFA, where tissue heating is achieved through the flow of electrical current resulting in resistive heating, MWA utilizes electromagnetic fields. This method employs the phenomenon of dielectric hysteresis to generate heat within the tissue, subsequently causing cellular damage and tissue ablation [75].

Dielectric hysteresis in MWA refers to the delayed response of polar molecules, such as water, to the rapidly alternating electromagnetic field generated by microwave frequencies, typically 900 MHz or 2.45 GHz. When exposed to microwaves, the electric field within the tissue changes direction rapidly, prompting polar molecules to attempt alignment with each shift in field direction, as illustrated in Fig 2.1. Due to their inherent mass and intermolecular forces, these molecules experience a natural delay or 'lag' in their response, known as dielectric hysteresis.

This lag causes the molecules to be out of sync with the oscillating field, leading to asynchronous molecular movement. As the molecules continuously try to catch up to the field's new orientation, they rub against each other, creating friction. This frictional interaction between molecules, arising from their efforts to reorient with the changing field, converts kinetic energy into thermal energy. The constant molecular motion and resulting friction generate significant heat within the tissue [14].

This heating mechanism is especially effective in tissues rich in water content. Water molecules, being highly polar, are particularly responsive to electromagnetic field

changes, leading to greater frictional heat as they struggle to align with the rapid field oscillations. Furthermore, while the primary mechanism is dielectric heating, ions present in the tissue can still contribute to heating in MWA due to ionic polarisation, where displaced ions collide with other ions, converting kinetic energy into heat. However, this contribution is generally less significant than in RF ablation because the microwave frequencies primarily act on the dipole molecules rather than the free ions [76].

The specific frequencies of 900 MHz and 2.45 GHz employed in MWA are chosen because they fall within the Industrial, Scientific, and Medical (ISM) bands, globally reserved frequency ranges allowed for non-commercial applications, which includes medical devices [77]. This choice helps to minimize interference with other electronic devices and ensures compliance with international regulations.

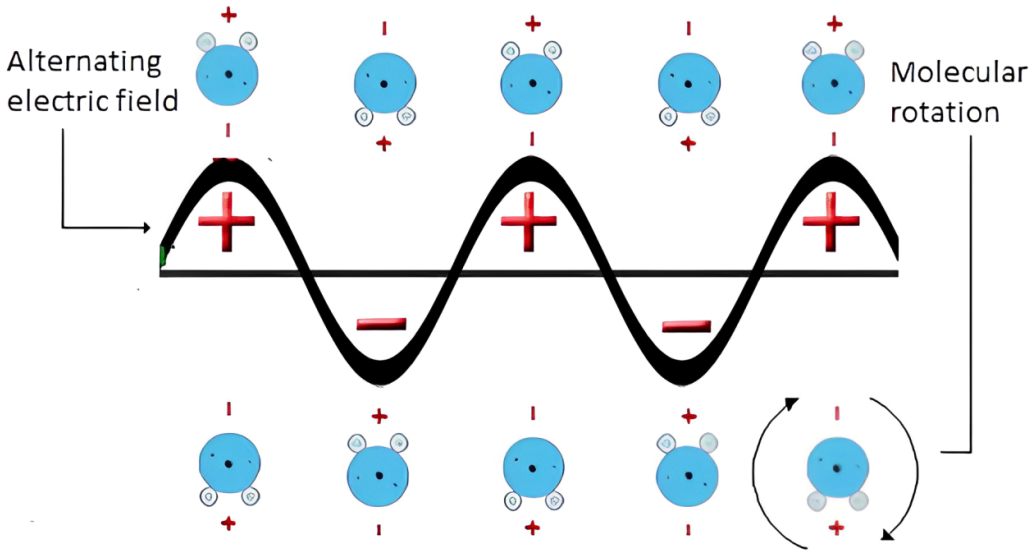

Figure 2.1: The rotation of water molecules in the presence of an alternating electric field. Adapted from Microwave Ablation: Principles and Applications, by Simon, Caroline J. et. al. In RadioGraphics, vol 25, pages S69-S83, (2005) [78].

With the fundamental mechanism of heating established, the question of how to use this physics to heat a specific volume of tissue within the body is now posed. Microwave energy is delivered to the target region through a carefully designed needle-like probe containing a microwave antenna, which is inserted percutaneously into the tumour,

this probe couples electromagnetic energy produced from a generator to the tumour where a volume is heated around the probe, as illustrated in Fig 2.2.

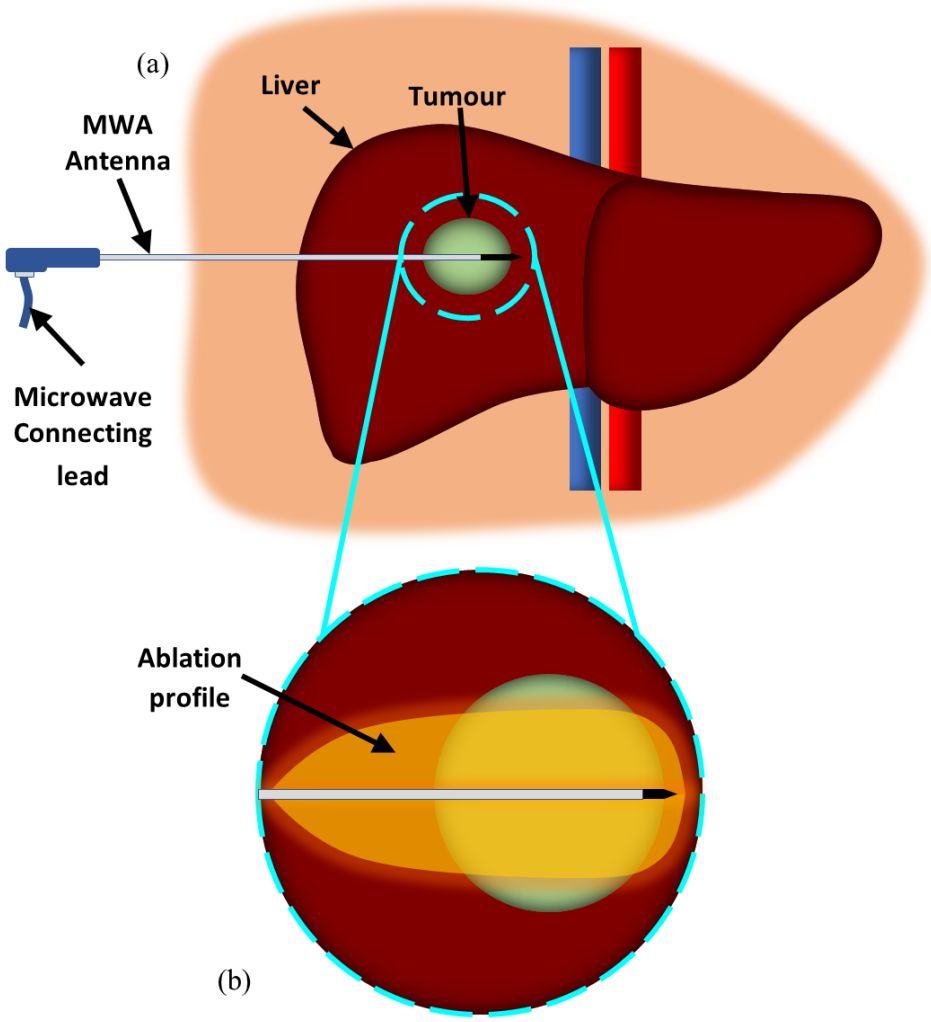

Figure 2.2: A conceptual illustration of MWA treatment. (a) The MWA probe is inserted into the tumour embedded within the liver, treatment can then begin and an ablated area is created from the increased temperature. (b) The shape of this ablation may vary from the target tumour, unceasing the likelihood of collateral damage to neighbouring healthy tissue, or leaving a viable tumour behind.

Typically, a coaxial cable facilitates the transport of energy to the probe from the generator. A coaxial cable is a type of transmission line that excels in carrying high-frequency electrical signals with minimal loss or interference from external signals. The cable is made of an inner conductive wire surrounded by a dielectric material, then a layer of conductive shield followed by an outer plastic insulating sheath. The term

coaxial comes from the fact that both conductive parts of the cable have the same axis. The outer conductor is normally kept at ground potential and the voltage signal is applied through the central conductor. This outer conductor confines the electric and magnetic fields to the dielectric material between the two conductors and therefore little signal loss is observed, in addition, the same shielding occurs for external signals and they are prevented from interfering with the conducted signal.

It is these properties that make coaxial cables an attractive choice for transmitting weak signals that may be largely affected by external interference and also stronger signals that must be contained so as they do not radiate and affect external structures. Largely, MWA probes share the same geometry as the coaxial transmission line discussed here, as can be seen in Fig 2.3. The inclusion of a catheter that encapsulates the coaxial body is crucial not only for hygienic reasons, ensuring sterility during surgical insertion into the body, but also for technical functionality. The catheter is composed of materials specifically chosen for their biocompatibility, inertness, and minimal interference with electromagnetic signal integrity.

For efficiency and safety when carrying the potentially high-power electromagnetic signal, the probe impedance must be correctly selected, with good coupling between components and the target tissue another important consideration to make. The cable and probe structures have a characteristic impedance that is dependent on the dielectric constant of the insulative layer between the two conductors as well as the radii of the inner and outer conductors. Ideally, there would be a seamless transmission of the signal between the transmission cable and the probe structure itself i.e. there would be no reflection of signal at the junction between the two. Reflections occur when a change of impedance is encountered by a propagating wave, therefore, in an effort to match the impedances of both the EM generator, transmission cable, and MWA probe to ensure minimal signal losses through reflection.

Observing the probe itself, instead of the usual coaxial geometry, a short portion of the outer conductor is stripped away around its entire circumference, leaving a break

in the conductor which we will call a *slot*, as illustrated in Fig 2.3[79]. In addition, at the very end of the probe, the coaxial structure terminates by shorting the inner conductor to the outer conductor. The purpose of these two features is to direct the propagation of electromagnetic waves out of the probe and into the surrounding material. When the electromagnetic signal reaches the distal end of the MWA probe, instead of being confined between the two conducting layers it is able to radiate out through the slot, into the catheter, and onwards into the local tissues immediately abutting the catheter surface. This creates an electromagnetic field within the tissue volume, concentrated around the probe slot, that subsequently leads to heating, damage, and ultimately, cellular death.

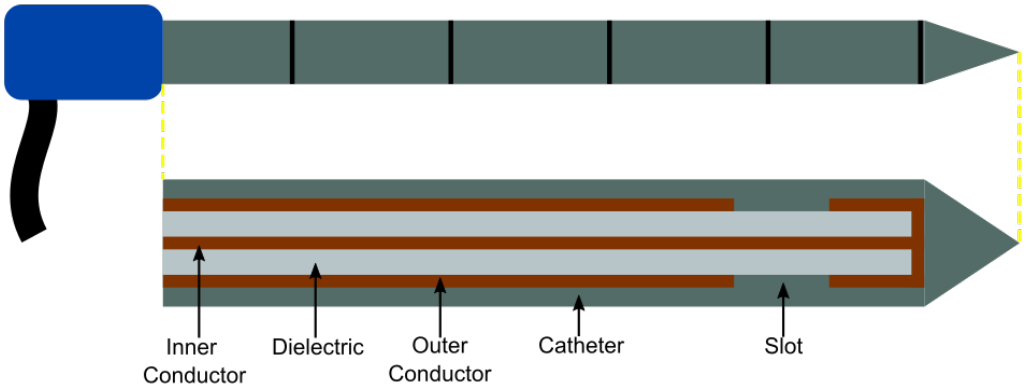

Figure 2.3: The internal structure of MWA probes is typically coaxial with a shorted tip, allowing the microwave signal to radiate into the surroundings via a slot in the outer conductor - this is the antenna part of the device. A biocompatible catheter surrounds the antenna so that the conducting elements are not in contact with the tissue, ensuring hygiene is maintained whilst also allowing the coupling of the electromagnetic signal from the antenna into the tissue. It is, therefore, necessary for the catheter to have similar dielectric properties to the dielectric material within the antenna, to minimise signal reflection at their interface. The material chosen for the catheter is typically Teflon or PTFE [1, 2]. The combination of antenna and catheter will be referred to as the probe.

2.1.1 Benefits of MWA over RFA

Unlike the mechanism governing RFA, electromagnetic energy transmission in MWA relies on the dielectric permittivity and magnetic permeability of the tissue, microwaves are able to propagate through materials even with low electrical conductivity. Charred or desiccated tissue does not limit energy deposition as it does in RFA, therefore enabling temperatures far in excess of 100 °C to be readily achieved without breaking the energy coupling [80, 81, 79, 82]. This is a major advantage in allowing faster ablation with a greater coagulative volume, even in bone and lung tissues that RFA modality is incapable of treating [83].

The higher power deposition possible into the target volume with MWA allows direct and rapid heating that can more readily overcome the effect of heat sinks posed by blood vessels when compared to the RFA modality [65]. As previously mentioned, the RFA technique encounters difficulty in ablation regions around any vessel greater than 3mm in diameter and so runs an increased risk of leaving residual tumour tissue close to the vessel wall if temperatures do not increase sufficiently to ablate the area. MWA can ablate up to and through vessels of this size, allowing larger ablation volumes to be created [84, 85].

Comparative studies between MWA and RFA reveal nuanced advantages of MWA in the treatment of primary liver tumours and hepatic metastasis [85]. To highlight a few, a study underscored MWA's superiority, showing better one- and two-year disease-free survival rates and fewer major complications compared to RFA, particularly for patients with smaller tumours ($\leq$ 3 cm), perivascular tumours, or high recurrence risk [86]. Additionally, another study demonstrated MWA's effectiveness in achieving complete necrosis in early-stage HCC. This is particularly evidenced by the concordance between imaging assessments one month post-ablation and pathological findings post-liver transplantation, highlighting MWA's reliability and its potential as a bridge to transplantation [87]. These studies advocate for MWA's application in managing HCC, emphasizing its utility in clinical scenarios where its benefits of fast and large ablations are most pronounced.

2.1.2 MWA challenges

Although MWA addresses several limitations of RFA, it introduces its own set of challenges.

A significant issue is the characteristically elliptical or tear-drop shaped electric field generated by MWA, which leads to a similar temperature profile - presents a problem if the tumour is spherical in shape [75]. An elliptical or tear-drop shaped ablation area leaves the potential for incomplete heating of the target tumour, or excessive damage to otherwise healthy tissues away from the targeted area, illustrated in Fig 2.2. The shape and extent of heating are directly related to the shape and strength of the electromagnetic field pattern created within the tissue by the ablating probe. As such, the shape of fields created from an MWA probe is a consideration during the design process with reference to the clinical objectives of achieving an ablation profile to match the tumour shape [88, 1, 89, 90, 80, 91, 92, 93].

Another challenge is controlling the rapid temperature increase inherent to MWA, as an uncontrolled ablation risks ineffective treatment of the target tissue or unnecessarily damaging nearby healthy tissue. Furthermore, excessive charring of the tissue in contact with the probe, which can be induced by excessively high temperature, can make probe placement or removal more challenging [94]. It is therefore essential to enable a strong control of the ablation development throughout the treatment, this challenge is compounded by the high sensitivity of tissue properties to temperature [45, 95, 47, 46, 44, 96]. As a result, the expected heating pattern predicted through simulation of constant tissue parameters is not representative of the real-world scenario, where electric field patterns within the tissue can vastly change throughout the procedure due to nonlinear changes in the tissue dielectric properties [75, 46, 45, 42].

Efficient power transfer to the tissue is also crucial, this is typically assessed by calculating the input reflection coefficient of a given probe [97]. A high level of reflec-

tion, caused by differences in material impedance between the probe and the tissue, can cause internal heating of the feed lines and within the probe structure, potentially heating tissue unintentionally or causing structural damage that affects the operation of the device itself.

Achieving a perfect impedance match between the probe and surrounding tissue is impractical, it is therefore expected that substantial power reflection can occur at this junction. As mentioned previously, it is well established in the literature that biological tissue properties relevant to MWA treatment display high levels of temperature dependence, and this extends to the properties that define the impedance of the tissues, therefore wave impedance and in turn the goodness of the impedance match of the probe to its surroundings throughout MWA heating [45, 47].

Moreover, an inherent drawback of using microwave energy for ablation includes challenges in achieving precise treatment due to the 2-4 cm wavelength penetration with the electromagnetic frequencies used, which offer less control compared to techniques with shallower penetration like RFA[74]. This characteristic, coupled with the rapid expansion of the ablation zone, reiterates the need for real-time imaging for accurate monitoring.

2.2 Microwave ablation development and modelling

Having outlined the fundamental challenges faced by MWA treatment, we now focus on the various strategies and technological advancements devised to mitigate these issues. The evolution of MWA therapy is deeply intertwined with advancements in mathematical modelling and simulation techniques, which have played a pivotal role in understanding and overcoming the complex interplay of factors influencing ablation outcomes.

Computational models serve as a bridge between theoretical insights and experimental

validations, shedding light on the electromagnetic and thermal dynamics of MWA. These models facilitate the exploration of different ablation scenarios, potentially refining treatment efficacy and safety. They provide fast estimations of electromagnetic wave propagation, energy absorption by tissues, and the subsequent temperature changes, each part of which poses a multi-physics problem that must be handled appropriately for accurate results.

This section explores the progression of modelling approaches and probe design innovations that have emerged, highlighting their significant contributions to the development of more effective, precise, and safe MWA procedures. The intricate modelling process is essential for both device design refinement and understanding ablation dynamics, leveraging the governing principles of electromagnetic wave propagation and energy absorption.

2.3 Evolution of Modelling Techniques

The progression from basic models to more sophisticated simulations highlights an ever-deepening understanding of biological tissue properties and their significant impact on MWA outcomes. With an increasing number of tissue phenomena available for modelling—from porous media and tissue contraction to vaporization—the challenge lies in incorporating all these aspects into a single, manageable simulation. The selection of tissue models to include becomes study-dependent, driven by the specific objectives and constraints of the analysis. Notably, while comprehensive modelling offers a closer approximation of real-world scenarios, practical limitations often necessitate a focus on a subset of phenomena. This approach aligns with the inherent trade-offs between model complexity, computational feasibility, and the specific insights sought through the simulation.

The standard approach to solving the multiphysics problems inherent in MWA simulations is through Finite Element Method (FEM) modelling, a technique that allows for the detailed representation and analysis of complex interactions within the tissues

being modelled. Commercial software packages like COMSOL Multiphysics [98], CST Studio Suite [99], and ANSYS are frequently employed due to their comprehensive toolsets for addressing the diverse challenges of MWA modelling.

With this in mind, let's examine the building blocks that make up the computational modelling of MWA.

2.3.1 Electromagnetic Field Modelling

Electromagnetic modelling relies on the governing Maxwell equations, a set of laws that can be used to predict how electric and magnetic fields interact with their surroundings. Of particular importance in MWA modelling are the dielectric properties, as we have clarified in the previous chapter[100][74]. Accordingly, the dielectric properties of the tissue will determine the shape of the electric and magnetic fields yielded from a given probe, and therefore the resulting temperature profile.

Transfer of energy from the electromagnetic field to tissue can be described by a quantity called the Specific Absorption Rate (SAR) - the power absorbed per unit mass of tissue [101]. This is quantified as a function of Electric field strength $\mathbf{E}$, effective conductivity σ, and tissue density ρ [102]:

$$SAR = \frac{\sigma|\mathbf{E}|^2}{2\rho} \tag{2.1}$$

Directly related to the electric field, this is a useful metric to draw from a given probe design to predict how it may perform in a clinical setting, as the SAR pattern created will influence the temperature distribution. Since most tumour shapes are typically spherical, SAR patterns are often the focus of attention in the design phase in order to produce matching temperature fields to destroy the tumour with minimal damage to surrounding healthy tissue.

2.3.2 Pennes Bioheat Model

Early heat transfer models in biological tissues, notably the Pennes bioheat equation, laid a foundational framework by simplifying the complex heat transfer processes in living organisms [103]. The Pennes model accounts for conductive and convective

heat transfers, along with metabolic heat generation, providing a basic but effective approximation for the transient temperature distribution within targeted tissue volumes, crucial for analyzing the progression of thermal therapies like ablation.

However, as tissue heats, the situation becomes increasingly complex. Changes occur at molecular, cellular, and structural levels, leading to alterations in thermal, mechanical, and dielectric properties of tissues [95]. These changes challenge the basic assumptions of the Pennes model, necessitating more sophisticated models or adaptations that can account for the dynamic nature of tissue properties undergoing heating.

2.4 Probe Design Innovations

With the foundational understanding of electromagnetic field modelling and the complexities of bioheat transfer in tissues, we transition to exploring the practical applications of these theories in the design and optimization of MWA probes. The advancements in modelling techniques have directly influenced the development of probe designs, aimed at overcoming specific limitations identified in MWA treatments. By applying theoretical insights into electromagnetic behaviour and thermal dynamics, engineers and researchers have developed probes that offer improved ablation characteristics.

The field of MWA has seen significant advancements through the exploration of varied probe designs. These include the monopole (M) probe structure [104], which maintains the main coaxial body but with a section of the outer conductor removed towards the end. The single slotted (SS) probe described earlier in this subsection [93, 79, 105], a dual slotted (DS) probe with two gaps in the outer conductor separated by a fixed length [90], and a sleeve single slotted (SSS) probe, containing the same coaxial geometry of the single slot but with an additional layer of conducting material within the catheter [106, 107, 89].These designs will be discussed in more depth in later chapters, but a brief overview of the main features of each of the designs is given here. A basic illustration of these probe concepts is shown in Figure 2.4

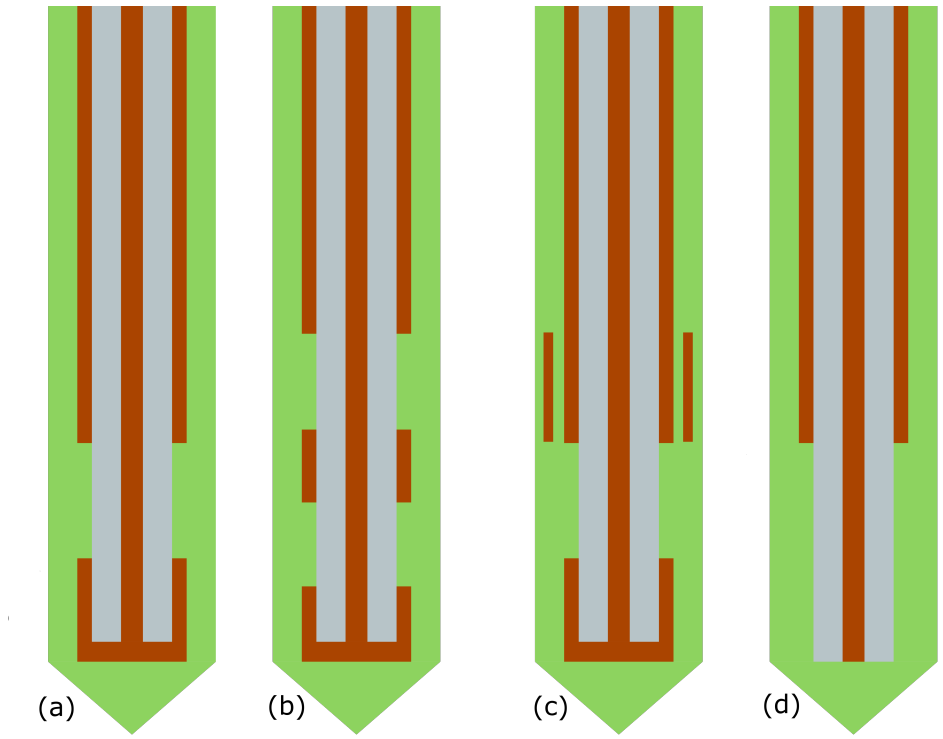

Figure 2.4: The four prominent probe designs, the single slotted probe (a), dual slotted probe (b), sleeve single slotted probe (c), and the monopole probe (d).

In MWA, the design of the probe is critically influenced by the effective wavelength in biological tissue, particularly how it governs the electric field strength at the probe tip. The active part of the probe, typically the section of the inner conductor exposed at the end, is optimized to be a quarter of the effective wavelength. This specific length is crucial because it strategically positions the maximum strength of the electric field at the probe tip, where ablation is intended. The effective wavelength can be calculated through:

$$\lambda_{eff} = \frac{c}{f\sqrt{\varepsilon_r}} \tag{2.2}$$

Where λ_{eff} is the effective wavelength of a signal with frequency f in a tissue with relative permittivity ε_r, and c is the speed of light [108, 1].

The quarter-wavelength is significant because it corresponds to the point where the standing wave pattern within the probe naturally concentrates the electric field strength. At this location, the electric field exhibits its highest intensity, directly at the interface between the probe and the tissue. This intense electric field is essential for effectively inducing dielectric heating in the tissue, which is the mechanism by which ablation occurs. By ensuring that the peak electric field strength occurs right at the tip, the

probe delivers focused energy to the target area, enhancing the precision and efficacy of the ablation process[1]. It is therefore seen that M type probes can be optimised so that the length of the inner conductor is adjusted to be a quarter of the effective wavelength, calculated to be near 14 mm for antennas in liver tissue at an operational frequency of 2.45 GHz [109, 108], and for slotted probes, the position is optimised by placement at a quarter of the effective wavelength from the shorted tip [93, 110]

The DS probe effectively has two sources that radiate out from the antenna, one from each slot. These two waves interact destructively around the upper region of the upper slot to reduce the elongation of the electric field pattern along the outside of the outer conductor. Reducing this elongation aims to create more concentrated absorption patterns that are closer to the spherical ideal [80]. Although DS designs have been shown to create larger and more spherical ablations compared to M designs, their performance is sensitive to slot design since the concept relies on the interaction of waves from the two slots [90]. Nevertheless, it is still seen that the probe designs proposed by M, S, and DS concepts are affected to an extent by backward heating along the track of the probe, resulting in elliptical or teardrop shaped heating patterns where healthy tissue is damaged unnecessarily [1, 111].

An SSS probe aims to achieve the same outcome by introducing a sheath of conducting material within the catheter that surrounds the coaxial structure, but maintaining separation from the outer coaxial layer itself [112][113]. These designs have been shown to confine the absorption pattern towards the probe tip. this typically comes with the concession that a wider probe diameter is needed to facilitate the housing of the sleeve, however, some designs endeavour to include sleeves within miniaturised probe designs [114][115]. These pattern characteristics can vary depending on the exact dimension of the probe design, as will be highlighted later in this thesis.

The introduction of internally-cooled probes represented a significant advancement in managing the temperature in and around the probe itself, through the use of either gas [116, 117], or water as coolant [118]. By allowing for higher energy delivery without the

risk of overheating, these probes enabled the creation of larger ablation zones without increasing the risk of damage to adjacent tissues, and observing reduced tissue charring in the area around the probe, as has been seen in experimental studies [91, 119, 94]. In prospective clinical studies, shaft-cooled probes have been shown to effectively treat tumours [117], and achieve large ablated regions [119]. Moreover, in the application of MWA for the treatment of thyroid nodules, the cooled probes elicited a lower patient pain intensity in comparison to the same procedure involving an uncooled MWA device [120].

Modelling of fluid-cooled probes has been conducted, with the cooling influence typically implemented using boundary conditions that assign fixed temperature values to parts of the probe internals [121], or by using convective boundary conditions on these same parts of the probe [122, 123, 124, 125], with some studies taking a more fluid dynamics approach [94].

2.5 Advancements in Modelling

Ongoing efforts in the field of MWA modelling have focused on incorporating more detailed physiological and pathological tissue characteristics to improve the accuracy and clinical relevance of the simulations. In addition to those already discussed, key advancements include:

2.5.1 Water Vaporization and Tissue Contraction

The decrease in the dielectric properties of the tissue with increasing temperature due to evaporation has been incorporated into the models by accounting for the latent heat of vaporization. The effect of internal water evaporation in the bioheat equation was included by replacing specific heat with an effective specific heat value, representing a step forward in physiological modelling [126, 127]. Additionally, the shrinkage of the tissue volume through a combination of protein denaturing, dehydration, and collagen contracts through heating [128, 129], which can be caused by both RFA and MWA modalities, has been observed and studied in laboratory experiments [74]. As such, predictive models of tissue contraction have emerged to account for the dimension

changes that are not accounted for in a fixed geometry [130, 131].

2.5.2 Porous Media Models

More complex heat transfer models based on the porosity concept have been used to analyze MWA, leading to two bioheat equations for tissue and blood temperatures [132, 133]. As explored by Keangin and Rattanadecho, the consideration of tissue porosity and its effect on SAR and temperature gradients provides a more nuanced view of energy absorption and dissipation mechanisms within the liver [134]. This detailed modelling approach allows for the simulation of blood flow's cooling effects and the resulting heat sink impact, crucial for the design of tailored ablation strategies that account for individual tumour characteristics and surrounding tissue properties. While porous media models are considered to be more realistic, they introduce a new set of parameters whose values are difficult to determine precisely.

2.5.3 Dimensionality of modelling

The use of simplified geometries through 2D modelling and assumptions of axial symmetry has been widely used in MWA studies. Early studies demonstrated the utility of these methods in capturing the essential physics of the problem, focusing on the theoretical underpinnings of thermal and electromagnetic interactions [104, 106, 135, 122, 118, 136]. Building on this work, further refinements and enhancements were introduced to address specific aspects of probe design and thermal behavior, improving the predictive accuracy of simulations [123, 121, 93, 124, 89, 47].

In recent years, advancements in 2D modelling have targeted specific applications, incorporating new features to account for tissue variability and more realistic boundary conditions [111, 88, 97, 134, 139, 43]. However, despite these improvements, the inherent limitations of 2D modelling—particularly its assumption of homogeneity in the surrounding tissue—have been increasingly highlighted in the literature. These limitations have driven the development of more advanced approaches, including 3D simulations and patient-specific modelling, to address the heterogeneity and complexity of biological systems [137, 112, 113, 138, 140, 133].

The importance of performing full 3D simulations for each tumour individually, or due to the geometric complexity of the problem in question, has been emphasized in recent studies [141, 137, 115, 105, 42, 48, 94, 127]. To give some instances where a 2D approach would not suffice: simulations have been performed using realistic 3D models of tumours obtained from CT scan databases, such as the 3D-IRCADb-01 database [127], rather than assuming simplified tumour shapes. In another instance, non-symmetrical probe design aimed at directional control of ablation field [141], or other asymmetric probe geometries [137, 115].

2.6 Study design

2.7 Aims and objectives

Now that we have laid out the background on ablation therapy, the challenges MWA faces, and the progressive efforts to enhance standards, it becomes necessary to narrow our focus to the specific problems this research aims to tackle. The forthcoming chapters will delve into sophisticated simulations and analyses, which are crucial to advancing our understanding and capabilities within MWA.

2.7.1 Transient Shape Changes with Temperature-Dependent Dielectric Properties

Recognizing the importance of the temperature profile's shape in the effectiveness of ablation, and acknowledging the highly variable behavior of tissue dielectric properties throughout the procedure, our first objective investigates these dynamics in detail. The ideal outcome of ablation therapy aims to closely match the ablation zone with the tumour shape, typically spherical, to minimize damage to surrounding healthy tissues and ensure complete eradication of the tumour. This precision is critical and heavily influenced by the transient properties of the tissue undergoing ablation.

Previous studies have modelled temperature-dependent dielectric properties, highlighting their impact on ablation outcomes [46]. Although these temperature-dependent models have been included in ablation studies, these models often focus on the end-state shapes and sizes of temperature profiles and do not dynamically account for changes during the ablation process [48]. Furthermore, while many simulation studies exist they rarely engage in broad comparative analyses and typically examine only one or two probe designs under varying conditions [134, 115, 138, 139, 111]. In contrast, a comparative analysis for four different probe types and their resulting temperature distributions was provided, but without accounting for changes in tissue dielectric properties throughout the procedure, a crucial aspect for predicting more realistic outcomes [109].

Our research advances this field by incorporating a dynamic model of temperature-dependent dielectric properties into our MWA simulations, focusing on analyzing how these properties transiently influence the shape and size of SAR and temperature distributions. We conduct a comparative analysis across four different probe designs under consistent conditions of power, ablation time, and simulated tissue conditions, providing a robust framework for evaluating probe performance and interactions with dynamic tissue changes. This approach offers a comprehensive view of how different probe configurations can lead to varied ablation shapes and sizes, thus affecting the clinical outcomes of the procedures.

This work not only accounts for the initial and final states but also captures the transient behaviour of the field shapes, providing a more comprehensive understanding of the ablation process, as demonstrated in [142].

2.7.2 Parametric study of water cooled probes

While advancements in MWA technology have led to probe designs with more attractive characteristics, existing models often do not fully capture the complex fluid dynamics within probe cooling systems. Simplified boundary conditions, such as those employed

in [121, 125], approximate the effects of coolant systems but may overlook crucial dynamic interactions. More recently, computational fluid dynamics has been used to assess the impacts of coolant flow rate on thermal profiles with an individual probe design, indicating the benefits of more advanced modelling [94].

Building on these insights, our study proposes to advance the simulation complexity by incorporating comprehensive fluid flow computation into the design of cooling mechanisms within MWA probes. This approach will allow us to conduct a detailed multi-variant analysis, investigating how coolant flow rate, temperature, and coolant positioning influence the resultant ablation fields. By focusing on these less frequently modelled aspects of probe design, particularly the internal cooling through the circulation of a coolant fluid, our research aims to address issues such as non-uniform heating patterns and probe overheating. This novel approach offers advancements over the current literature by delivering a more nuanced understanding of how different probe configurations can lead to varied ablation shapes and efficiencies, thus affecting the clinical outcomes of the procedures.

2.7.3 Development of an Open-Source Simulation Package

A primary objective of our research is to develop a bespoke simulation package using publicly available sources, designed to simulate MWA probe designs at a quality comparable to commercial multi-physics modelling packages. This initiative aligns with the overarching goals of equality, inclusivity, and diversity in scientific research by leveraging open-source software.

The rationale for employing open-source software stems from its potential to democratize access to sophisticated simulation tools. This approach allows for broader participation in cutting-edge research, particularly enabling institutions with limited resources to engage in high-level scientific studies. Additionally, using open-source software would enhance the transparency and collaborative potential of our research, fostering a more inclusive research community. By developing this tool, we aim to

provide an accessible platform that can be further developed by researchers to advance the field of MWA. In addition, this thesis aims to give an extensive description and derivation of the mathematical and computational background to MWA modelling, which would be particularly useful for engineers without a strong electromagnetic or MWA background.

2.7.4 Thesis overview

In Chapter 3 we break down, in detail, the components required to create the two-dimensional framework upon which the research elements of this work are based. These are the fundamental equations that describe the electromagnetic problem and then the associated bioheat equation for calculating a temperature distribution throughout our domain. We then aim to validate our model at various levels, with benchmark tests of the finite element models used, then comparison with other simulated datasets and appropriate experimental data suitable for comparison.

In Chapter 4, we outline the finite element method (FEM), a key computational technique used throughout this thesis. The chapter focuses on critical aspects of FEM, including domain discretization, weak formulation, and boundary condition implementation. Special emphasis is placed on using H(Curl) elements for electromagnetic simulations and Lagrange elements for thermal modeling. The chapter also validates the FEM framework with benchmark cases, ensuring accuracy and reliability for subsequent simulations.

In Chapter 5 we introduce several prominent probe concepts that exist in the literature and begin an investigation into the different shapes of both SAR and temperature patterns yielded from this selection. In particular, we compute shape metrics on the ablation variables in a transient fashion, highlighting the influence that temperature-dependent tissue properties have on these shapes.

In Chapter 6 an advancement in the 2D framework is made, and we consider more

complex designs in the form of the internally fluid-cooled probe concept. Advancing on the current modelling standard for this type of probe, a full fluid flow computation is made by embedding the relevant partial differential equations into the existing FEM framework. Using this improved model to investigate the effect of coolant location, coolant input temperature, and flow rate on the resulting temperature fields.

3 Two Dimensional Modelling in Microwave Ablation

3.1 Overview

Modelling of MWA involves simulating the coupling between electromagnetic energy propagation and the resulting heat transfer, in this chapter, the complete set of relevant governing equations is presented, and a breakdown of how these are discretized into a form that allows solutions to be computed in the finite element scheme we have selected.

Firstly though, an understanding of the geometry and assumptions made that define the problem. An overview of the basic structure of microwave ablation probes has already been discussed, as well as the supporting hardware that enables microwave ablation procedures to be carried out, but when considering constructing a model for such a treatment it is desirable to reduce the computational domain to focus on a region of particular interest. In this case, only the MWA probe itself and the surrounding tissues are of importance to gaining an understanding of how ablation develops throughout treatment, all components outside of this region can be excluded from analysis. We will therefore not consider the generator or connecting coaxial transmission lines within our modelling, instead, we employ appropriate boundary conditions up the truncated domain that aim to give the equivalent response that the structures themselves would ordinarily display.

So far, the domain remains three-dimensional (3D). However, for the analysis carried out in this thesis it is appropriate to simplify the domain. Therefore, leveraging the probe's symmetrical design around its axis allows for a reduction in dimensionality from 3D to 2D geometry, as illustrated in Fig 3.1.a. Furthermore, assuming such an axial symmetry enables further reduction of the computational domain, as depicted in Fig 3.1.b. These reductions in the computational domain impose limitations on the tissue characteristics that can be modelled; for example, a 2D domain does not support the modelling of axisymmetric biological features within the tissue such as larger vascular structures. Consequently, the tissue must be treated as isotropic and

homogeneous. Additionally, the probe designs modelled with this 2D approach must inherently possess axial symmetry; directional probes [141] and some internally cooled designs are not suitable for simulation without expanding the model's dimensionality and considering asymmetrical aspects.

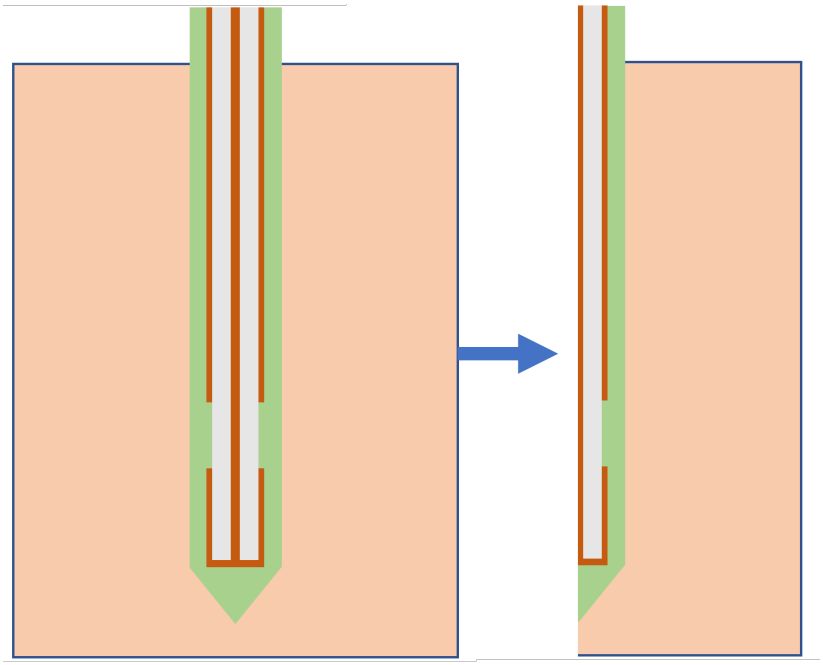

Figure 3.1: A 3D geometry can be reduced to a 2D geometry by assuming homogeneity of the tissue (Fig. a). Further reduction is achieved by assuming axial symmetry of the probe, allowing the domain to be halved as shown in Fig. b.

Using this reduced geometry, the domain can now be split up into its constitutive components and their related boundaries, an essential step for implementing physical models discussed later. Figure 3.2 shows a fully annotated single-slotted probe with domain Ω which encompasses all the materials within the figure, those are the inner and outer conductors, dielectric, air gap, catheter, and tissue. This domain is enclosed by $\partial\Omega$, a boundary with components $\partial\Omega_1$ at the top of the dielectric - the input to the probe, $\partial\Omega_2$ around the tissue boundaries, and $\partial\Omega_3$ that lies on the surfaces of the

inner and outer conductors. This breakdown of the domain will be sufficient for the modelling of non-cooled MWA probe designs. The catheter encapsulates the active microwave antenna and must serve a dual purpose to both ensure hygienic requirements during the procedure through its inertness and biocompatibility, whilst also allowing coupling of electromagnetic fields generated from the antenna to pass into the tissue.

Now the computational domain and boundaries are fully defined, building a computational framework can begin, initially by establishing a full definition of the electromagnetic problem from the fundamental principles of electromagnetism. This is covered in section 3.2.

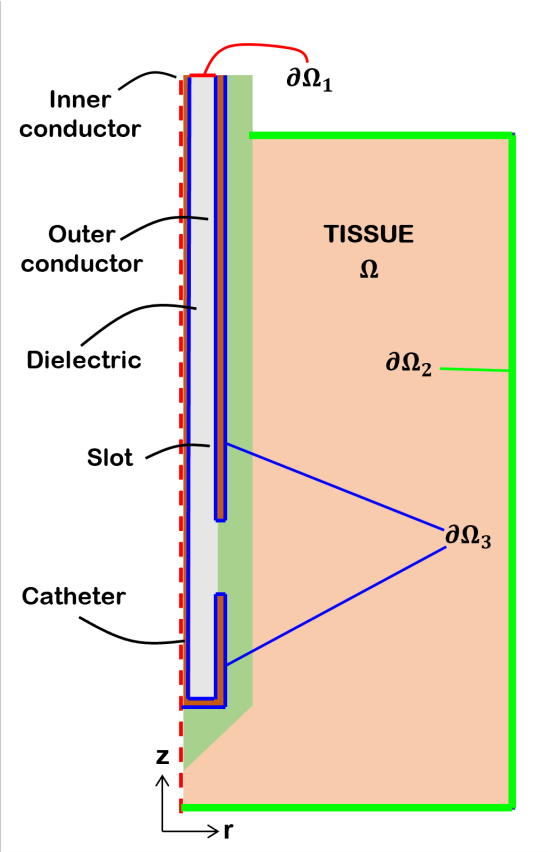

Figure 3.2: From the reduced geometry, domain Ω is defined with boundary a $\partial\Omega$ made from parts $\partial\Omega_1$, $\partial\Omega_2$, and $\partial\Omega_3$

Variable Summary		
Symbol	Name	Unit
$\mathbf{D}$	Electric flux density	$C.m^{-2}$
$\mathbf{B}$	Magnetic flux density	$Wb.m^{-2}$
$\mathbf{E}$	Electric field	$V.m^{-1}$
$\mathbf{H}$	Magnetic field	$A.m^{-1}$
$\mathbf{J}$	Current density	$A.m^{-2}$
ρ	Charge density	$C.m^{-3}$
ε	Electrical permittivity	$F.m^{-1}$
μ	Electrical permeability	$H.m^{-1}$
ω	Angular frequency	Hz
σ	Electrical conductivity	$S.m^{-1}$
j	imaginary unit	-
k_0	free space wavenumber	m^{-1}
$\mathbf{n}$	Surface normal vector	-
ρ_l	Mass Density	$kg.m^{-3}$
C_l	Specific heat capacity	$J.kg^{-1}.K^{-1}$
k_l	Thermal conductivity	$W.m^{-1}.K^{-1}$

Table 3.1: A summary of the relevant variables used in the electromagnetic and thermal governing equations.

3.2 Electromagnetic theory

Before going into the governing equations for this multiphysics model, an overall summary of the main variables that are involved is given in Table 3.1. An approach to calculating the electromagnetic field within the MWA problem can be split into three main parts. The first is to take some known input power and translate this into an electric and magnetic field strength at the feed point of the antenna, this relationship is described by Poynting's theorem. Next in line is to understand and compute how these microwaves propagate along the antenna towards the slot, then finally predict the dispersion of the waves through the tissue domain and calculate the resulting fields. To tackle any of these parts, the fundamental equations governing electromagnetic

behaviour must be utilized, it is therefore a good place to begin by introducing these governing rules - the Maxwell equations.

3.2.1 Maxwell equations

Named after the scientist James Clerk Maxwell, these four coupled partial differential equations together describe how electric and magnetic fields interact with each other, and provide a mathematical model for electromagnetic wave propagation. From here onwards, for ease of understanding, any variables in bold typeface are vector quantities. The four primary vector variables referred to within this section are the electric field $\mathbf{E}$, the electric flux $\mathbf{D}$, the magnetic field $\mathbf{H}$ and magnetic flux density $\mathbf{B}$. Here is a brief overview of each of the Maxwell equations and their physical interpretation, below they are explained and expressed in their integral forms using closed line and closed surface integrals, denoted as $\oint$ and $\oiint$ respectively, and then their more general differential forms.

Gauss' law

The first of Maxwell's equations is Gauss' law and describes how an electric field behaves around electric charges. In words it can be expressed as; the net electric flux Φ_E through any hypothetical closed surface is equal to $\frac{1}{\varepsilon_0}$, where ε_0 is the free space permittivity, multiplied by the net electric charge Q within that closed surface:

$$\Phi_E = \frac{Q}{\varepsilon_0} \tag{3.1}$$

If we call this closed surface S, which encloses a volume V, the electric flux can be written in terms of a surface integral of the electric field $\mathbf{E}$:

$$\Phi_E = \oiint_S \mathbf{E}\ d\mathbf{A} = \frac{Q}{\varepsilon_0} \tag{3.2}$$

where $d\mathbf{A}$ is a vector representing an infinitesimally small element of area on the surface. This is the integral form of Gauss' law, to find the differential form divergence theorem is applied to the surface integral and the change is expressed as a volume integral of the charge density ρ within the bounded volume.

$$\iiint_V \nabla \cdot \mathbf{E}\ dV = \iiint_V \frac{\rho}{\varepsilon_0}\ dV \tag{3.3}$$

which will hold for any volume V, and therefore

$$\nabla \cdot \mathbf{E} = \frac{\rho}{\varepsilon_0}. \tag{3.4}$$

Gauss's law for magnetism

Second is Gauss' law of magnetism, which states magnetic monopoles do not exist but instead must be attributed to a dipole, and that the total magnetic flux through a closed surface must be zero. Similarly to Gauss's law, if the magnetic flux Φ_B through a bound surface can be expressed by a surface integral of the magnetic flux density $\mathbf{B}$ in this case.

$$\Phi_B = \oiint_S \mathbf{B}\ d\mathbf{A} = 0 \tag{3.5}$$

This is the integral form, application of the divergence theorem yields the differential form,

$$\iiint_V \nabla \cdot \mathbf{B}\ dV = 0. \tag{3.6}$$

Which, again, will hold for any volume and so therefore

$$\nabla \cdot \mathbf{B} = 0. \tag{3.7}$$

Since the relation between magnetic flux density and magnetic field exists through the permeability, μ of said material as

$$\mathbf{B} = \mu\mathbf{H}, \tag{3.8}$$

which will be discussed in further detail later, Gauss's law of magnetism could also be written in terms of the magnetic field

$$\nabla \cdot \mathbf{H} = 0. \tag{3.9}$$

However, in magnetic materials where magnetization $\mathbf{M}$ is non-negligible, the relationship between $\mathbf{B}$ and $\mathbf{H}$ must consider the magnetization vector:

$$\mathbf{B} = \mu\mathbf{H} + \mu_0\mathbf{M} \tag{3.10}$$

This modifies the divergence condition for $\mathbf{H}$, leading to:

$$\nabla \cdot \mathbf{B} = \mu_0 \nabla \cdot \mathbf{M} \tag{3.11}$$

As $\nabla \cdot \mathbf{B} = 0$ always holds, if $\nabla \cdot \mathbf{M} \neq 0$, then $\nabla \cdot \mathbf{H}$ is not zero, reflecting the contribution of magnetization within the material.

Faraday's law

The third Maxwell equation is Faraday's law, showing how a magnetic field that is changing in time t, will give rise to a rotating electric field, $\mathbf{E}$, which is also time dependent. Mathematically this takes the form

$$\nabla \times \mathbf{E} = -\frac{\partial \mathbf{B}}{\partial t}. \tag{3.12}$$

Ampere's law

The fourth is Ampère's law, which states a magnetic field $\mathbf{H}$ can be generated by both electric current $\mathbf{J}$, and by a changing electric field $\frac{\partial \mathbf{D}}{\partial t}$. To find its integral form consider the definition as The magnetic field around any closed loop C that bounds a surface S, is proportional to the electric current $\mathbf{J}$ plus the displacement current (equal to $\frac{\partial \mathbf{D}}{\partial t}$) through the enclosed surface.

$$\oint_C \mathbf{H}\, dC = \iint_S \mathbf{J}\, dS + \iint_S \frac{\partial \mathbf{D}}{\partial t}\, dS \tag{3.13}$$

Kelvin-Stokes theorem allows the line integral of a field to be rewritten as a surface integral of the curl of the field,

$$\iint_S (\nabla \times \mathbf{H})\ d\mathbf{S} = \iint_S \left(\mathbf{J} + \frac{\partial \mathbf{D}}{\partial t}\right)\ d\mathbf{S}. \tag{3.14}$$

Therefore, the differential form can be expressed as

$$\nabla \times \mathbf{H} = \mathbf{J} + \frac{\partial \mathbf{D}}{\partial t}. \tag{3.15}$$

3.2.2 Time-Harmonic forms

These fields discussed exhibit sinusoidal time variation, in other words, they are time-harmonic. In order to simplify the mathematics going forward we can make use of this characteristic to eliminate time-dependent terms within the differential form of the Maxwell equations.

To make this change, first, take the assumption that electric and magnetic fields are variable with both space and time and so can be expressed as the product of some space-dependant function $X(x, y, z)$ and some time-dependent function $T(t)$. Time harmonic waves display oscillations over time, this sinusoidal time dependence can be described through complex notation as follows $e^{j\omega t}$, and so the appropriate substitutions can be made:

$$\mathbf{E}(x, y, z, t) = X(x, y, z) \cdot T(t) = X(x, y, z) \cdot e^{j\omega t} \tag{3.16}$$

$$\mathbf{H}(x, y, z, t) = X(x, y, z) \cdot T(t) = X(x, y, z) \cdot e^{j\omega t} \tag{3.17}$$

Using j as the imaginary unit and ω for the angular frequency. The time derivative of each of these functions is equal to the original function multiplied by $j\omega$. Substituting this into equations(3.4,3.9,3.12,3.15) converts the derivative forms to the time-harmonic Maxwell equations:

$$\nabla \cdot \mathbf{E} = \frac{\rho}{\varepsilon_0} \tag{3.18}$$

$$\nabla \cdot \mathbf{H} = 0 \tag{3.19}$$

$$\nabla \times \mathbf{E} = -j\omega\mathbf{B} \tag{3.20}$$

$$\nabla \times \mathbf{H} = \mathbf{J} + j\omega\mathbf{D} \tag{3.21}$$

3.2.3 Constitutive relations

Maxwell's equations define the fields that are generated by currents and charges but do not describe how these currents and charges are generated. Therefore these equations must be supplemented by relations that describe the behaviour of material under the influence of fields, these are covered by the constitutive equations. For general use, these are:

$$\mathbf{D} = \varepsilon\mathbf{E} \tag{3.22}$$

$$\mathbf{B} = \mu\mathbf{H} \tag{3.23}$$

Where μ is the permeability and ε represents the absolute permittivity of the material, these properties dictate how a material responds to electromagnetic fields and can be complex, frequency-dependent, and non-linear. To illustrate this, the complex forms

are given by:

$$\varepsilon = \varepsilon' - j\varepsilon'' \tag{3.24}$$

$$\mu = \mu' - j\mu'' \tag{3.25}$$

Here ε' and μ'' denote the real parts, reflecting the capacity to store electric and magnetic energy, respectively. ε'' and μ'' are the imaginary parts that correspond to energy dissipation within the material, primarily as heat. The negative sign in front of the imaginary parts follows the convention used in the engineering and physics literature to denote loss through the positive imaginary component in the exponential of the wave equation, which shows attenuation as the wave propagates through the material.

As previously mentioned, magnetic permeability in biological tissues can be approximated to that of free space, yet it can exhibit complex characteristics in other materials, indicating energy losses similar to those described for permittivity.

Considering the context of a lossy capacitor, complex permittivity provides a useful analogy for understanding how materials respond to alternating electric fields. In an ideal scenario, a capacitor would store and release electrical energy without losses. However, real capacitors often exhibit 'lossy' behaviour due to the imaginary part of the permittivity (ε''). This component causes energy dissipation as heat during each cycle of the applied AC field, reducing the efficiency of energy storage.

When an AC voltage is applied, the imaginary part of the permittivity leads to a phase shift between the voltage and current, indicating that not all the energy stored in the electric field is fully recoverable. Instead, a portion of it is converted into heat, which is critical in applications like microwave ablation where controlled heating is required.

The real part of complex permittivity (ε'), or ε_r as it is more commonly referred to, represents the material's capacity to store electrical energy. It indicates how much energy the electric field can hold relative to a vacuum, which is crucial for understanding

the energy storage capabilities of the material without implying any direct contribution to energy loss.

The imaginary part of permittivity is closely related to the effective conductivity (σ), which quantifies the conversion of electromagnetic wave energy into heat within the material. For lossless materials, the conductivity is zero, meaning there is no absorption of energy. However, in lossy materials like biological tissue, a non-zero conductivity implies significant energy absorption, essential for the heating observed in microwave ablation processes.

To express a lossy material such as tissue we include a vector form of Ohm's law, with the condition that electrical conductivity is non-zero.

$$\mathbf{J} = \sigma \mathbf{E} \quad , \quad \sigma \neq 0 \tag{3.26}$$

In addition, the assumption that this material is source-free means a value of 0 can be assigned to the charge density,

$$\rho = 0. \tag{3.27}$$

This completes the set of equations necessary for modelling the behaviour of electromagnetic waves in MWA. It must first be assembled into a vector wave equation.

3.2.4 Vector wave equation

Solving the Maxwell equations for either **E** or **H** can be achieved by combining them to form a wave equation with a singular unknown vector. What follows is the derivation of an equation in **E** from the time-harmonic forms and taking constitutive relations from equations (3.22,3.23,3.26) for such a material with both dielectric and conductive properties. These constitutive relations may change depending on the material within the computational domain, but the substitution of the corresponding variable values into the wave equation ensures it remains true.

Derivation

Beginning with Faraday's law, Eq. (3.20), and substituting out the magnetic flux

density through the use of the constitutive relation to **H** in (3.23),

$$\nabla \times \mathbf{E} = -j\omega\mu\mathbf{H}. \tag{3.28}$$

Similarly, Ampère's law (3.21) can be expressed solely in terms of **E** and **H** by use of Ohm's (3.26) to replace **J**, and constitutive relation between electric flux density and field from (3.22). Making these substitutions and simplifying gives

$$\nabla \times \mathbf{H} = j\omega\left(\varepsilon - j\frac{\sigma}{\omega}\right)\mathbf{E}. \tag{3.29}$$

Taking the curl of (3.28) allows substitution of (3.29) on the right-hand side, leaving a partial differential equation where **E** is the only unknown vector,

$$\nabla \times \nabla \times \mathbf{E} = -j\omega\mu\nabla \times \mathbf{H} = -j\omega\mu\left(j\omega\left(\varepsilon - j\frac{\sigma}{\omega}\right)\mathbf{E}\right). \tag{3.30}$$

This can be simplified to

$$\nabla \times \nabla \times \mathbf{E} = \omega^2\mu\left(\varepsilon - j\frac{\sigma}{\omega}\right)\mathbf{E}. \tag{3.31}$$

The electrical permeability and permittivity can also be expressed as the product of relative permeability μ_r and free space permeability μ_0, and relative permittivity ε_r and free space permittivity ε_0.

$$\mu = \mu_r\mu_0 \tag{3.32}$$

$$\varepsilon = \varepsilon_r\varepsilon_0 \tag{3.33}$$

Expanding these terms in Eq (3.31) gives

$$\nabla \times \nabla \times \mathbf{E} = \omega^2\mu_r\mu_0\left(\varepsilon_r\varepsilon_0 - j\frac{\sigma}{\omega}\right)\mathbf{E}, \tag{3.34}$$

Which can be rearranged to

$$\nabla \times \mu_r^{-1}\left(\nabla \times \mathbf{E}\right) = \omega^2\mu_0\varepsilon_0\left(\varepsilon_r - j\frac{\sigma}{\omega\varepsilon_0}\right)\mathbf{E}, \tag{3.35}$$

The purpose of such a rearrangement is to group terms that can collectively be described as the free space wave number, k_0, written as

$$k_0 = \omega\sqrt{\mu_0\varepsilon_0}. \tag{3.36}$$

The result of this is the equation taking the form of the classic vector wave equation,

$$\nabla \times \mu_r^{-1} (\nabla \times \mathbf{E}) - k_0^2 \left(\varepsilon_r - j \frac{\sigma}{\omega \varepsilon_0} \right) \mathbf{E} = 0. \tag{3.37}$$

This wave equation can then be solved to compute the electric field within the entire domain.

3.2.5 Waves in biological tissue

Due to the axis-symmetric design of the probes considered in this thesis, EM waves propagate in the transverse magnetic mode - a radiation pattern where no component of the magnetic field exists in the direction of wave propagation. Since the waves are able to propagate in both the z and r directions within the tissue domain, it stands to reason that the magnetic field must act purely in the azimuthal direction.

3.2.6 Modes of Propagation in Coaxial Cable

In a coaxial cable, different modes of electromagnetic waves can propagate. The primary mode is the TEM mode, where both electric and magnetic fields are orthogonal to the direction of wave propagation, and no cutoff frequency is required for its propagation. However, at higher frequencies, transverse electric (TE) and transverse magnetic (TM) modes can also propagate, each with its respective cutoff frequency determined by the cable's geometry:

- **TE Modes**: These modes have electric fields that lie entirely in the transverse plane but have no radial component of the magnetic field.
- **TM Modes**: These modes have magnetic fields that lie entirely in the transverse plane but have no radial component of the electric field.

The existence of these modes beyond the TEM mode is primarily due to the boundary conditions imposed by the coaxial structure and is significantly influenced by the operational frequency. The cutoff frequency (frequency threshold above which modes can propagate) for each mode in a coaxial cable can be calculated from the cable's inner ($a = 0.135\,\text{mm}$) and outer ($b = 0.335\,\text{mm}$) radii. For the first TE mode (TE11) and the first TM mode (TM01), the cutoff frequencies are given by:

$$f_c^{TE11} = \frac{1}{2\pi\sqrt{\mu\epsilon}} \frac{X'_{11}}{b-a}, \tag{3.38}$$

$$f_c^{TM01} = \frac{1}{2\pi\sqrt{\mu\epsilon}} \frac{X_{01}}{b-a}, \tag{3.39}$$

where X'_{11} and X_{01} are the first roots of the derivative of the Bessel function of the first kind and the Bessel function of the zeroth kind, respectively.

Given a typical coaxial interior used in microwave ablation antennas, with inner and outer conductor radii of 0.135mm and 0.335mm respectively, and a low-loss dielectric with a permittivity of 2.1 and permeability comparable to that of free space, the calculated cutoff frequencies for TE11 and TM01 are 303 GHz and 395 GHz, respectively. These frequencies are far higher than the 900 MHz and 2.45 GHz used in MWA, ensuring that only TEM modes exist.

3.2.7 Free Space TEM Waves

In free space, electromagnetic waves can be described by Maxwell's equations in the absence of any charges and currents. The solution to these equations for a plane wave travelling in the z-direction can be expressed as:

$$\mathbf{E} = E_0 \mathbf{e}_x e^{j(kz-\omega t)}, \tag{3.40}$$

$$\mathbf{H} = \frac{E_0}{\eta_0} \mathbf{e}_y e^{j(kz-\omega t)}, \tag{3.41}$$

where E_0 is the amplitude of the electric field, ω is the angular frequency, k is the wave number, and η_0 is the intrinsic impedance of free space, approximately $377\,\Omega$. This impedance represents the ratio of the electric field to the magnetic field in electromagnetic waves travelling through free space. TEM waves exhibit electric and magnetic fields that are perpendicular to each other and the direction of wave propagation.

For computing the propagation of microwave along the probe, consider a purely dielectric material like that within the coaxial structure as having electrically insulative characteristics, in other words, σ is zero in this medium. Therefore,

$$\mathbf{J} = 0. \tag{3.42}$$

Considering also that the charge density within these materials is zero, the wave equation within this material becomes slightly reduced to reflect this lack of absorption,

$$\nabla \times \nabla \times \mathbf{E} = \omega^2 \mu \varepsilon \mathbf{E} \tag{3.43}$$

To eliminate the double curl term, a vector identity can be applied along with Eq. (3.4), simplifying the spatial derivative to

$$\nabla \times \nabla \times \mathbf{E} = \nabla (\nabla \cdot \mathbf{E}) - \nabla^2 \mathbf{E} = \nabla (0) - \nabla^2 \mathbf{E}. \tag{3.44}$$

Similarly to the wave equation derived previously in Eq (3.37), grouped terms can collectively be described as the wave number k,

$$k = \omega \sqrt{\mu \varepsilon}. \tag{3.45}$$

Consequently, the wave equation for $\mathbf{E}$ looks like

$$\nabla^2 \mathbf{E} + k^2 \mathbf{E} = 0. \tag{3.46}$$

Within a coaxial structure, electromagnetic fields are able to propagate in what is known as the Transverse Electromagnetic (TEM) mode, meaning neither the magnetic nor electric field have components that act in the direction of wave propagation. In practice the direction of wave propagation is along the cable (z-plane), therefore creating electric fields with only radial components (r-plane) and magnetic fields in the azimuthal plane (ϕ-plane).

3.2.8 Laplacian in Cylindrical Coordinates and Its Reduction

In the case of the Transverse Electro-Magnetic (TEM) mode, where the electric field $\mathbf{E}$ has no component in the direction of propagation ($E_z = 0$) and no azimuthal component ($E_\phi = 0$), the Laplacian simplifies significantly. The Laplacian in cylindrical coordinates for a TEM vector field $\mathbf{E}$ is given by:

$$\nabla^2 \mathbf{E} = \left(\frac{\partial^2 E_r}{\partial r^2} + \frac{1}{r} \frac{\partial E_r}{\partial r} + \frac{1}{r^2} \frac{\partial^2 E_r}{\partial \phi^2} + \frac{\partial^2 E_r}{\partial z^2} \right) \hat{r} \tag{3.47}$$

Additionally, for TEM modes in coaxial cables, there is symmetry around the axis, meaning that the fields do not depend on the azimuthal angle ϕ, reducing $\frac{\partial^2}{\partial \phi^2}$ terms to zero. The simplified expression for the Laplacian is thus:

$$\nabla^2 \mathbf{E} = \left(\frac{\partial^2 E_r}{\partial r^2} + \frac{1}{r} \frac{\partial E_r}{\partial r} + \frac{\partial^2 E_r}{\partial z^2} \right) \hat{r} \tag{3.48}$$

However, in strict TEM mode, the radial component E_r should not vary along z, leading to:

$$\nabla^2 \mathbf{E} = \left(\frac{\partial^2 E_r}{\partial r^2} + \frac{1}{r} \frac{\partial E_r}{\partial r} \right) \hat{r} \tag{3.49}$$

Applying the wave equation to the radial component E_r yields the Bessel differential equation:

$$\frac{\partial^2 E_r}{\partial r^2} + \frac{1}{r} \frac{\partial E_r}{\partial r} + k^2 E_r = 0 \tag{3.50}$$

This form is known as a Bessel differential equation. The solutions to such equations in cylindrical coordinates, which are finite at the origin and meet boundary conditions at cylindrical surfaces, are given by Bessel functions of the first kind.

$$E_r(r) = A J_0(kr) \tag{3.51}$$

where A represents the amplitude of the electric field, and J_0 is the zeroth-order Bessel function of the first kind, suitable for describing radial behaviours in cylindrical structures without azimuthal variation.

Given the time-harmonic nature of electromagnetic fields in wave propagation and the need for solutions that reflect variations along the coaxial cable's length (z), we integrate the spatial solution with temporal and longitudinal variations:

$$\mathbf{E}(z,t) = \hat{\mathbf{r}} \frac{A_0}{r} e^{j(\omega t \pm kz)} \tag{3.52}$$

$$\mathbf{H}(z,t) = \hat{\boldsymbol{\phi}} \frac{A_0}{Zr} e^{j(\omega t \pm kz)} \tag{3.53}$$

Here, Z denotes the characteristic impedance of the medium, which relates the electric field and the magnetic field magnitudes and phases. The factor $e^{j(\omega t \pm kz)}$ represents the wave propagating along the cable, where ω is the angular frequency of the wave, and k is the wave number, indicating how the phase of the wave varies with time t and position along the cable z.

3.2.9 Application of Poynting's Theorem in Coaxial Cables

Poynting's theorem is essential for describing the power per unit area carried by electromagnetic waves in the form of the Poynting vector, $\mathbf{S}_{av}$. For sinusoidal steady-state fields, the time-averaged Poynting vector can be expressed as:

$$\mathbf{S}_{av} = \frac{1}{2} \mathrm{Re}(\mathbf{E} \times \mathbf{H}^*) \tag{3.54}$$

where $\mathbf{E}$ and $\mathbf{H}$ are the phasor representations of the sinusoidal electric and magnetic fields, respectively. The Poynting vector $\mathbf{S}_{av}$ for the above fields can be simplified to:

$$\mathbf{S}_{av} = \frac{1}{2}\mathrm{Re}\left(\left(\hat{\mathbf{r}}\frac{A_0}{r}e^{j(\omega t - kz)}\right) \times \left(\hat{\boldsymbol{\phi}}\frac{A_0}{Zr}e^{-j(\omega t - kz)}\right)^*\right) \tag{3.55}$$

$$\mathbf{S}_{av} = \hat{\mathbf{z}}\frac{A_0^2}{2Zr^2} \tag{3.56}$$

The total power transmitted through the cable, integrating $\mathbf{S}_{av}$ over the cross-sectional area of the dielectric, is given by:

$$P_{av} = \int_{r_i}^{r_o} \frac{A_0^2}{2Zr^2} 2\pi r \, dr \tag{3.57}$$

$$P_{av} = \frac{\pi A_0^2}{Z} \ln\left(\frac{r_o}{r_i}\right) \tag{3.58}$$

Given the specified average power P_{av} and the impedance Z, the maximum amplitude A_0 of the waves can be calculated:

$$A_0 = \sqrt{\frac{P_{av} Z}{\pi \ln\left(\frac{r_o}{r_i}\right)}} \tag{3.59}$$

This formulation allows a bridging between the theoretical aspects of electromagnetic wave propagation with practical applications in engineering, particularly for designing coaxial cables based on specific power handling requirements. Later we will employ these equations to excite the electro-magnetic simulation, defining $\mathbf{E}_{inc}$ as the electric field amplitude that is incident upon the probe input boundary, which will propagate through the dielectric and into other parts of the computational domain.

3.3 Bioheat model

The bioheat equation models the distribution of temperature (T) with time (t) within a composite domain such as in microwave ablation systems. It takes the form:

$$\underbrace{\rho C \frac{\partial T}{\partial t}}_{\text{Transient heat storage}} = \underbrace{\nabla \cdot (k \nabla T)}_{\text{Heat diffusion}} + \underbrace{Q_p + Q_{SAR} + Q_m}_{\text{Heat sources/sinks}} \tag{3.60}$$

This equation has three constitutive parts, on the left-hand side we have the transient heat storage, dependant on the variables ρ (kg/m^3), C (J/kg·K), represent the mass density and specific heat capacity respectively. On the right, there is a component

describing the heat diffusion throughout the domain, a function of the thermal conductivity, k (W/m·K). The Q terms are all heat sources or sinks of different kind, Q_p (W/m^3), representing heat due to blood perfusion, Q_{SAR} (W/m^3), denoting heat generated by microwave energy absorption, and Q_m (W/m^3), for metabolic heat generation. Furthermore, the material parameters vary spatially within the domain depending on the material, whether it be tissue, parts of the antenna, or the catheter. This variation is essential for accurate modelling, as it influences how heat is stored and transferred through different materials.

Heat loss due to microvascular blood perfusion is represented by the term Q_p, a function of blood perfusion rate ω_b, blood temperature T_b, blood specific heat capacity and density, C_b and ρ_b,

$$Q_p = \omega_b C_b \rho_b (T_b - T). \tag{3.61}$$

For modelling in vivo situations, this sink term is important, however, in the case of simulating ex vivo ablations there is an absence of blood flow and therefore the term is removed.

Coupling the temperature distribution with the electromagnetic field exists through Q_{SAR}, the thermal source from the microwave ablation probe. The energy absorbed from an electric field by the tissue media is captured by the equation:

$$Q_s = \frac{\sigma |\mathbf{E}|^2}{2} \tag{3.62}$$

Q_m represents heat generated from metabolic action, which is commonly ignored due to its negligible magnitude when compared to the microwave and blood perusing terms, and will therefore also be excluded from our modelling.

4 Finite element method

The Finite Element Method (FEM) is a powerful computational technique used to derive approximate solutions to boundary value problems for partial differential equations. It is extensively used in engineering, physics, and other sciences due to its applicability to complex geometries. Here we will give a brief overview of the FEM to add valuable context to the modelling framework we present, but a good source for further insight into the technique would be the work by Leszek Demkowicz, found in [143].

4.1 Formulation of the Finite Element Method

The process of formulating a problem using the Finite Element Method involves several key steps:

4.1.1 Discretising the domain into finite elements

Before solving a problem using the FEM, the first step is the discretization of the domain. This involves dividing the entire area under study into smaller, manageable pieces called finite elements. In a two-dimensional setting, this meshing process typically involves creating elements that are typically triangular or quadrilateral shaped, due to their ability to conform closely to complex domain geometries and for the ease with which they can be connected to form a mesh. In the case of complex geometries or sensitive areas where higher gradients are anticipated, it is advantageous to employ h-refinement by increasing the density of smaller-sized elements. This refinement ensures more detailed modelling in regions requiring greater accuracy due to rapid changes in the physical properties.

Once the domain has been divided into a mesh of geometric shapes the appropriate finite element formulation must be chosen. A 'finite element' in FEM refers to both the geometric segment of the domain — each individual triangle or quadrilateral in the mesh — and the set of mathematical functions or 'basis functions' used within these segments to approximate the physical properties of the problem. These elements collectively act as the building blocks for constructing the numerical solution to the differential equations under study.

For problems involving scalar fields such as temperature, Lagrange elements are typically used. These elements are suitable because they provide continuous polynomial approximations across element boundaries, which are necessary for accurately modelling the gradual variations in temperature. Using Lagrange elements ensures that the temperature field is smoothly approximated, which is essential for accurately capturing the conductive and convective heat transfer processes.

In electromagnetic simulations, the selection of HCurl elements ensures compliance with the boundary conditions dictated by Maxwell's equations. Specifically, HCurl elements enforce that the tangential components of the electric field $\mathbf{E}$ and the magnetic field $\mathbf{B}$ are continuous across interfaces, which aligns with Fraday's law (3.12), and Ampère-Maxwell Law (3.15). Mathematically this read:

$$\mathbf{n} \times (\mathbf{E}_1 - \mathbf{E}_2) = 0, \quad \text{and} \quad \mathbf{n} \times (\mathbf{H}_1 - \mathbf{H}_2) = 0 \tag{4.1}$$

Additionally, these elements appropriately model the behaviour of the normal components of electric displacement $\mathbf{D}$ and magnetic flux density $\mathbf{B}$, allowing for necessary discontinuities as described by Gauss's Laws for Electricity (3.4) and Magnetism (3.9):

$$\mathbf{n} \cdot (\mathbf{D}_1 - \mathbf{D}_2) = \sigma_f, \quad \text{and} \quad \mathbf{n} \cdot (\mathbf{B}_1 - \mathbf{B}_2) = 0 \tag{4.2}$$

These expressions ensure that the simulated fields accurately reflect both the boundary conditions and the physical laws governing electromagnetic interactions across different materials.

Each element is connected at points known as nodes, which are key to defining the element's geometry and the basis functions used for approximating the solution. This mesh of elements and nodes creates a framework that allows for the local approximation of the problem's governing equations, providing a systematic approach to solving complex problems by simplifying them into smaller, more manageable parts.

4.1.2 Choosing a Test Function

At the heart of FEM is the use of test functions or basis functions within each of these finite elements. These functions are used to approximate the solution over each element in the domain. Test functions are employed in the formulation of the FEM to multiply the differential equation being solved, facilitating the integration process across the domain, which is essential in deriving the weak form of the equation. Basis functions, on the other hand, are used to construct the approximate solution itself, they define the shape of the solution within each finite element.

Typically, these functions are polynomial due to their simplicity and computational efficiency. For instance, in a two-dimensional problem, a function of 1st order (linear) might be used, which takes the form $f(x, y) = ax + by + c$. The order of these polynomials directly influences the granularity, precision of the approximation, and the convergence rate of the FEM solution. Polynomials of lower order, such as 1st order, may suffice for problems with minimal variations within elements. In contrast, polynomials of higher order, such as 2nd order (quadratic) or 3rd order (cubic), are advantageous in scenarios where the solution exhibits more significant spatial variations and complexities. 2nd-order polynomials are commonly used in FEM, providing a balance between accuracy and computational efficiency.

The choice of polynomial order for each element, known as p-refinement, is important for controlling the solution's accuracy and computational requirements. The strategic combination of h-refinement, adjusting the mesh size, with p-refinement, and selecting the appropriate polynomial order, form the foundation of h-p finite element methods. This dual approach allows for optimized accuracy and efficiency in solving complex problems.

4.1.3 Weak Formulation

Once the problem is broken into elements and test functions are assigned, the next step involves converting the problem's governing differential equations into an integral form, known as the weak form. This conversion involves multiplying the differential

equation by a test function and integrating it over the domain. The weak formulation is crucial because it reduces the continuity requirements of the solution and its derivatives, allowing for numerical solutions that may exhibit discontinuities, such as at material boundaries. By converting to a weak form, the method broadens the types of functions that can be used as solutions, accommodating functions that are less smooth and thus more reflective of real-world scenarios where abrupt changes in material properties may occur. As an example, the differential equation in its strong form $-\nabla^2 u = f$ becomes $\int_\Omega \nabla v \cdot \nabla u \, d\Omega = \int_\Omega v f \, d\Omega$ in its weak form. Here v is the test function to multiply through the equation, and Ω is the domain over which the problem is defined.

4.2 Galerkin Method

The Galerkin method is a technique used within FEM to refine how we approximate the solution to a problem. It uses the same type of functions for the test functions and the solution's basis functions. This consistency helps to ensure that the discrepancies (residuals) between the predicted behaviour of the model and the requirements set by the weak form of the differential equations are minimized throughout the domain.

Essentially, the Galerkin method is about making sure that these residuals are as small as possible, in a way that they average out to zero when considered over the entire domain. This doesn't mean comparing to an exact solution but ensuring that the approximation behaves correctly according to the mathematical model and defined boundary conditions within the finite element framework.

To continue the example, in the Galerkin method, we approximate u as u_h, as a combination of basis functions ϕ_i:

$$u \approx u_h = \sum_{i=1}^{n} c_i \phi_i \tag{4.3}$$

where c_i are coefficients to be determined. The Galerkin method translates this into a set of algebraic equations by ensuring the residual is orthogonal to each basis function, leading to:

$$\sum_{i=1}^{n} c_i \int_\Omega v_j \mathcal{L}\phi_i \, d\Omega = \int_\Omega v_j f \, d\Omega \quad \text{for all } j \tag{4.4}$$

4.2.1 Assembly

In the Finite Element Method (FEM), after individual equations for each element are derived using the Galerkin method, the next critical step is the assembly of these equations to define the overall system. During the assembly, these local equations are systematically combined to form a comprehensive global system. Each element's equations are linked at nodes they share with adjacent elements, ensuring the model's overall continuity and coherence. This linkage involves aligning the local contributions in a larger matrix, called the global stiffness matrix, and a corresponding global force vector. The correct placement of these contributions depends on the connectivity of the nodes across the entire mesh.

The assembled global system—a large set of linear equations—encapsulates the behaviour of the entire domain under study. It is then solved using numerical techniques such as the conjugate gradient (CG) method for symmetric problems or Generalized Minimal Residual (GMRES) for non-symmetric problems. Solving this global system yields the solution to the problem, providing an approximation of how the entire structure or physical system behaves based on the imposed conditions and the physical laws governing the system.

4.3 Boundary conditions

Crucial to the FEM technique being used to solve this electromagnetic portion of the overall multi-physics problem is the correct application of boundary conditions. Here we will define what conditions are specified upon each of the boundary portions, annotated in Fig 3.2.

4.3.1 Wave guide port boundary conditions

The input boundary to the probe must be handled in an appropriate way such as to create excitation from incoming microwaves, whilst also acting to absorb reflected signals that may meet the boundary. Waveguide port boundary conditions (WPBC) have been described and implemented in commercial packages as an effective way to achieve this function [144]. Assuming that only TEM modes propagate within the

coaxial structure of the antenna [145] this boundary condition has been described in [146], and can be written as:

$$\mathbf{n} \times (\nabla \times \mathbf{E}) + P(\mathbf{E}) = U_{inc} \tag{4.5}$$

Where P and U_{inc} are

$$\begin{aligned} P(\mathbf{E}) = &- \gamma_0^{TEM} \mathbf{e}_0^{TEM} \iint_{S_p} \mathbf{e}_0^{TEM} \cdot \mathbf{E} \, \mathrm{d}S - \sum_{m=1}^{\infty} \gamma_m^{TE} \mathbf{e}_m^{TE} \iint_{S_p} \mathbf{e}_m^{TE} \cdot \mathbf{E} \, \mathrm{d}S \\ &- \sum_{m=1}^{\infty} \frac{-k^2}{\gamma_m^{TM}} \mathbf{e}_{tm}^{TM} \iint_{S_p} \mathbf{e}_{tm}^{TM} \cdot \mathbf{E} \, \mathrm{d}S \end{aligned} \tag{4.6}$$

$$\begin{aligned} U^{inc} = &\mathbf{n} \times (\nabla \times \mathbf{E}^{inc}) - \gamma_0^{TEM} \mathbf{e}_0^{TEM} \iint_{S_p} \mathbf{e}_0^{TEM} \cdot \mathbf{E}^{inc} \, \mathrm{d}S \\ &- \sum_{m=1}^{\infty} \gamma_m^{TE} \mathbf{e}_m^{TE} \iint_{S_p} \mathbf{e}_m^{TE} \cdot \mathbf{E}^{inc} dS - \sum_{m=1}^{\infty} \frac{-k^2}{\gamma_m^{TM}} \mathbf{e}_{tm}^{TM} \iint_{S_p} \mathbf{e}_{tm}^{TM} \cdot \mathbf{E}^{inc} dS \end{aligned} \tag{4.7}$$

Since we have earlier established that at the frequency of 2.45GHz used in MWA, only TEM mode waves propagate within the coaxial part of the antenna, therefore the TM and TE components can be removed. The electric field for the TEM mode in a coaxial cable is given by:

$$\begin{aligned} \mathbf{n} \times (\nabla \times \mathbf{E}) = &\gamma_0^{TEM} \mathbf{e}_0^{TEM} \iint_{S_p} \mathbf{e}_0^{TEM} \cdot \mathbf{E} \, \mathrm{d}S + \mathbf{n} \times (\nabla \times \mathbf{E}^{inc}) \\ &- \gamma_0^{TEM} \mathbf{e}_0^{TEM} \iint_{S_p} \mathbf{e}_0^{TEM} \cdot \mathbf{E}^{inc} \, \mathrm{d}S \end{aligned} \tag{4.8}$$

With the modal propagation constants and modal function defined as:

$$\mathbf{e}_0^{TEM} = \hat{r} \frac{1}{\sqrt{2\pi \ln(b/a)}} \frac{1}{\rho}, \quad \gamma_0^{TEM} = jk$$

The problem can be simplified further since we know the form that the electric field vector has in TEM mode in coaxial transmission lines. This gives:

$$\mathbf{n} \times (\nabla \times \mathbf{E}) = \gamma_0 (\mathbf{n} \times (\mathbf{n} \times \mathbf{E})) - 2A_0 \gamma_0 \mathbf{e}_0^{TEM} \qquad \text{on} \qquad \partial\Omega_1 \tag{4.9}$$

The boundary condition at the waveguide port acts as a Neumann-type condition. Neumann boundary conditions are a derivative or flux of the solution variable, whilst

Dirichlet boundary conditions prescribe the solution variable itself. In this case, the boundary condition specifies the behaviour of the electric field's derivatives at the boundary. In the context of electromagnetic simulations, these conditions involve manipulating derivatives like the curl of the electric field to model how electromagnetic waves are reflected and transmitted by the boundary.

4.3.2 Absorbing boundary conditions

For computational efficiency the domain is truncated through the application of an absorbing boundary condition around the edges of the tissue, primarily this boundary should absorb any incident wave without causing undesirable reflection back into the tissue. For this purpose a similar equation to the WPBC (4.9) is defined, excluding excitation of the input wave:

$$\mathbf{n} \times (\nabla \times \mathbf{E}) = \gamma_0 \left[\mathbf{n} \times (\mathbf{n} \times \mathbf{E})\right] \qquad \text{on} \qquad \partial\Omega_2 \tag{4.10}$$

The reasoning behind using this approach as opposed to implementing a perfectly matched layer is due to the increased complexity of both geometry/mesh generation and implementation within our framework.

4.3.3 Perfect Electrical Conductors

Metallic regions, such as those on the inner and outer conductors of a coaxial cable, are treated as perfect electrical conductors (PEC), meaning the material possesses a high density of free charges that can move with little resistance. When an external electric field is applied to such a conductor, these charges quickly rearrange themselves to produce a counteracting electric field, exactly cancelling the applied field within the conductor. This results in zero net electric field inside the perfect conductor.

On the surface of the conductor the situation differs slightly. Here, the redistributed charges neutralize only the tangential (parallel) components of the electric field, as these components would otherwise induce currents along the surface. The normal (perpendicular) component of the electric field at the surface, in contrast, does not induce parallel currents but rather affects the surface charge density itself. This component is

not neutralized but instead balances the external field to maintain the condition that no electric field penetrates into the conductor. Thus, any electric field at the surface of a perfect conductor must be perpendicular to it.

To enforce this behaviour in a FEM model, we apply the boundary condition given by:

$$\mathbf{n} \times \mathbf{E} = \mathbf{0} \qquad \text{on} \qquad \partial\Omega_3 \tag{4.11}$$

This equation ensures that the tangential components of the electric field are zero at the boundaries of the PEC. Since $\mathbf{n}$ is the normal vector to the surface, the cross product $\mathbf{n} \times \mathbf{E}$ isolates the tangential components of $\mathbf{E}$ at the surface. Setting this cross product to zero aligns with the physical requirement that no electric field exists parallel to the surface of a perfect conductor.

This condition is a classic example of a Dirichlet boundary condition,also known as fixed boundary conditions, which specify the value of a function at the boundary of the domain. In the context of electromagnetic fields, this involves setting the electric field to a specific value, such as zero, at the boundary.

4.3.4 Axis of symmetry conditions

In any symmetric structure, specific conditions must be met along the axis of symmetry to ensure that the electric field behaves consistently with the symmetry of the system. Notably, the radial component of the electric field, E_r, is zero on the axis of symmetry. This is because the system is symmetric, there is no preferential direction for the electric field to point radially, and any such direction would break the symmetry.

$$E_r = 0 \tag{4.12}$$

Additionally, the rate of change of the axial component of the electric field (E_z) with respect to the radial direction (r) must also be zero at the axis in order to maintain symmetry.

$$\frac{\partial E_z}{\partial r} = 0 \tag{4.13}$$

4.4 Weak formulation of the equations

Having established the necessary background on the FEM and discussed the governing equations and boundary conditions, we now turn our attention to the derivation of the weak form. The strong form of a partial differential equation, which requires solutions to satisfy the equation exactly at every point within the domain, will be our starting point. This section will detail the conversion from the strong form to the weak form, paving the way for its numerical implementation.

4.4.1 Electromagnetic - Weak form

Recalling the vector wave equation as written in (3.37): $\nabla\times\mu_r^{-1}\left(\nabla\times\mathbf{E}\right)-k_0^2\left(\varepsilon_r-j\frac{\sigma}{\omega\varepsilon_0}\right)\mathbf{E}=0$. This can be written in a generalised form using lumped coefficients, α and β, along with trial term $\mathbf{u}$, and source term S, as:

$$\nabla\times\beta\nabla\times\mathbf{u}+\alpha\mathbf{u}=S \qquad \text{in } \Omega \tag{4.14}$$

$$\mathbf{n}\times\mathbf{u}=f_D \qquad \text{on } \partial\Omega_D \tag{4.15}$$

$$\mathbf{n}\times\beta\nabla\times\mathbf{u}=f_N \qquad \text{on } \partial\Omega_N \tag{4.16}$$

Here Ω is the domain with $\partial\Omega_D$ and $\partial\Omega_N$ are boundaries upon which Dirichlet and Neumann boundary conditions are applied respectively. The choice of α, $\mathbf{u}$ and S depends on the problem consideration, and in this case: $\Omega=\Omega \quad \beta=\frac{1}{\mu_r} \quad \alpha=-k_0^2\left(\varepsilon_r-\frac{j\sigma}{\omega\varepsilon_0}\right) \quad \mathbf{u}=\mathbf{E} \quad S=0$.

We will now go from the strong form to the weak form. Since we have a vector-valued governing equation we form the scalar (dot) product of the terms with a vector-valued test function $\mathbf{v}$ whose tangential component vanishes on $\partial\Omega_D$. Integrating the resulting expression over Ω gives

$$\int_\Omega\left(\nabla\times\beta\nabla\times\mathbf{u}+\alpha\mathbf{u}\right)\cdot\mathbf{v}d\Omega=\int_\Omega S\cdot\mathbf{v}d\Omega. \tag{4.17}$$

Next we use the vector identity $\nabla\times\mathbf{a}\cdot\mathbf{b}=\nabla\cdot(\mathbf{a}\cdot\mathbf{b})+\nabla\times\mathbf{b}\cdot\mathbf{a}$ along with some rearrangement to give

$$\int_\Omega\left(\beta\nabla\times\mathbf{u}\cdot\nabla\times\mathbf{v}+\nabla\cdot\left(\left(\beta\nabla\times\mathbf{u}\right)\times\mathbf{v}\right)+\alpha\mathbf{u}\cdot\mathbf{v}\right)d\Omega=\int_\Omega S\cdot\mathbf{v}d\Omega. \tag{4.18}$$

The divergence theorem can be applied to the second term on the left-hand side and leads to

$$\int_{\Omega} \left(\beta \nabla \times \mathbf{u} \cdot \nabla \times \mathbf{v} + \alpha \mathbf{u} \cdot \mathbf{v}\right) d\Omega + \int_{\partial\Omega} \mathbf{n} \cdot ((\beta \nabla \times \mathbf{u}) \times \mathbf{v}) ds = \int_{\Omega} S \cdot \mathbf{v} d\Omega. \quad (4.19)$$

Finally, through the properties of the scalar and vector products, we have the weak form of the problem as

$$\int_{\Omega} \left(\beta \nabla \times \mathbf{u} \cdot \nabla \times \mathbf{v} + \alpha \mathbf{u} \cdot \mathbf{v}\right) d\Omega = \int_{\Omega} S \cdot \mathbf{v} d\Omega - \int_{\partial\Omega} \mathbf{v} \cdot (\mathbf{n} \times \beta \nabla \times \mathbf{u}) ds. \quad (4.20)$$

4.4.2 Implementation

The weak form of the problem can be written as a matrix system in the shape of:

$$\mathbf{A}\mathbf{u} = \mathbf{f} \quad (4.21)$$

Where we can define $\mathbf{A}$ and $\mathbf{f}$ from Eq. (4.20):

$$\mathbf{A} = \int_{\Omega} \left(\beta \nabla \times \mathbf{u} \cdot \nabla \times \mathbf{v} + \alpha \mathbf{u} \cdot \mathbf{v}\right) d\Omega + \int_{\partial\Omega} \mathbf{v} \cdot (\mathbf{n} \times \beta \nabla \times \mathbf{u}) ds \quad (4.22)$$

$$\mathbf{f} = \int_{\Omega} S \cdot \mathbf{v} d\Omega \quad (4.23)$$

Specifying Dirichlet conditions at specific boundaries allows the solution $\mathbf{u}$ to be expressed as the sum of unknown values $\mathbf{u}_0$ and values at dirichlet boundaries $\mathbf{u}_D$,

$$\mathbf{u} = \mathbf{u}_0 + \mathbf{u}_D. \quad (4.24)$$

So (4.21) is adapted to solve for $\mathbf{u}_0$,

$$\mathbf{A}(\mathbf{u}_0 + \mathbf{u}_D) = \mathbf{f} \rightarrow \mathbf{A}\mathbf{u}_0 = \mathbf{f} - \mathbf{A}\mathbf{u}_D. \quad (4.25)$$

Which we will use within our chosen FEM solver to compute this portion of the overall multi-physics problem.

4.4.3 Electromagnetic test case

To evaluate the effectiveness of boundary condition implementations in a coaxial transmission line simulation, we utilize a simplified model under three distinct termination conditions: shorted, open, and matched load. Each scenario is designed to verify

the application of the electromagnetic FEM formulation and solver, along with the effectiveness of the WPBC on the coaxial input surface, absorbing boundary condition at the terminal end of the transmission line, and PEC condition on the metallic surfaces of the conductors.

According to electromagnetic theory, a short-circuited coaxial transmission line should display a distinct standing wave pattern with nodes, where both the real and imaginary components of the electric field are zero, and antinodes, where these components reach their maximum. As described by David M. Pozar in "Microwave Engineering" (4th Edition, Wiley), this pattern emerges because the boundary condition at the short circuit forces the electric field to zero, leading to constructive and destructive interference between the incident and reflected waves at predictable quarter-wavelength intervals. The wavelength λ inside the transmission line depends on the frequency (f = 2.45GHz), the relative permittivity ($\varepsilon_r = 2.03$ for this example case) of the dielectric, and the wave speed of light ($c = 3e^{10}$m/s), giving $\lambda = c/f\sqrt{\varepsilon_r} = 85.94mm$. The magnitude of the field, calculated as $\sqrt{\mathbf{E}_{real}^2 + \mathbf{E}_{imag}^2}$, manifests as zero at nodes and peaks at antinodes. To verify this, we perform FEM simulations, plotting both the real and imaginary components of the electric field along a line parallel to the transmission line's axis, within the dielectric medium.

In our simulations, this expected behaviour is observed, showcasing nodes and antinodes at calculated locations that perfectly align with the theoretical expectations for a line operating at 2.45 GHz in a medium with permittivity 2.03. Nodes, specifically located at distances $\lambda/2 = 42.97mm$ and $\lambda = 85.94mm$, and antinodes observed at $\lambda/4 = 21.49mm$ and $3\lambda/4 = 64.45$ from the terminal end (see Fig 4.4.3), validate the accuracy of our model and the effectiveness of the boundary condition implementation. These results not only confirm the reliability of the FEM solver but also underscore its capability to replicate established theoretical behaviours in electromagnetic wave propagation.

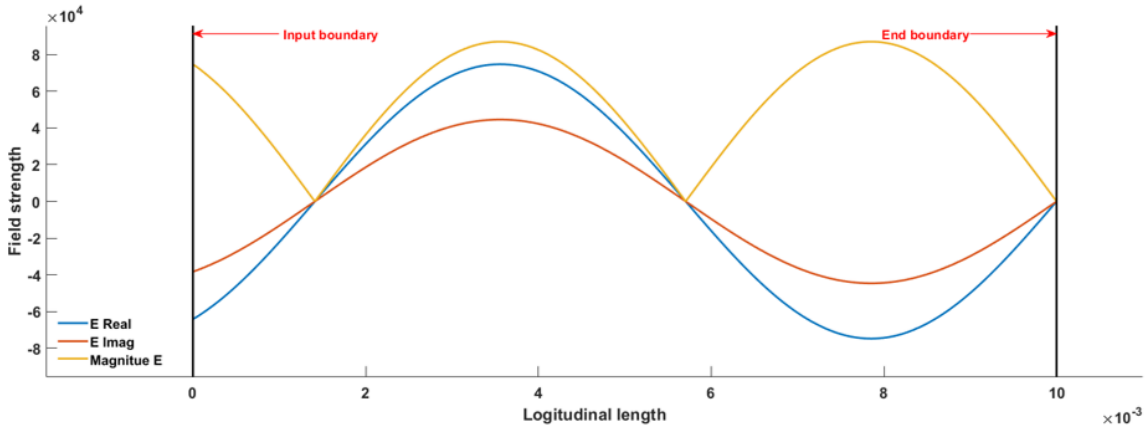

Figure 4.1: A shorted coaxial case, where the terminal end is simulated to be shorted. This results in a standing wave formation within the transmission line.

Conversely, an open-circuited termination shows a similar standing wave pattern but with the positions of nodes and antinodes reversed. Antinodes occur right at the open end, and nodes are spaced a quarter-wavelength apart. This pattern results from the boundary condition at the open end, which does not constrain the electric field, allowing it to reach maximum values, whereas the reflected wave from the end causes destructive interference at specific intervals, creating nodes. Again, simulated data from this configuration can be seen in Fig 4.4.3, where the expected behaviour is precisely replicated, showing antinodes at the open termination and nodes at intervals that conform to the quarter-wavelength rule.

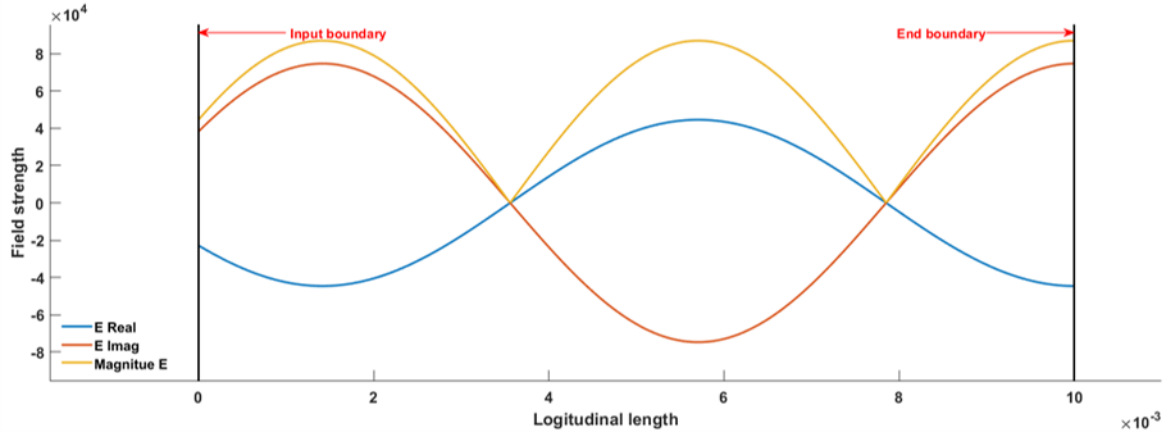

Figure 4.2: An open coaxial case, where the terminal end allows waves to freely reach their maximum

In an ideal matched load condition, theoretical principles predict that the impedance of the load exactly matches the transmission line's characteristic impedance, thereby

eliminating reflections at the terminal end. As a result, unlike the open or shorted cases, there is no formation of standing waves, which typically arise from the superposition of incident and reflected waves. Instead, the electric field maintains the form of a travelling wave, characterized by a sinusoidal variation consistent with the incident wave's profile.

To simulate this, we apply an absorbing boundary condition at the terminal end of the coaxial line in our FEM model. This boundary condition is designed to mimic a perfectly matched load, allowing the wave to pass as if the transmission line were infinitely long. The FEM results, as illustrated in Fig 4.4.3, confirm the absence of reflections and the continuity of the wave's behaviour, consistent with a load that perfectly absorbs the wave without any reflection. This simulation outcome aligns with the theory and provides confidence in the boundary condition's correct implementation and the FEM model's ability to accurately depict a matched termination in a coaxial transmission line.

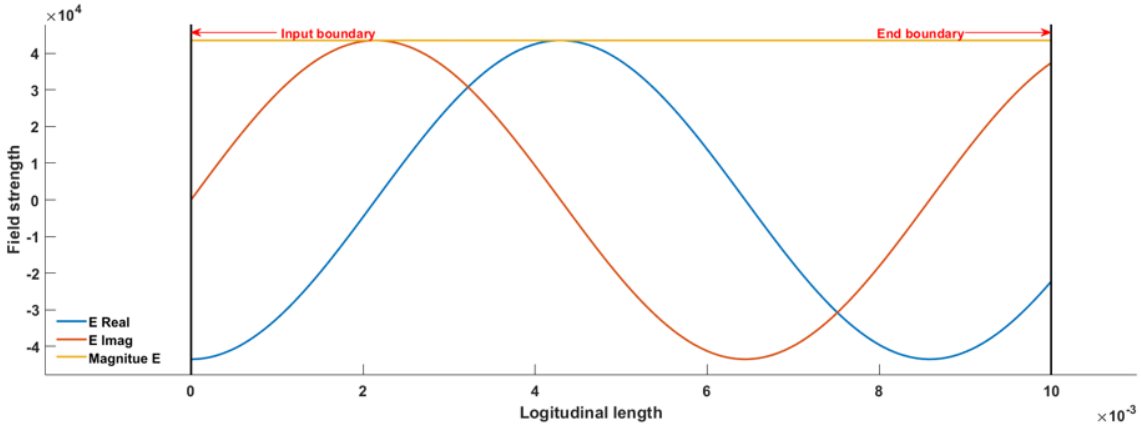

Figure 4.3: A perfectly matched case, where the terminal end is simulated to be absorbing, therefore no wave reflections are exhibited and the waves are unimpeded.

4.4.4 Bioheat Weak formulation

A weak form is also needed for this partial differential Eq (3.60), similarly to the electromagnetic wave equation, an equation with trial function term $\hat{T}$ is multiplied by a test function w and integrated over domain,

$$\int_{\Omega} \left(\rho_l C_l \frac{\partial \hat{T}}{\partial t} \right) w d\Omega - \int_{\Omega} \left[\nabla \cdot (k_l \nabla \hat{T}) \right] w d\Omega = \int_{\Omega} F w \, d\Omega. \tag{4.26}$$

Source and sink terms in Eq (3.60) have been grouped into a single variable F from here forward. The second term in the equation has a secon-order derivative which can be converted into first-order using the divergence theorem and identity $\nabla \cdot (\phi u) = \phi(\nabla \cdot u) + (\nabla \phi) \cdot u$. Applying these changes gives the weak form of the problem,

$$\int_\Omega \left(\rho C \frac{\partial \hat{T}}{\partial t}\right) w \; d\Omega - \int_{\partial s} \left[w(k_l \nabla \hat{T})\right] \cdot \mathbf{n} \; ds + \int_\Omega (\nabla w) \cdot (k_l \nabla \hat{T}) \; d\Omega = \int_\Omega F w \; d\Omega. \tag{4.27}$$

where ∂s is some part of the boundary of Ω. Neumann boundary conditions can be implemented through this surface integral part of the weak form, on the external surfaces of the tissue boundary an insulating condition is set through

$$(k_l \nabla T) \cdot \mathbf{n} = 0 \qquad (\partial \Omega_3). \tag{4.28}$$

This completes the necessary equations for computing the thermal side of the multi-physics problem.

4.4.5 FEM equations summary

Compiling all of these components, the entire non-linear coupled system can be summarised by the equations:

$$\nabla \times \beta \nabla \times \mathbf{E} + \alpha(T)\mathbf{E} = \mathbf{S} \qquad \text{in } \Omega, \tag{4.29a}$$

$$\mathbf{n} \times (\nabla \times \mathbf{E}) = \gamma_0 \left[\mathbf{n} \times (\mathbf{n} \times \mathbf{E}) - 2\mathbf{E}_{inc}\right] \qquad \text{on } \partial\Omega_1, \tag{4.29b}$$

$$\mathbf{n} \times (\nabla \times \mathbf{E}) = \gamma_0 \left[\mathbf{n} \times (\mathbf{n} \times \mathbf{E})\right] \qquad \text{on } \partial\Omega_2 \tag{4.29c}$$

$$\mathbf{n} \times \mathbf{E} = 0 \qquad \text{on } \partial\Omega_3, \tag{4.29d}$$

$$\rho C \frac{\partial T}{\partial t} = \nabla \cdot (k_l \nabla T) + Q_s(\mathbf{E}) \qquad \text{in } \Omega, \tag{4.29e}$$

$$(k_l \nabla T) \cdot \mathbf{n} = 0 \qquad \text{on } \partial\Omega_3, \tag{4.29f}$$

where Ω denotes the computational domain of interest at this stage $\subset R^3$, whilst $\partial\Omega_1$, $\partial\Omega_2$ and $\partial\Omega_3$ in Fig 4.4 represent the Dirichlet, Neumann and mixed boundaries respectively. Here the grouped coefficients are, $\beta = \frac{1}{\mu_r}$,
$\alpha = -k_0^2 \left(\varepsilon_r(T) - \frac{j\sigma(T)}{\omega \varepsilon_0}\right), \quad \mathbf{S} = 0.$

4.5 Coupled system

As mentioned in the previous chapter, properties of biological tissue can be highly temperature sensitive and therefore any simulation should account for this to increase the accuracy of results. In this analysis, we will consider the temperature dependence of tissue dielectric properties, namely the electrical permittivity and effective conductivity. Experimental studies on bovine liver samples have allowed the construction of empirical relations that estimate the changes as a function of temperature [46, 147]. Both of these studies used the same sigmoid type function to model the dielectric behaviour, the coefficients we use in our study are taken from the Ji paper [46], and are shown in table 4.1.

Relative permittivity (ϵ_r)			**Electric conductivity** (σ [S/m])		
α_1	α_2	α_3	β_1	β_2	β_3
0.0764	82.271	48.391	0.0697	85.375	2.173

Table 4.1: Summary of dielectric properties and electric conductivity with respect to temperature.

$$\varepsilon_r(T) = \alpha_3 \left(1 - \frac{1}{1 + \exp(\alpha_1(\alpha_2 - T))}\right) + 1 \tag{4.30}$$

$$\sigma(T) = \beta_3 \left(1 - \frac{1}{1 + \exp(\beta_1(\beta_2 - T))}\right) \tag{4.31}$$

Here, α_{1-3} and β_{1-3} are the regression coefficients found in [46] and T is the temperature (°C). Both properties express a decreasing trend with an increasing temperature. With this information, electric field strength calculated through (3.37) becomes temperature dependent as

$$\nabla \times \mu_r^{-1} (\nabla \times \mathbf{E}) - k_0^2 \left(\varepsilon_r(T) - j\frac{\sigma(T)}{\omega\varepsilon_0}\right)\mathbf{E} = 0. \tag{4.32}$$

This dependency therefore influences the temperature computed in the bioheat model shown in Eq. (4.33), as it becomes

$$\rho_l C_l \frac{\partial T}{\partial t} = \nabla \cdot (k_l \nabla T) + Q_p + \frac{\sigma|\mathbf{E}(T)|^2}{2} \qquad \text{in}\Omega \tag{4.33}$$

Equation (4.32) can then be solved to compute the electric field in the tissue.

Since the EM equation is formulated in the frequency domain, it inherently computes a steady-state solution for each timestep. This time-independent approach circumvents the need for the impractically small time steps that would be required for solving these equations in the transient domain. By doing so, it simplifies the integration with the thermal processes, which are handled separately in the time domain using the implicit Euler scheme.

The simulation workflow, as shown in Fig 4.4, involves calculating the electric field first using the frequency domain version of the EM equation (4.32). Following this, the temperature distribution is determined through the bioheat equation (3.60). After updating the thermal properties based on the new temperature profiles, the simulation proceeds to the next time step.

To ensure the accuracy of the simulation, convergence at temperature-sensitive points within the domain is monitored. Simulations were run at reducing timesteps adjusted until the temperature changes at these points between timesteps fell below the threshold of 0.1°C at the conclusion of ablation. This convergence test showed convergence is reached at a time step of 0.01 seconds. This step ensures that the results are consistent and the simulation remains stable as it integrates over time.

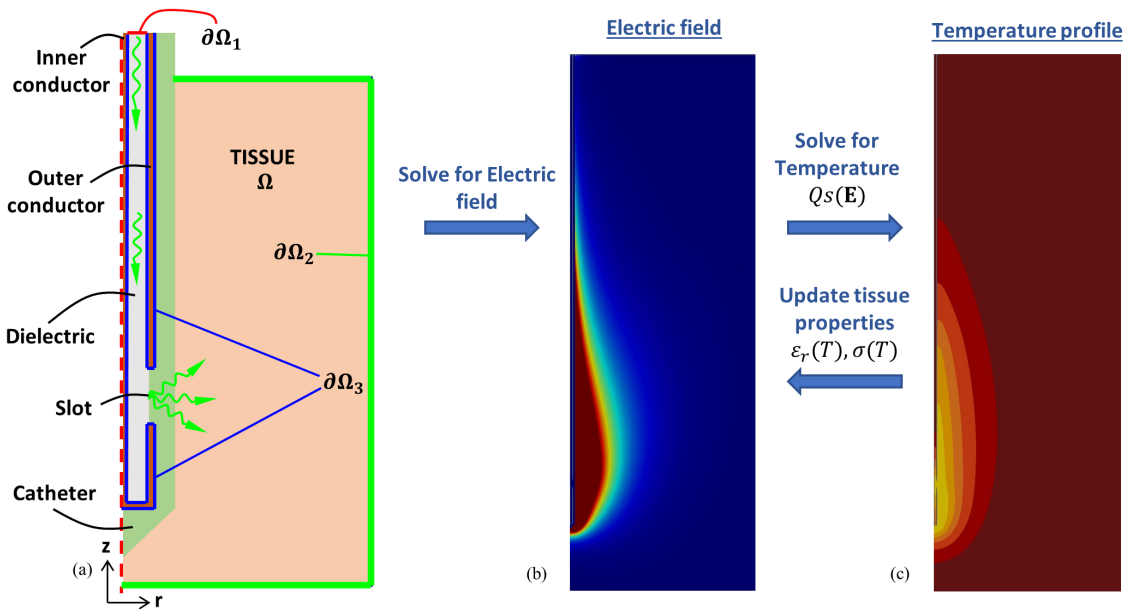

Figure 4.4: Overview of the framework used to solve the coupled problem. (a) The axisymmetric domain Ω is made up of tissue and the probe constituent materials, catheter, conductors and dielectric. The three boundaries upon which conditions will be applied are shown by $\partial\Omega_1$, $\partial\Omega_2$ and $\partial\Omega_3$. EM waves propagate along the probe, from the input at $\partial\Omega_1$ through the dielectric to the slot where they are able to radiate into the catheter and tissue. (b) Typical shape of the electromagnetic field pattern created by simulated MWA probes. (c) Corresponding temperature distribution after a period of ablation.

4.5.1 Solving approach

The open-source NGSolve library was chosen as a foundation to solve this coupled system by FEM hp finite elements [148], this platform was chosen over the more commonly used commercial software for this type of multi physics modelling, because of the flexibility and accessibility afforded to NGSolve through its open source license. Other open source platforms do exist for FEM multiphysics modelling, FEnics was considered but at the time of starting this project there were limitations with the use of complex numbers within FEM formulations, which made modelling of the electromagnetics part of this problem increasingly difficult [149]. Geometries of each probe and surrounding tissue domain are created and meshed in the GMSH software package, an open-source package that allows geometries to be readily defined and

meshed by various user defined methods. The file formats are readily integrated with the choice of FEM solver we have selected. An unstructured mesh of triangular elements is created that allows refinements near the slot in the antenna to be defined, where higher gradients within the electric field are observed. As briefly mentioned earlier, the electromagnetic equation is discretised by third-order H(Curl) elements, such elements more naturally allow the electric field boundary conditions to be applied and are commonplace in electromagnetic FEM modelling. This is because discontinuity in the normal component of the electric field can occur at material interfaces or around boundaries of sharp corners, a characteristic that would not be enforced by Lagrange element based FEM solutions. H(Curl) elements allow this discontinuity of normal components across interfaces, whilst maintaining continuity in the tangential components. Second-order Lagrange elements were used for discretising the bioheat equation on the same mesh using NGSolve [150].

4.6 Validation

These types of MWA simulations are typically simulated using commercial multiphysics packages. A platform that enables mesh generation and a broad range of multi-physics couplings, but comes at a financial expense which therefore limits accessibility in some cases, like ours. To validate our open-source approach we chose to select existing results from the literature that use a commercial multiphysics package and run comparative simulations that will allow us to assess the models' performance. Added to this, we include experimental data acquired under the same conditions, for a comparison to real-world applications of MWA.

4.6.1 Electromagnetic model

Firstly, validation of the electromagnetic model involves measuring the SAR magnitude through the domain. More specifically, plotting the values along a line parallel to the probe axis at a distance of 2.5 mm. The resulting line plot of SAR intensity with z coordinate can be directly compared to the equivalent simulation carried out for a single slotted antenna with surrounding catheter, on commercial software, as per [151]. The antenna and catheter dimensions, along with material properties are described in

table 4.2. Simulated at 10 W power input, the SAR comparison is shown in Fig 4.6.

Materials	**Dimensions (mm)**	**Parameters**	**Values**
Inner conductor radius	0.145	Relative permittivity, liver	43.03
Dielectric radius	0.470	Electric conductivity, liver	1.69 [S/m]
Outer conductor radius	0.595	Thermal conductivity, liver	0.56 [W/(m*K)]
Catheter radius	0.895	Relative permittivity, dielectric	2.03
Slot width	1.000	Relative permittivity, catheter	2.6
Slot position	5.000	Microwave frequency	2.45 [GHz]
Metal	0.595	Input microwave power	10 [W]

Table 4.2: Table of Materials and Parameters used in the SAR validation [151]

The results show good agreement along the length of the probe, with small differences around the point closest to the probe slot which is responsible for the peak in SAR, this difference can be justified by differences in meshing density at this point and differences associated with the digitization of data. The strong agreement between datasets through the mid portion of the probe length suggests that our electromagnetic model performs the same computation as the commercial software, and the matchedness close to the boundaries at 0 and 80mm gives confidence that the absorbing boundary conditions enforced in our model achieve the same results as those within COMSOL.

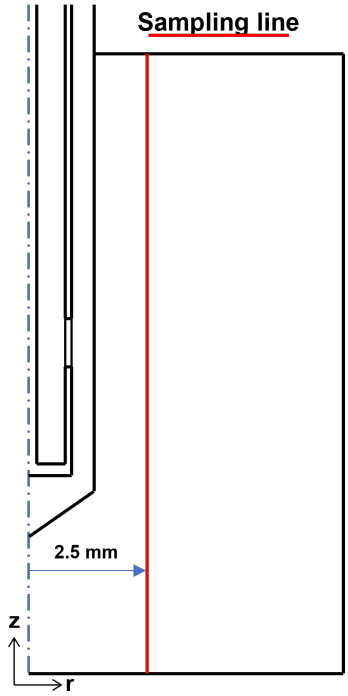

Figure 4.5: The single slotted antenna with catheter illustration that represents the geometry used in this validation as also seen in [151], annotated with the line along which SAR is measured.

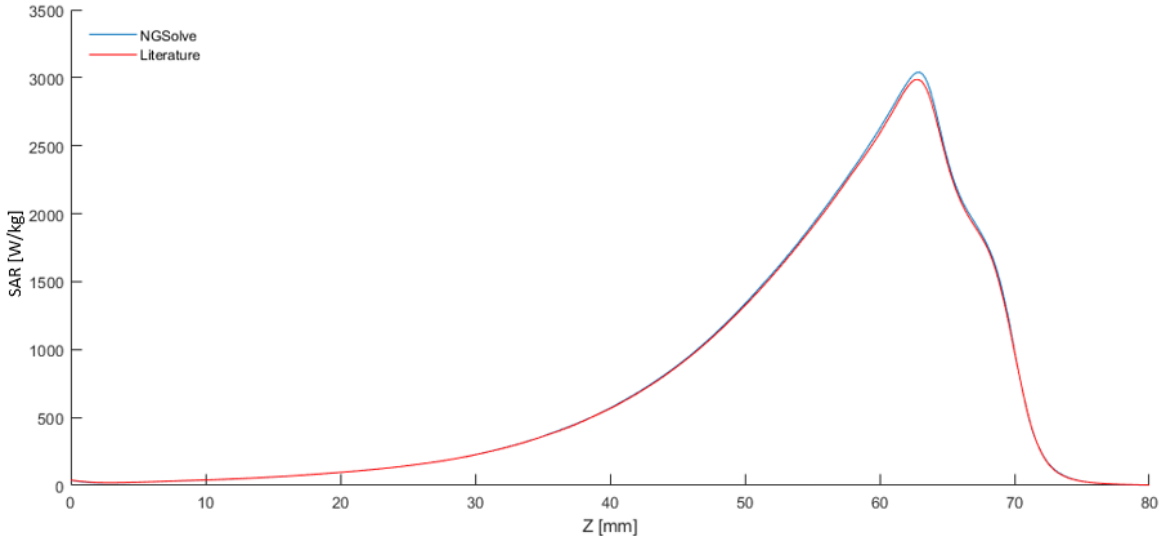

Figure 4.6: Comparison of simulated results to the numerical solution found through commercial software conducted ourselves [151]. Here, Z = 0 is at the probe insert end, Z = 65 is adjacent to the probe slot, the probe tip at Z = 70, and Z = 80 is the end of the tissue domain.

4.6.2 Coupled model

In order to validate the coupled model, a comparative simulation was conducted using a methodology similar to that described in [126] and in alignment with other studies such as [93]. A single-slotted probe geometry was replicated, with material parameters set to match those used in the referenced comparative study, these dimensions and material parameters are shown in Tables 4.4 and 4.3.

Property	**Liver**	**Copper**	**Teflon**
Relative permittivity	43	–	21
Electrical conductivity [S/m]	1.69	–	0
Thermal conductivity [W/m°C]	0.5	400	0.24
Mass density [kg/m^3]	1060	8700	1200
Specific heat capacity [J/kg°C]	3600	385	1050

Table 4.3: A summary of the relevant variables in the setup of the comparative simulation.

Materials/Parameters	**Dimensions/Values**
Inner conductor radius	0.145 mm
Dielectric radius	0.470 mm
Outer conductor radius	0.595 mm
Catheter radius	0.895 mm
Plastic template	2.5mm
Plastic cutting board	5 mm
Radius of layers	1.25 mm
Insertion depth	30 mm
Slot position	8 mm
Slot width	1 mm
Tissue width	40 mm
Tissue height	40 mm

Table 4.4: Materials and Their Dimensions

This included a slot located 8mm from the end of the probe, inserted 30mm into tissue

that is 40mm wide and 40mm deep, with a plastic block at the base and surface of the tissue for stability during experimentation. An ablation was simulated for 150s at a power setting of 75W, with experimental data recorded at 5s intervals. Temperature measurements were specifically taken at radial distances of 4.5mm and 9.5mm from the centre of the slot, aligning with the depth level of the slot. These measurement points are illustrated in Fig 4.7. The simulation results are shown in figures 4.8 and 4.9, which displays the temperature changes throughout the ablation process and demonstrates good agreement with the established model.

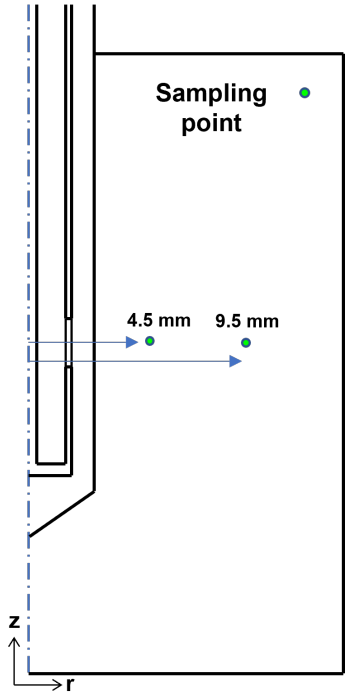

Figure 4.7: The single slotted probe illustration that represents the geometry used in this validation, annotated with measurement points 4.5mm and 9.5mm from the centre of the slot at which temperature is sampled.

Additionally, in our modelling tests, we explored the extended bioheat model introduced in [126], which adapts the traditional bioheat equation to include the latent heat of vaporization absorbed by the tissue. This adaptation is crucial for simulating high-temperature ablation processes, as it incorporates a modified specific heat capacity that adjusts based on changes in water content due to temperature. The model proposes specific equations to relate water content directly with temperature changes.

We attempted to integrate this model into our simulation by way of adopting the equations for tissue water content as a function of temperature presented in [126], which were fitted based on experimental data collected in their earlier work [106]. However, we found that these equations did not accurately reflect the behaviour illustrated in their graphs. Consequently, we turned to the subsequent research published in [147], which provides an equivalent function for water content based on models that are fitted to their own experimental data. These functions, while similar in form to those in [126], accurately replicate the expected changes in water content with rising temperatures, leading us to adopt them for our simulations.

We can now evaluate the presented models in the literature against our own models, with a comparison to the experimental data under the same conditions. This is shown in figures 4.8 and 4.9, which show temperature changes at 4.5mm and 9.5mm from the probe surface respectively.

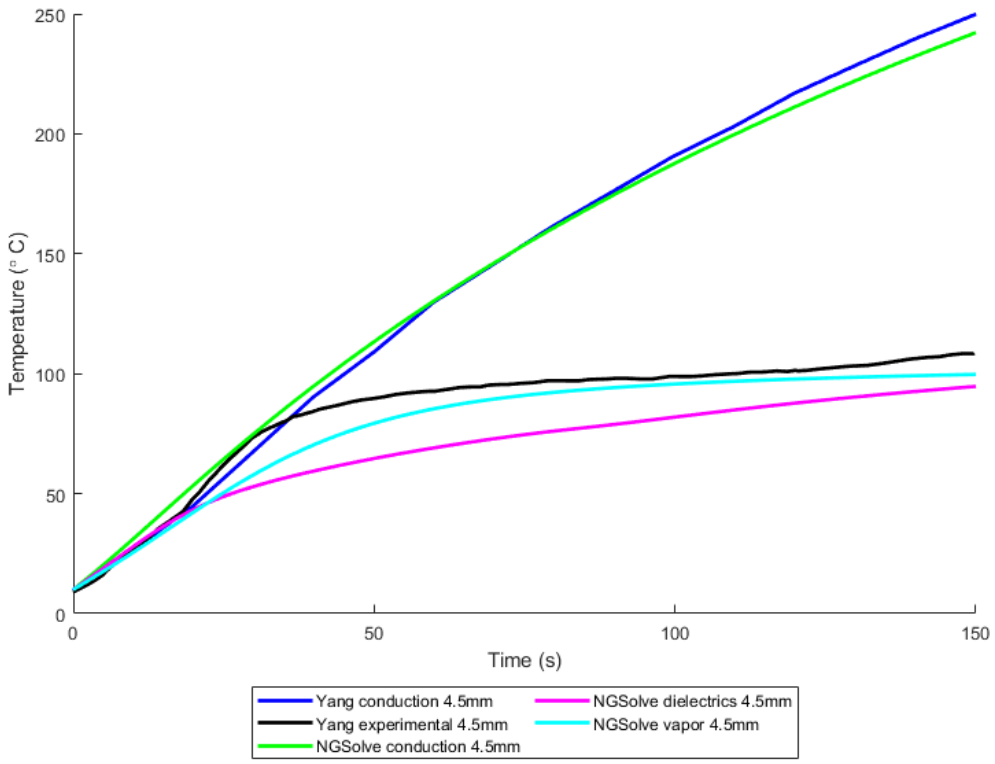

Figure 4.8: Experimental data of temperature at 4.5mm from the probe surface, in line with the antenna slot, is plotted in black. Similarly, simulated temperature data from a conduction model is shown (dark blue) from work presented in [126]. Data shown in the green line is the equivalent conduction model replicated using our open-source framework with NGSolve. Furthermore, the light blue line shows an implementation of the water vapour model as it exists in [147], and the magenta line shows data generated using the temperature-dependant dielectric model implemented through our weakly coupled framework.

At the 4.5 mm measurement point, good agreement is seen between the conduction model presented in [126] and our simulations. This level of agreement is similar to that depicted in [93]. However, it is apparent that the conduction model alone does not compare well to the experimental data beyond 30 seconds, where temperature approaches 100 °C, this is due to the static parameters used within the conduction model which do not reflect the change to tissue properties with increasing temperature. On the other hand, the water vapour model more closely follows the experimental

data in that the gradient reduces as the temperature approaches 100 °C, as a result of the adaptations to the specific heat capacity of the tissue to reflect the latent heat of vapourisation of tissue water. Furthermore, simulations using the temperature-dependent tissue dielectric properties also show better agreement with the experimental data compared to the conduction model. Similar temperature projections are seen using the latent heat model and temperature-dependent dielectric model, but there is still some disagreement with the experimental data, which can be attributed to the multiple other phenomena occurring within the tissue which are not accounted for in these models, such as changes to thermal conductivity, tissue contraction, and the isotropic nature of the tissue which is assumed to be homogeneous with the 2D modelling framework.

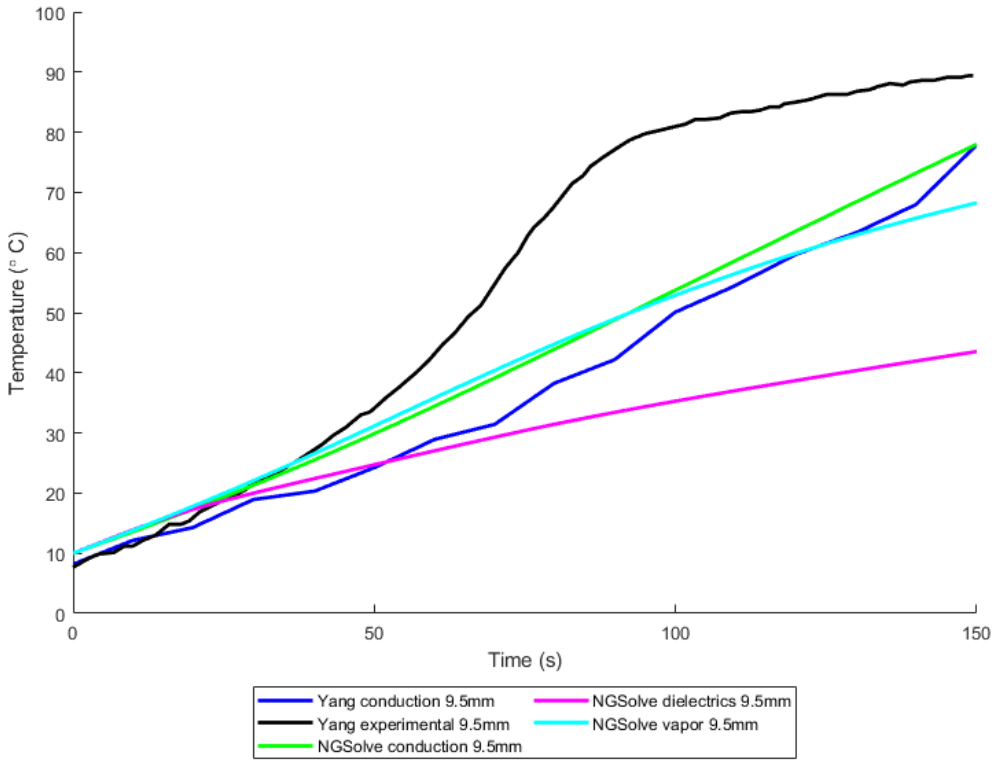

Figure 4.9: Experimental data of temperature at 9.5mm from the probe surface, in line with the antenna slot, is plotted in black. Similarly, simulated temperature data from a conduction model is shown (dark blue) from work presented in [126]. Data shown in the green line is the equivalent conduction model replicated using our open-source framework with NGSolve. Furthermore, the light blue line shows an implementation of the water vapour model as it exists in [147], and the magenta line shows data generated using the temperature-dependant dielectric model implemented through our weakly coupled framework.

Looking at the equivalent data at 9.5 mm from the probe in Fig.4.9, it is again seen that there is good agreement between the computational models presented in [126] and the FEM model presented in this thesis. However, unlike at the 4.5mm measurement point, further from the probe we see that experimental data indicates higher temperatures than those indicated in any of the models. This increase in temperature is in part due to the effects of the vapourised tissue water recondensing at cooler regions away from the higher-temperature tissue close to the probe. This condensation of hot

vapour heats the tissue and is not accounted for in the conduction model or variable dielectric properties model. These results were similarly observed in [46], where the accuracy of the models using the sigmoidal dielectric model decreased with increasing distance from the ablation probe. This reduction in model precision is attributed to the inadequate representation of thermal conductivity changes and the effects of tissue vaporization.

A further comparison is made to experimental data from a cooled probe concept in chapter 6.

4.6.3 Mesh convergence

A Mesh convergence study investigated the optimal mesh element size that should be used in our simulations, using relative error defined as Relative error $= \frac{|M-C|}{|C|}$, where M is the measured value, and C is the converged value found by running the highest mesh and polynomial order possible. In addition, NGSolve allows flexibility over the polynomial order of the elements used during the finite element computation, therefore convergence across a range of p-orders is also explored. The metric on which we base this convergence is a scalar quantity, the integral of the magnitude of the electric field across the entire domains. The results are shown in Fig 4.10.

It could be expected that increasing convergence rates will increase with increasing polynomial order, however, our results only show this behaviour at higher element mesh element numbers. Although the rate of convergence might not significantly increase with increased polynomial order, there is a benefit in the lower starting error achieved by increasing p. Based on this we selected meshes for our various geometries that sufficiently balanced accuracy and computational expense, utilising 3rd-order polynomials. An example of the meshing used for the internally cooled probe is shown in Fig 4.11.

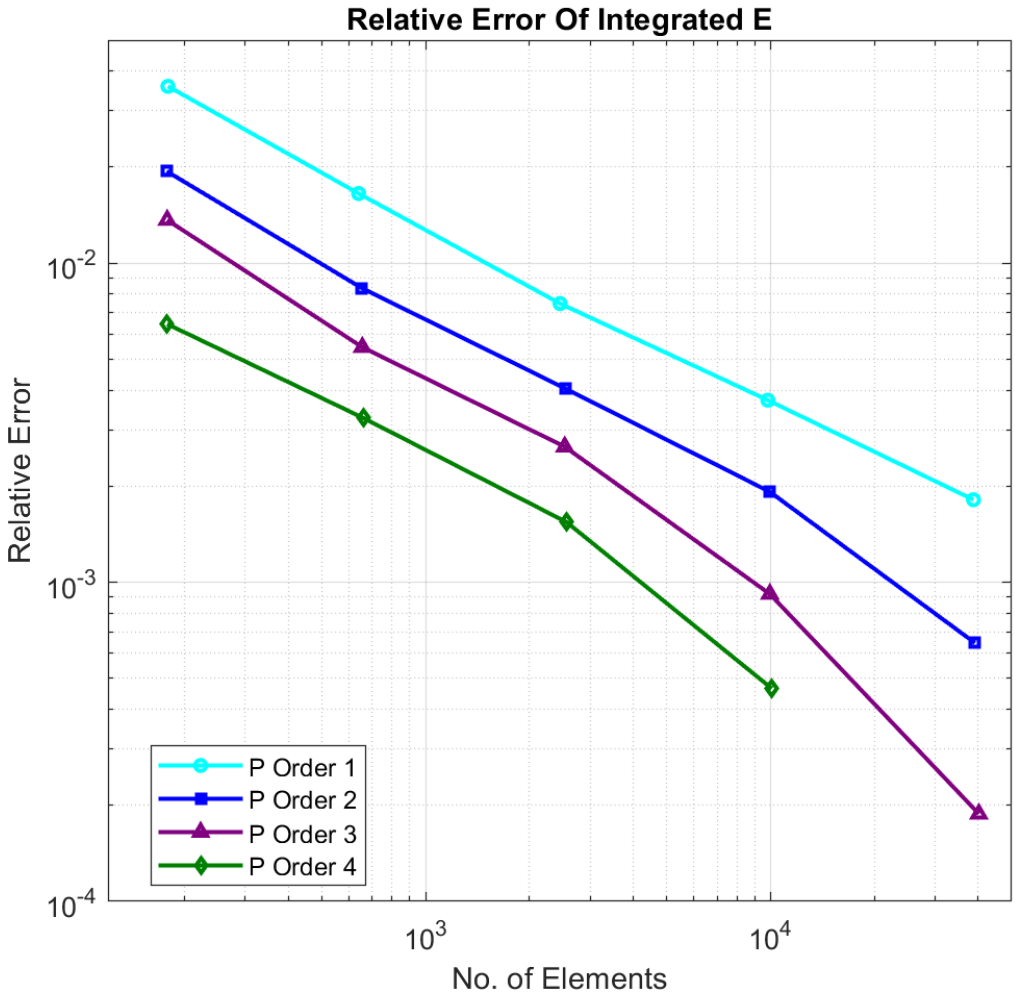

Figure 4.10: The results of a hp-convergence investigation are shown, with higher order elements showing convergence at a lower overall number of mesh elements.

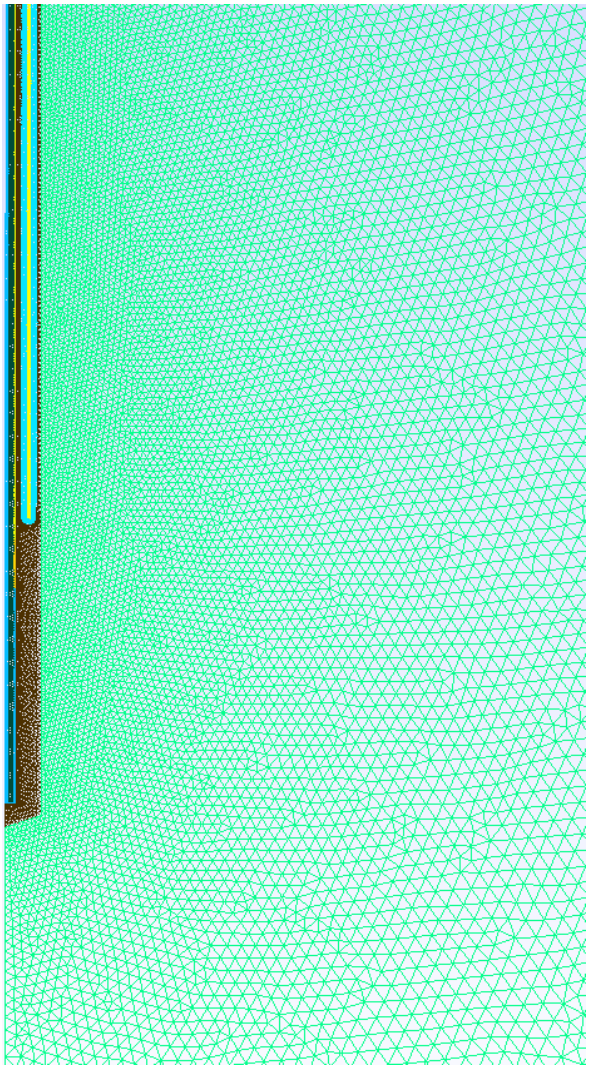

Figure 4.11: An example of the mesh used in the internally cooled probe design. With around 40 thousand triangular elements in this case, the same mesh is used for both the electromagnetic and heat transfer problems, utilising different p-orders to solve each problem.

5 Transient changes in microwave ablation

5.1 Introduction

The electric field and SAR generated by MWA antennas often result in an elliptical or tear-drop shaped temperature profile, which can be problematic when treating spherical tumors. This mismatch between the ablation zone and the tumor shape may lead to incomplete heating of the target area or unintended damage to surrounding healthy tissues, as depicted in Fig 2.2.b, thereby increasing the chances of complications [152]. In contrast, spherical heating patterns have the potential to create larger ablation zones, facilitating the treatment of more extensive disease volumes [153]. The shape and magnitude of the electromagnetic field pattern produced within the tissue by the ablation probe directly influence the shape and extent of heating. Consequently, the design of MWA antennas should consider the clinical goal of creating an ablation profile that closely matches the tumor shape.

5.1.1 impedance matching

Another design consideration in microwave ablation systems is the efficient transfer of input power from the probe into the tissue. This efficiency can be quantified by calculating the input reflection coefficient, or S_{11}, of a given probe. A high S_{11} value indicates a high level of reflection, meaning that a significant portion of the microwave energy is not absorbed by the target tissue but is instead reflected back up the feed line. This reflection can cause internal heating of the coaxial feed lines within the probe structure, potentially leading to unintended heating of tissues or causing structural damage that affects the operation of the device itself.

The mechanism behind this heating relates to the imperfections in the materials used in the feed lines. Typically, metals and dielectrics in the coaxial cables are considered perfect conductors and insulators in theoretical models, as we have laid out in our modelling framework. However, in practice, these materials are not perfect.

Metals have finite resistivity, and dielectrics exhibit some degree of lossiness. These imperfections mean that some of the microwave energy carried and reflected in the feed line is converted into heat. This conversion occurs through resistive heating in the metals and dielectric losses in the insulators, which are not captured in our idealized modeling framework, but are a worthwhile consideration when evaluating probe efficiency. As the reflected energy increases, more heat is generated due to these material imperfections, potentially compromising the probe's functionality and safety.

It is crucial, therefore, to focus on impedance matching to minimize S_{11}. Effective impedance matching ensures that the probe's impedance closely matches that of the target tissue, maximizing power transfer into the tissue and minimizing power reflection. This can be assessed both in the simulation and measurement phases. In simulations we can compute the reflection coefficient analytically using the resolved electric field and the known input field, measurements in practical settings, often done using a network analyzer, confirm the impedance matching by directly measuring S_{11} under conditions that mimic clinical usage.

In microwave ablation, the geometry of the ablation probe is crucial for ensuring effective energy transfer into the tissue. in the case of a monopole antenna specifically, the length of the probe is key to achieving resonance at a quarter wavelength ($\lambda/4$) of the microwave energy. This specific length allows the probe to resonate with the microwave frequency, creating a condition where the probe's impedance is optimally matched to the impedance of the tissue.

When a probe is tuned to $\lambda/4$, it reaches a state of resonance where its capacitive and inductive reactances are balanced, minimizing the reactive components of its impedance. This balance is significant because it reduces the electromagnetic reflections at the interface between the probe and the tissue, allowing more microwave energy to be absorbed rather than reflected. Essentially, the probe's length, when set to a quarter wavelength, aligns its electrical properties to those of the surrounding medium, thereby optimizing the transfer of energy.

5.1.2 shape

Several variations of MWA antenna concepts have been proposed in search of improved effectiveness, including the monopole [104], single slotted [79], double slotted [90], and sleeved antennas [106, 107]. Studies have investigated different probe concepts both numerically and experimentally in a comparative manner, using simulation with fixed tissue properties to calculate fundamental measurements from an isothermal contour line at the completion of ablation [109].

During microwave ablation, the electromagnetic (EM) waves emitted by the probe can reflect at the interface between the catheter and the tissue due to impedance mismatches. As these waves reflect, they can travel back along the probe, inducing backward currents on the outer conductor of the coaxial cable. These reflected waves can propagate within the catheter, which surrounds the coaxial cable. The catheter may partially confine and guide these reflected waves back toward the tissue along the length of the probe, or the other direction towards the tip of the probe, affecting the distribution of the electromagnetic field.

The elongation of the SAR pattern along the probe is a result of these EM reflections. As the reflected waves travel along the outer surface of the probe, confined by the catheter, they can reintroduce energy into the tissue at points along the probe, not just at the point local to the active part of the antenna i.e. the slot.

Quantifying the shapes and sizes of the ablation fields extends only as far as the measurement of the length and diameter of the temperature field, from which the aspect ratio is written. However, this provides limited information for fields displaying bulges or folds. Considering that a sphere is the most desirable shape of ablation, it makes sense to use a metric quantifying how circular a two-dimensional shape is, i.e. the circularity.

The temperature dependence of the tissue dielectric properties has been shown to have a substantial influence on the simulation outcome, as changes in these properties are responsible for changing field patterns and probe performance throughout heating [46, 14, 88]. Therefore, it makes sense to consider not only the size and shape of the electric field pattern at the beginning of ablation but also the dynamics of how these patterns change throughout the process as the target tissue heats up.

This chapter presents a comparative analysis of transient changes to both the shape and size of temperature and SAR fields throughout ablations simulation, examined for a variety of common probe concepts. Shape analysis metrics specific to the objective of treating a spherical tumour will be used. To achieve this, a multi-physics modelling framework on an open-source platform, wrapped within a user interface is utilized, to allow an easy investigation of the dynamic fields created from the different probe geometries and input settings. In this chapter, we will now cover the shape analysis techniques used, describe the different probe concepts that have evolved, and then present the results of our analysis in a breakdown of each variable measured along with a discussion of the output from this work.

5.2 Design Variables

The design variables within microwave ablation that are relevant to this investigation include the probe concept and dimensions of the geometric variables for each of these concepts. Simulation of these probes allows measurables such as the reflection coefficient, shape and size, and SAR and temperature field to be made, which can be used to infer a design's effectiveness. We will take a look at how each of these variables are calculated now.

5.2.1 Reflection coefficient

If $*$ indicates the complex conjugate of a variable, the reflection coefficient of a probe has been shown as a function of the overall computed electric field $\mathbf{E}$, and the incident electric field $\mathbf{E}_{inc}$, at the input surface to the probe [146, 154]

$$\mathrm{S}_{11} = \frac{\int_{\partial\Omega_1} (\mathbf{E} - \mathbf{E}_{\mathrm{inc}}) \cdot \mathbf{E}^*_{\mathrm{inc}} \, \mathrm{d}(\partial\Omega_1)}{\int_{\partial\Omega_1} \mathbf{E}_{\mathrm{inc}} \cdot \mathbf{E}^*_{\mathrm{inc}} \, \mathrm{d}(\partial\Omega_1)}, \tag{5.1}$$

which is a measure of how well-matched the impedance of the tissue is to the characteristic impedance of the probe itself. A closely matched impedance will translate to a larger proportion of the energy supplied to the probe being transferred into the tissue, and therefore more energy absorption. In addition to negating issues associated with high-power reflection.

A coaxial MWA probe can be considered as a one-port system, where the S11-parameter is equal to the reflection coefficient Γ. Calculation is possible in terms of the total electric field, $\mathbf{E}|_{\partial\Omega_1}$, and exciting electric field input, $\mathbf{E}_{inc}|_{\partial\Omega_1}$, measured on the antenna input surface $\partial\Omega_1$ [97]. The boundary names can be seen by recapping the geometry used for modelling, in Fig 5.1.

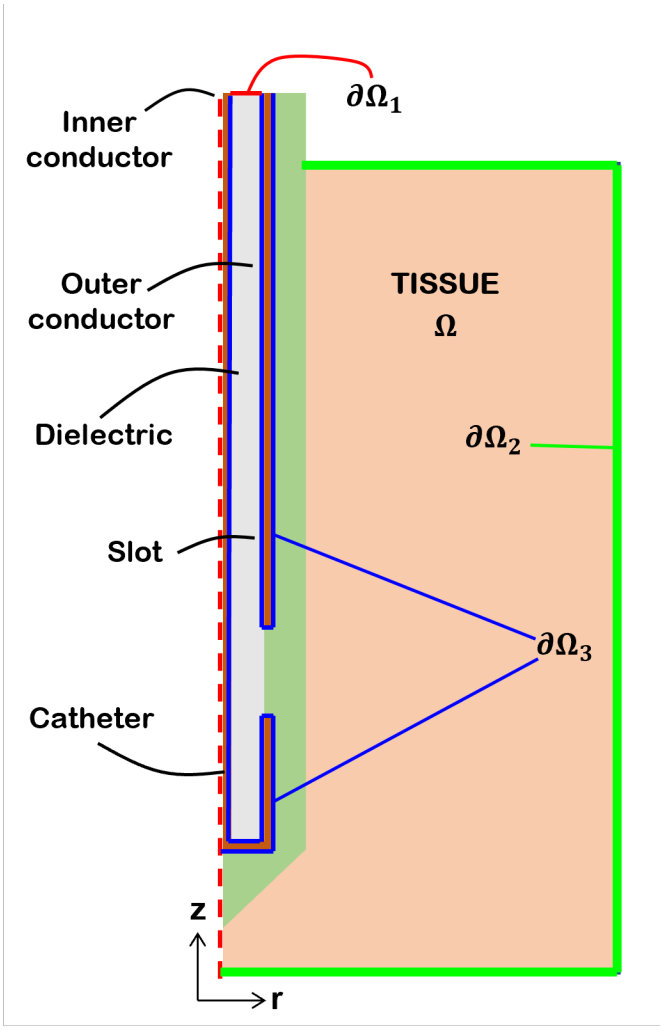

Figure 5.1: The axisymmetric domain modelled in this work with annotated boundaries.

5.2.2 Shape analysis

Assuming the ablation shape in this analysis is desired to be as spherical as possible in order to treat a spherical tumour. Temperature and energy absorption field shapes are formed from the simulated data and subsequently analysed, calculating a shape metric in 2D that is equivalent to measuring sphericity in 3D.

When analysing the shape and size of these distributions, it is helpful to define an enclosed boundary. This boundary is identified by setting an isocontour value for each specific field variable, an example of such an isocontour and the resulting 2D shape segmentation is shown in Fig 5.2. Once these boundaries are defined in the

axisymmetric data, the shape can be segmented for analysis.

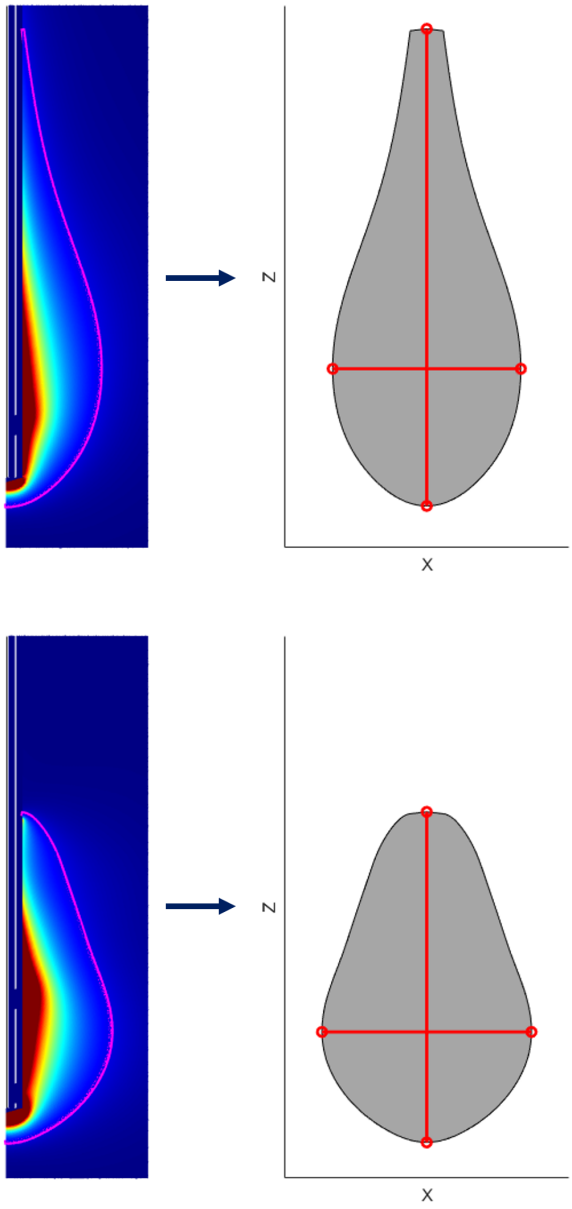

Figure 5.2: SAR within the tissue is calculated through equation 2.1, the SAR distribution data can be segmented by applying an isocontour threshold (left) which can be interpolated at its upper limit and mirrored to create a complete 2D shape (right). From this 2D segmentation, the shape analysis metrics such as aspect ratio and circularity are taken.

The two-dimensional area of each shape can be calculated for exact measure of size. The first shape metric uses takes the maximum length and width of each shape to define the aspect ratio as

$$AspectRatio = \frac{Max\ Width}{Max\ Length}. \tag{5.2}$$

This is a commonly used shape descriptor used to evaluate ablations in both the computational and experimental fields [80][109][48]. Another descriptor of shape, circularity, can be described by a function of area and perimeter

$$\text{Circularity} = \frac{4\pi\ \text{Area}}{\text{Perimeter}^2}, \tag{5.3}$$

this yields a value that is constant regardless of the scale of shape, and with values varying relative to 1 which would represent a perfect circle. Figure 5.3 demonstrates how the SAR field pattern deforms from its original shape when heated.

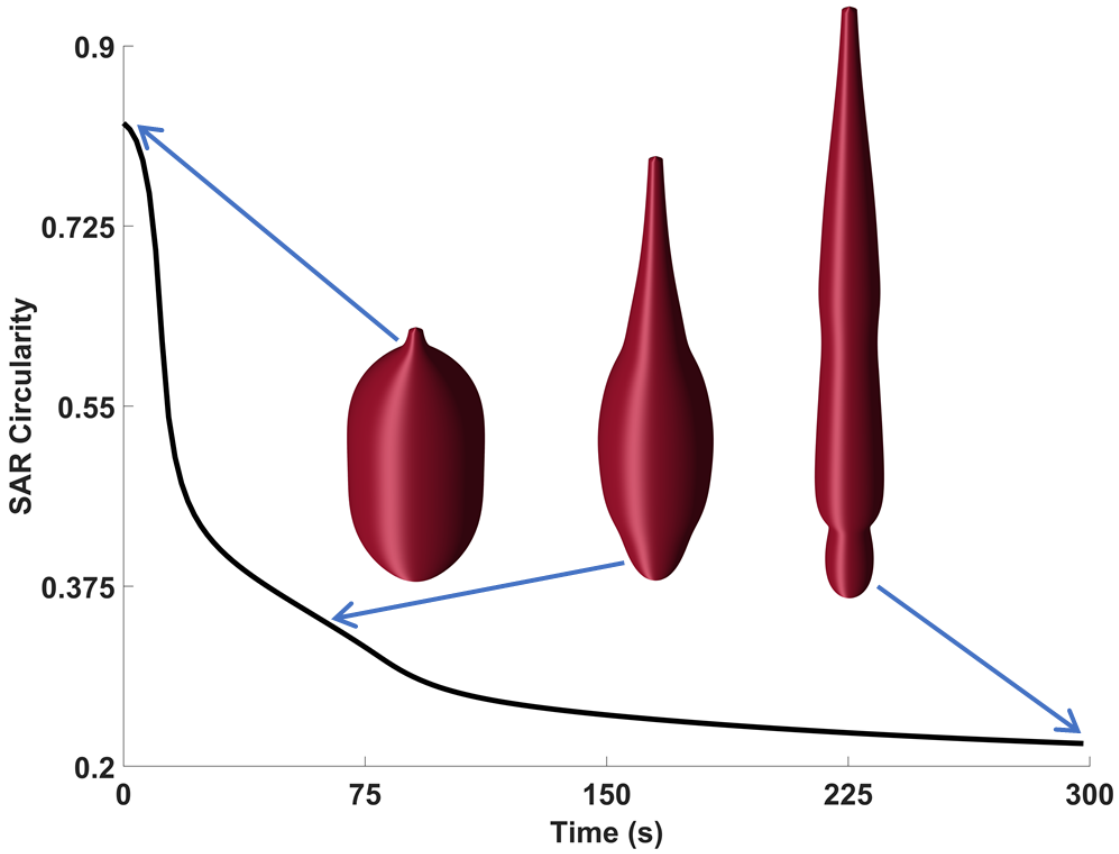

Figure 5.3: Absorption patterns segmented by the 1kW/m^3 isocontour throughout the ablation simulation, annotated against the absorption circularity curve.

As ablation progresses, the SAR pattern elongates significantly along the probe. This elongation is primarily driven by the gradual heating of tissue and the associated changes in its dielectric properties. While the initial setup might achieve optimal impedance matching, allowing for efficient energy absorption, the situation evolves as the tissue's permittivity and conductivity decrease due to heating.

This decrease in permittivity and conductivity leads to a reduction in the tissue's impedance. Initially, the tissue and probe are well-matched impedance-wise, allowing for effective energy absorption. But as the tissue heats and its impedance decreases, this match deteriorates. The impedance mismatch increases the reflection coefficient, causing more microwave energy to be reflected at the catheter-tissue interface, rather than being absorbed by the tissue.

These reflected waves do not remain static but travel along the length of the probe. They propagate towards regions of the tissue that are cooler and thus have not yet undergone significant changes in dielectric properties. In these cooler regions, the tissue's impedance is still closer to its original state, which reduces the extent of impedance mismatch in these areas. As a result, the reflected energy can travel further along the probe to these cooler areas before it is eventually absorbed or reflected back again. This movement of energy contributes to the progressive elongation of the SAR pattern.

As the ablation continues and more of the tissue along the probe heats up, the zones of reduced impedance mismatch move progressively further away from the initial ablation site. This shift causes the SAR pattern to elongate gradually. The elongation continues as long as there are cooler regions along the probe that can absorb the reflected energy more effectively than the heated regions. Therefore, the elongation of the SAR pattern is a dynamic process, continually evolving as the temperature along different sections of the probe changes.

5.2.3 Probe concepts

Several variations for the design of MWA probes have been proposed and studied. Four main concepts could be distinguished that will be simulated and compared in this work, all of which are axisymmetric, and are illustrated in figure 5.4. These include the monopole (M) probe structure Fig 5.4.a, which maintains the main coaxial body but with a section of the outer conductor removed towards the end. The single slotted (SS) probe Fig 5.4.b described prior in the methods section, a dual slotted (DS) probe Fig 5.4.c with two gaps in the outer conductor separated by a fixed length and a sleeve single slotted (SSS) probe Fig 5.4.d, containing the same coaxial geometry of the single slot but with an additional layer of conducting material within the catheter. For the purpose of this study, we will be operating at a frequency of 2.45 GHz.

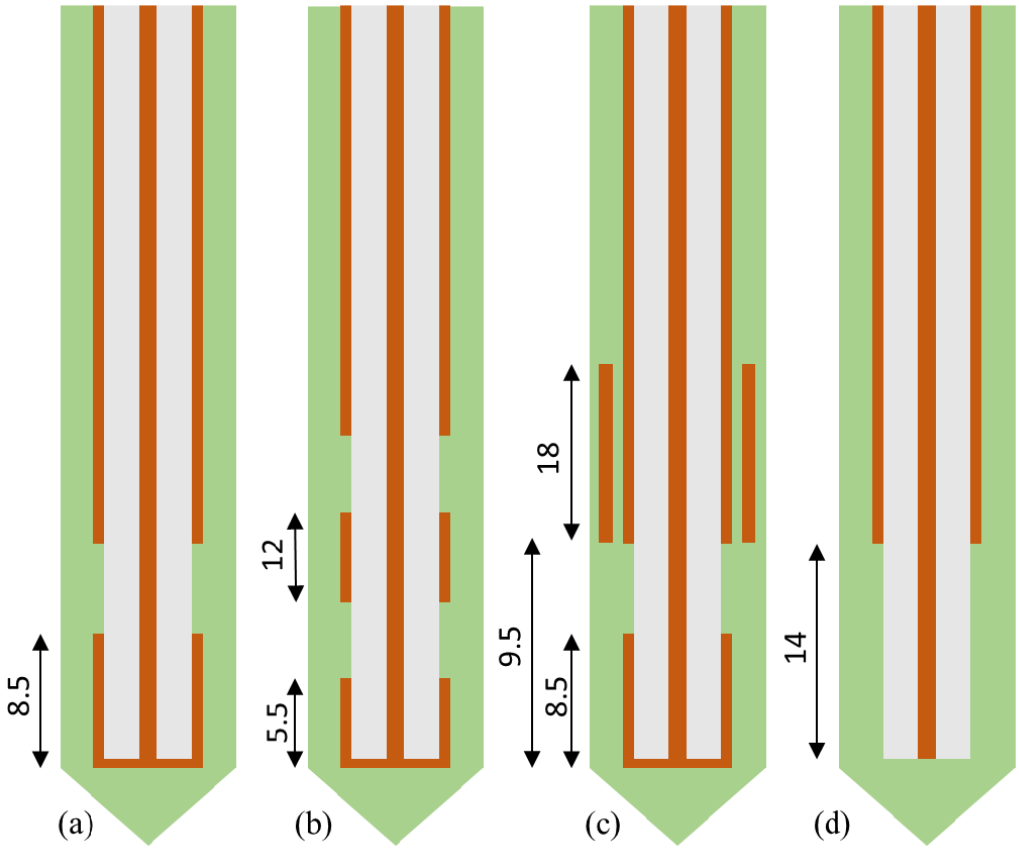

Figure 5.4: Illustrations of geometry for each of the probe concepts with specific geometry (mm). (a) single slot (SS), (b) Dual slot (DS), (c) Sleeve Single slot (SSS) and (d) Monopole (M).

The DS probe effectively has two sources that radiate out from the antenna, one from each slot, these two waves interact destructively around the upper region of the upper slot to reduce elongation of the electric field pattern along the outside of the outer conductor [1]. Reducing this elongation aims to create more concentrated absorption patterns that are closer to the spherical ideal [80]. An SSS probe aims to achieve the same outcome by introducing a sheath of conducting material within the catheter that surrounds the coaxial structure, but maintaining separation from the outer coaxial layer itself, with the objective of reducing the level of backward heating [106]. These designs have been shown to confine the absorption pattern towards the probe tip.

The exposed inner conductor length for the M probe, and the sleeve length used in SSS were chosen to replicate that used in the comparative study, where the exposed inner conductor length is close to $(\lambda/4)$ for resonance [109]. The same slot positioning was adopted for the SS and SSS probes such that a direct comparison can be made between the two. The theory behind the introduction of the sleeve to the SS design to create the SSS design is that the sleeve can act to interrupt reflected waves which would otherwise travel uninterrupted along the outside of the antenna through the catheter. This sleeve therefore acts to contain the EM energy at a local point close to the slot. Additionally, The optimized design of the floating sleeve antenna, specifically its length being approximately half the effective wavelength, plays a crucial role in enhancing the confinement of electromagnetic energy to the intended ablation zone. This length is strategically chosen to leverage the natural properties of wave propagation, ensuring that the sleeve effectively blocks backward wave propagation and instead enhances forward transmission[155].

For consistency, common dimensions are used for the coaxial and catheter parts of all probes simulated. The outer radii of coaxial components, in mm, are as follows: inner conductor (0.135), dielectric (0.335), outer conductor (0.46), and catheter (0.895). All slotted probes use a slot width of 1mm and the sleeve component has a thickness of 0.15mm. Probe-specific dimensions are described in Fig 5.4. The length of each probe is simulated as 70mm in a tissue domain of 80mm high and a radius of 40mm. The full

set of material properties is summarised in table 5.1.

Property	**Liver**	**Copper**	**Teflon**
Relative permittivity	$\varepsilon(T)$ or 43	–	2.1
Electrical conductivity [S/m]	$\sigma(T)$ or 1.69	–	0
Thermal conductivity [W/m°C]	0.5	400	0.24
Mass density [kg/m^3]	1060	8700	1200
Specific heat capacity [J/kg°C]	3600	385	1050

Table 5.1: A summary of the relevant variables in the setup of the comparative simulation.

5.3 Results

As mentioned previously, the open-source NGSolve library was chosen as a foundation to solve this coupled system by hp finite elements [148]. Geometries of each probe and surrounding tissue domain are created and meshed in the GMSH software package. An unstructured mesh of triangular elements is created with refinements near the slot in the antenna where higher gradients within the electric field are observed. The electromagnetic equations are solved across the discretised domain by third-order H(Curl) elements and second-order Lagrange elements were used for discretising the bioheat equation on the same mesh using NGSolve [150]. A weak coupling exists whereby material properties sensitive to temperature are updated at the end of each time step before resolving the electromagnetic problem again.

Simulations use a microwave frequency of 2.45 GHz and with an input power of 30W, whilst each ablation simulates 300s. The reflection coefficient, SAR, and temperature distribution are all calculated throughout and subsequently used for further shape analysis. Repeat simulations are made using constant tissue properties and plotted alongside to emphasise the difference this can make. The speed and usability of our open-source framework were greatly improved by the creation of an intuitive, bespoke user interface whereby simulation inputs could be selected in a simple fashion. An example of the first page of this used interface is shown in Fig 5.5

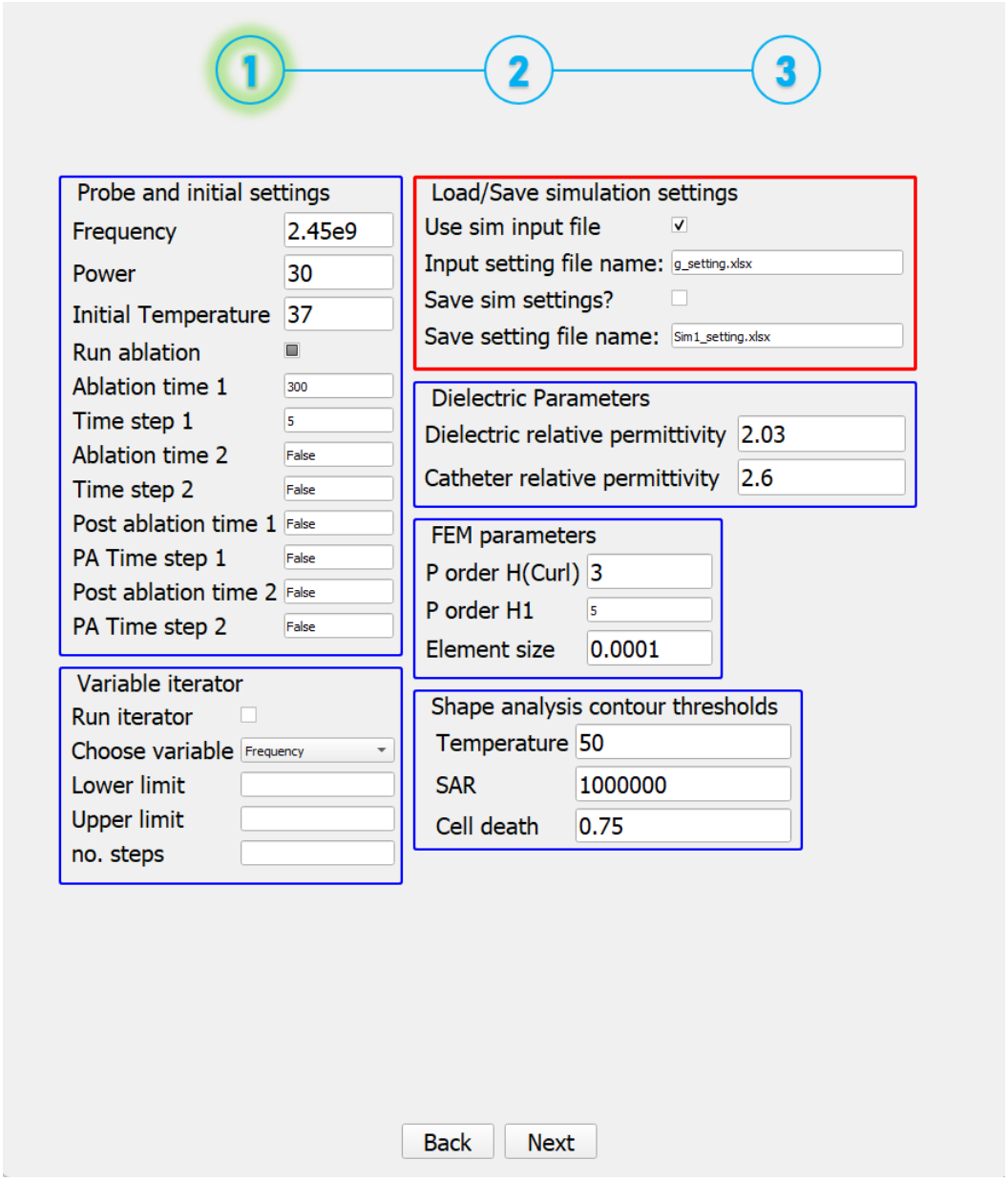

Figure 5.5: Graphical user interface used when running the simulations, this first page allows input of basic settings.

Once basic simulation settings have been prescribed, the second page of the GUI allows the user to select a probe from the library of existing designs. A design drawing of the chosen probe will appear within the window, annotated with all the geometric elements as shown in Fig 5.6. It is possible to edit these probe dimensions through the list on the left, and then an ablation simulation can be carried out to the description of the user.

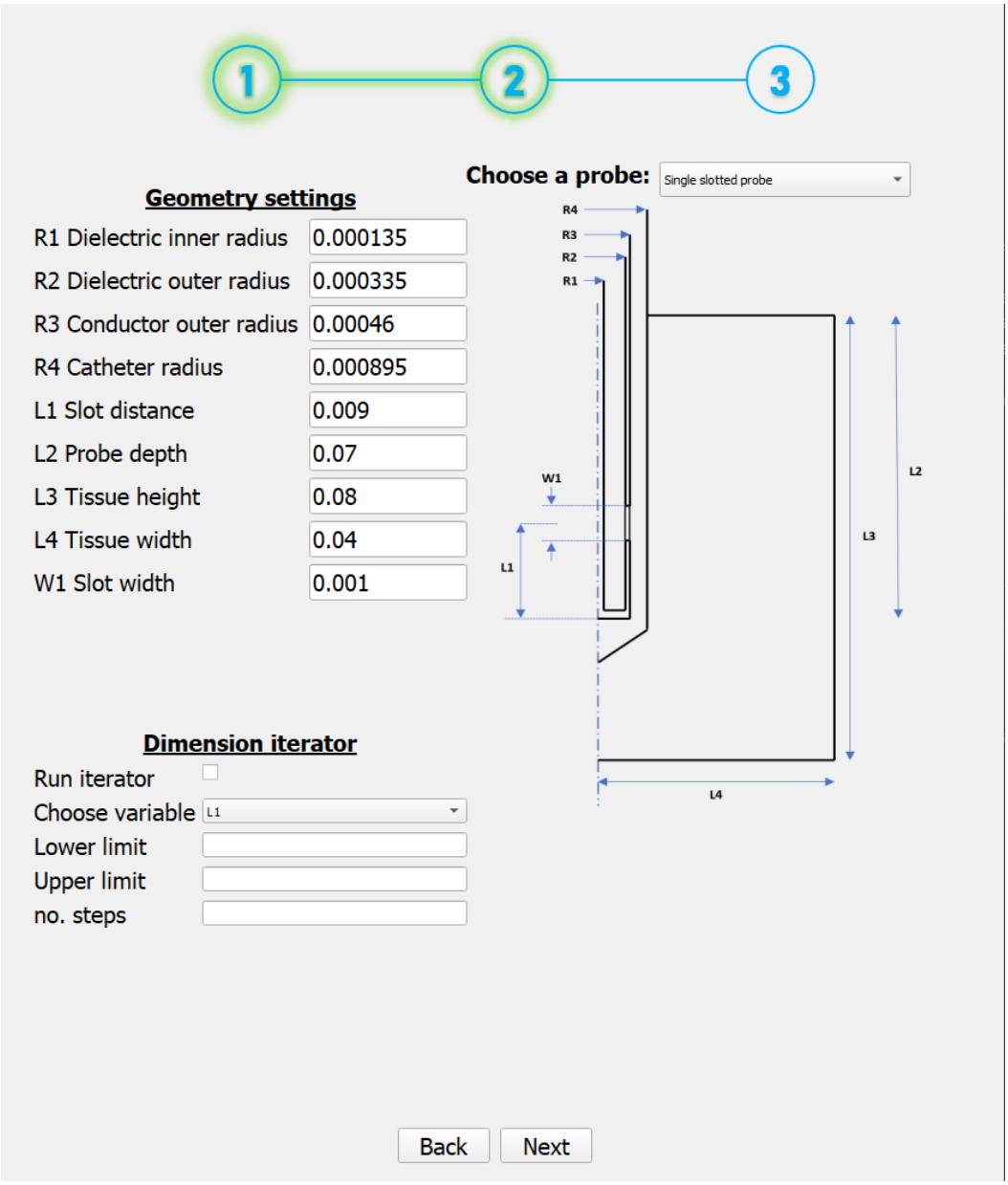

Figure 5.6: The second page of the GUI allows probe type to be selected from a library, and the exact dimensions defined.

5.3.1 Reflection Coefficient

Figure 5.7 shows the temporal changes in the reflection coefficient of each probe design through ablation. Initially, with the dielectric properties of liver tissue at 37°C, the calculated reflection coefficients from least to most efficient are DS -8.5 dB, M -15 dB, SS -27 dB closely followed by SSS -47 dB.

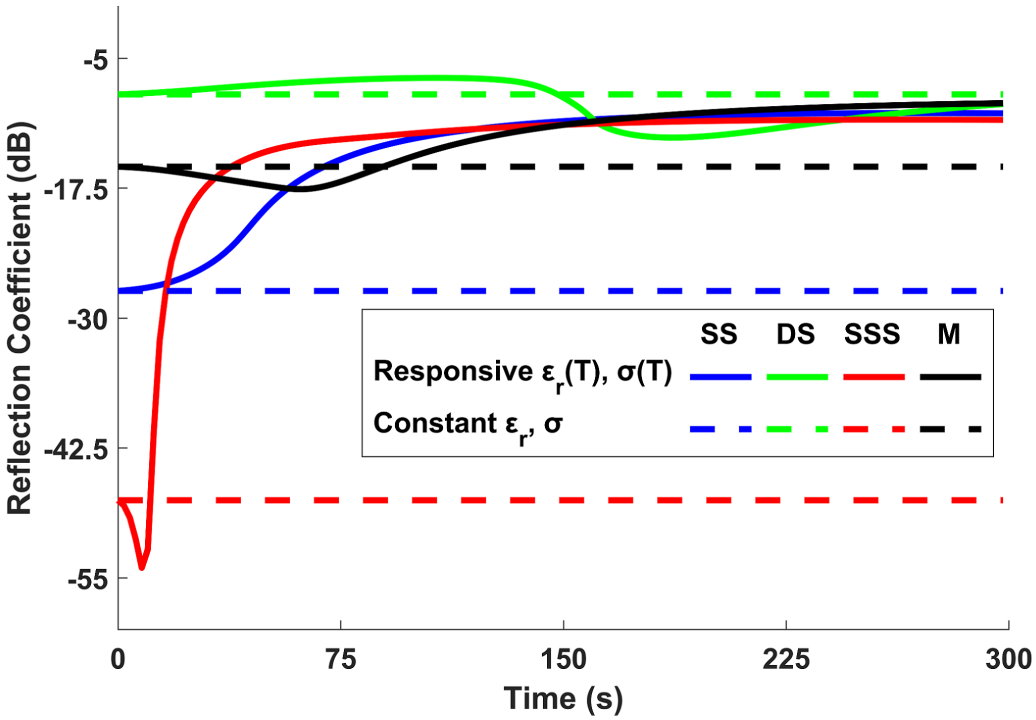

Figure 5.7: Graphic highlighting the significant changes in the reflection coefficient throughout ablation across the variety of probe designs, demonstrating the need to capture the dynamic changes in coefficients as opposed to treating them as constant.

The impedance of a coaxial probe when terminated with tissue is dependent on both the probe design and the electrical properties of the tissue. Initially aligning close to the typical impedance of biological tissues (about 50 ohms), this impedance varies as tissue properties change with increased heating, affecting permittivity and conductivity.

At the onset of ablation, the SSS probe displayed the best impedance match to the pre-heated tissue properties, as indicated by its lowest initial reflection coefficient. This setup suggested superior energy transfer capabilities compared to the SS, M, and DS designs, with the DS probe showing the least optimal initial matching. As the

heating induced changes in tissue properties, all probe types showed fluctuations in reflection coefficients, highlighting the evolving nature of tissue impedance.

The SSS probe's reflection coefficients initially improved sharply, reaching a minimum of -54 dB within the first ten seconds. However, as the temperature continued to rise, the decrease in permittivity and conductivity led to a steep deterioration in impedance match. This highlights the sensitivity of impedance matching to rapid changes in tissue properties during the early stages of ablation.

In contrast, the DS probe demonstrated more stable impedance characteristics over time, with a slight dip in reflection coefficient around 150 seconds suggesting a temporary optimal match. The M probe showed a gradual decrease in reflection coefficient to -18 dB around 62 seconds, followed by a slow rise, indicating moderate adaptability to changing tissue properties.

These trends underscore that the most substantial changes in impedance and reflection coefficients typically occur early in the ablation process, predominantly influenced by the tissue nearest to the probe where SAR and temperature rise are highest. As ablation progresses, these property changes near the probe stabilize, leading to a plateau in reflection coefficients.

As temperature approaches 100 degrees Celsius, tissue dielectric properties decrease at an accelerated rate due to rapid loss in water content, significantly impacting impedance. Initially, in the case of the SSS, this results in improved impedance matching, reflected by decreasing reflection coefficients. However, as temperatures near 100 degrees, the rapid change in dielectric properties causes a swift shift away from optimal impedance matching, explaining the observed non-monotonic behavior in reflection coefficients.

Given these insights, future probe designs could benefit from incorporating dynamically adaptive materials or configurations to better accommodate changing tissue impedance. Utilizing temperature-sensitive materials that adjust electrical characteristics in re-

sponse to tissue heating could enhance energy transfer efficiency.

These findings from simulated studies highlight the critical role of probe design and initial impedance matching in microwave ablation effectiveness. As the field evolves, innovative probe designs will be essential for adapting to the dynamic nature of tissue properties during ablation. These characteristics have been reported in other publications, such as those presented in [88], where for a sleeve antenna, measured S11 peaks at around -33 dB before reducing rapidly towards a plateau of less than -5 dB.

5.3.2 Shape Analysis

The size of the threshold SAR field created for each probe design is captured in Fig 5.8, which displays the data for the total area above a SAR threshold of 1kW/m^3. At the first instance of power being supplied to the probes, the segmented areas in increasing order are 3.70 $\times 10^{-4}$m^2 for DS, 4.47 $\times 10^{-4}$m^2 SSS, 4.99 $\times 10^{-4}$m^2 for M and 5.49$\times 10^{-4}$m^2 for SS. Whilst the presented results in isolation already contain useful information, it is the collective that provides a more complete picture of the diverse transient changes observed between probes. A common theme shared by all probes is an increase in SAR area measured at or shortly proceeding the reduced reflection coefficient seen in Fig 5.7, and reduced area seen when the reflection coefficient increases. This is most clearly illustrated for the DS probe with an obvious increase around 150s.

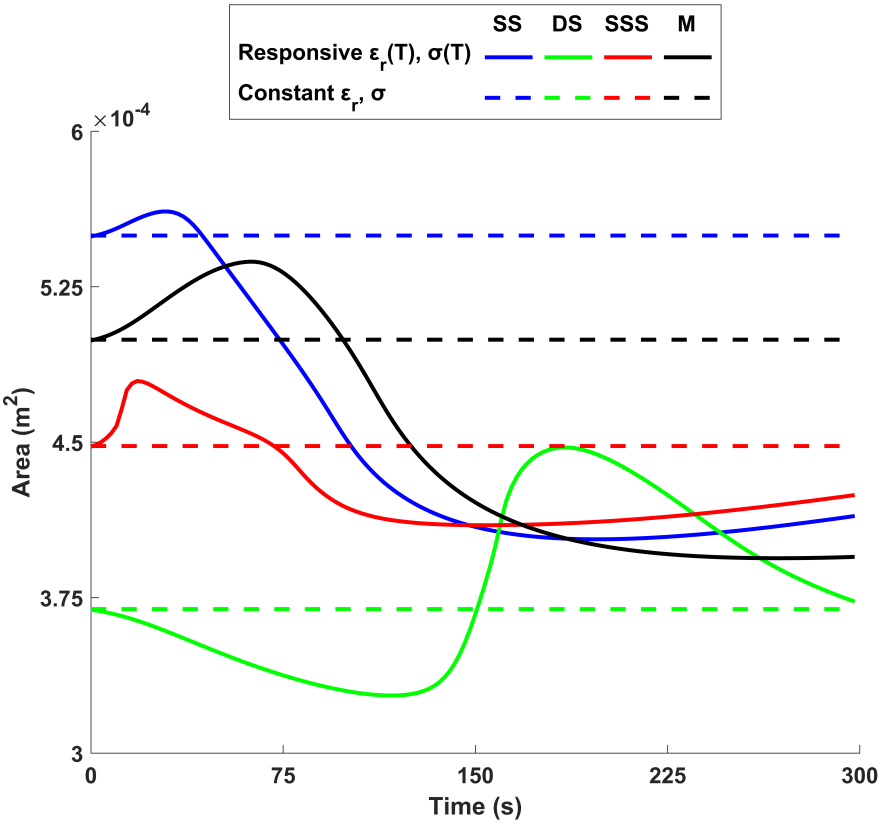

Figure 5.8: Results presented for SAR area, The influence of temperature-sensitive dielectric tissue properties is apparent when compared with simulated results using constant dielectric values.

The shape analysis of the SAR pattern is presented using the circularity and aspect ratio metrics, as shown in Fig 5.9 and 5.10 respectively. Initially, the SSS design has the highest circularity of 0.81, with the three other concepts closely matched in the range 0.35 - 0.38. All probes display a trend of reducing circularity throughout ablation, although with different gradients, the higher circularity from SSS probe reduces at a greater rate. Final measures across all probes span a small range between 0.20 - 0.22.

Inspecting the SAR aspect ratio, it is clear that a very similar outcome to the circularity is presented. The SSS design again has the highest aspect ratio to begin with, at a value of 0.49, significantly higher than the closely clustered values for the other three probes which lie in the region of 0.23 - 0.28. The reducing trend seen in the circularity is present in the aspect ratio too, the gradient changes appear to be very similar on

both graphs.

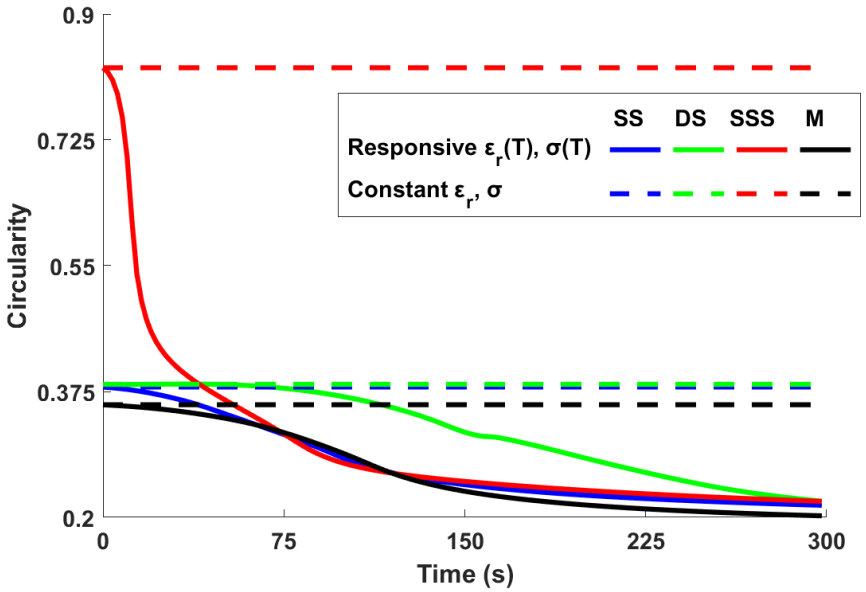

Figure 5.9: SAR circularity throughout simulated ablation with temperature-dependant dielectric properties, and constant dielectric properties.

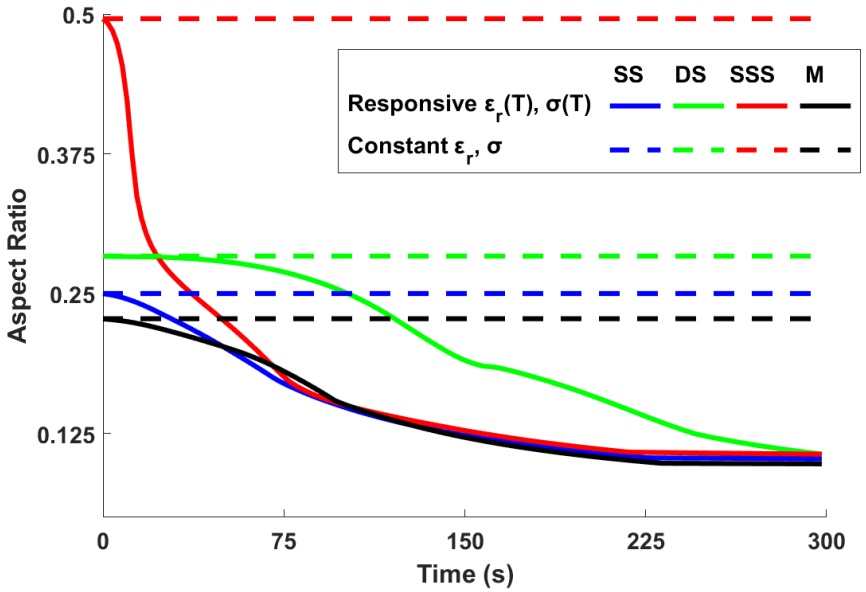

Figure 5.10: SAR aspect ratio throughout simulated ablation with temperature-dependant dielectric properties, and constant dielectric properties.

The same analysis is performed on the temperature field. Unlike their SAR counterparts, the 50°C thresholded thermal areas show a simple increase throughout the ablation process, which is observed consistently for all probes as illustrated in Fig 7.4. This temperature is sufficient to coagulate tissue in less than 5 minutes exposure time [147]. Initial calculated values show the DS probe has the smallest area early on with 1.9×10^{-4}m^2, followed by M at 2.8×10^{-4}m^2 with SS and SSS around 3.3×10^{-4}m^2. The M, SS, and SSS follow similar values throughout and end closely in the range 16.1 - 16.4×10^{-4}m^2, with the DS probe following the same trend but at a lower value throughout, finishing at 14.3×10^{-4}m^2.

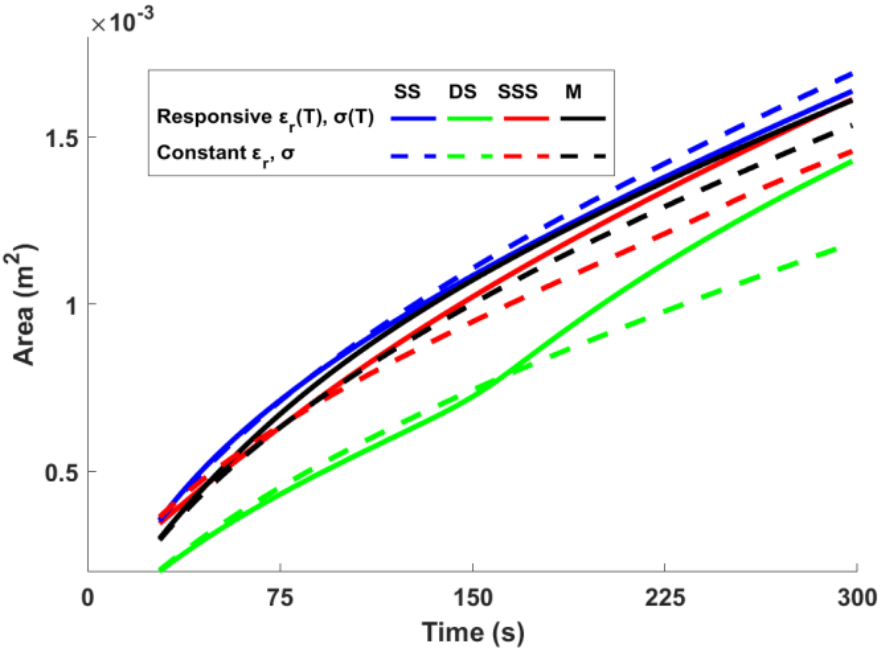

Figure 5.11: Temperature area segmented by the 50°C isotherm, showing the differences between temperature variable and constant dielectric properties via the solid and dotted lines respectively.

The temperature shape analysis is shown in figures 5.12 and 5.13. Investigating the circularity results in Fig 5.12, the SS and M probes show curves of an asymptotic nature with their starting values of 0.58 and end values of 0.73. The SSS and DS probes show different characteristics with increasing circularity values for a period before reaching a maximum and reducing for the remainder of the ablation. Potentially as a result of the markedly different circularity of SAR patterns when compared to the SS and M probes, as evident in Fig 5.9.

Comparing the circularity with the aspect ratio results shown in Fig 5.13, they appear to show similar trends for the SS and M probes. However, the curves of the SSS and DS probes are slightly different, with the DS displaying more of an increasing trend up to the midway point of ablation. The SSS probe results show fewer features than the equivalent for circularity, the aspect ratio shows little change throughout the simulation, and a less pronounced peak at the beginning of ablation.

Focussing on the dashed lines, corresponding to simulations with constant dielectric properties, the changes in aspect ratio and circularity at around 240 seconds are due to the isotherm reaching the boundary of the tissue domain. This will inherently influence the segmented shape as it connects a straight edge between the points where the isotherm meets the boundary.

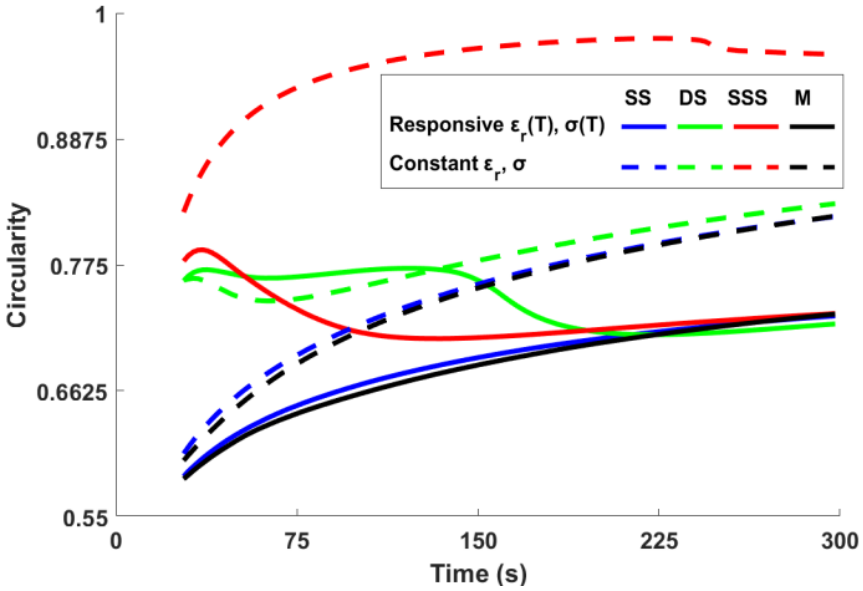

Figure 5.12: Temperature circularity calculated using Eq (5.3).

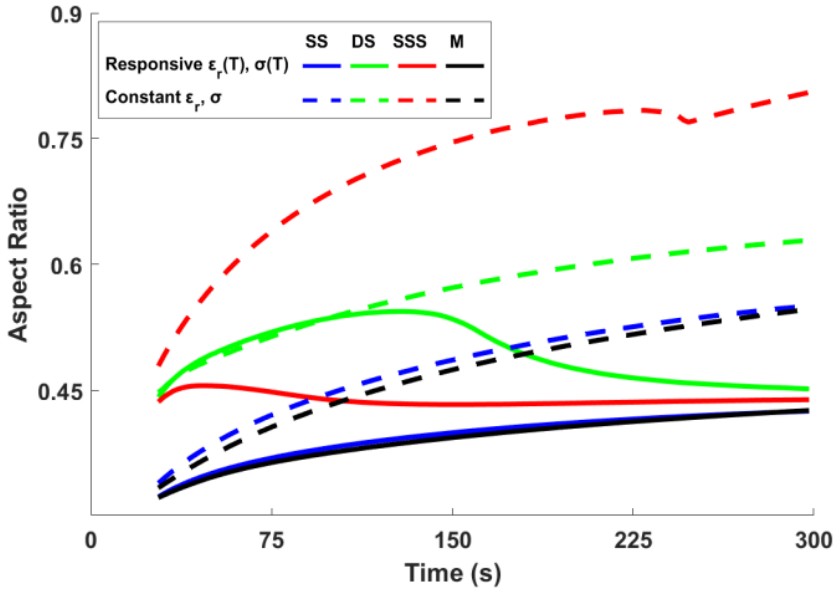

Figure 5.13: Temperature aspect ratio calculated from the segmented 50°C isotherm shapes.

5.4 Discussion

The experimental data presented in [109] utilized four probes with design specifications similar to those modelled in this study. These probes, operated at 40 watts power input, can be comparable to our simulated results at 30 watts when accounting for the losses within the generator and connecting lines to the MWA probe, produced varying ablation diameters: 0.48 for the SS probe, 0.51 for the M, 0.61 for the dual slotted, and 0.78 for the SSS. These measurements provide a benchmark for comparing the aspect ratios derived from our 50°C isotherm-based simulation.

Our simulation closely matches the aspect ratio for the SS design but displays more variation for the other designs. Several factors could explain these discrepancies:

Design Sensitivity: Even slight variations in probe design between our simulation and the experimental study can significantly influence outcomes. Our results indicate that the reflection coefficient and SAR are highly sensitive to these design differences.

Temperature-Dependent Measurement: The experimental ablation sizes were measured based on visual markings correlated with a critical temperature threshold, typically around 60°C, indicative of significant thermal damage. In contrast, our simulations use the 50°C isotherm to predict ablation size. This difference in thermal benchmarks could contribute to the observed discrepancies, as visual markings might not precisely capture the entire zone experiencing cellular damage.

Given these considerations, the variations between our simulated data and the experimental results underscore the complexity of accurately modelling microwave ablation. These findings highlight the need for refining simulation parameters and incorporating more sophisticated models of tissue behaviour and thermal response.

The reflection coefficients for all antenna designs showed a range of efficiencies throughout ablation. Hence, although it was found that the addition of a sleeve to the SS design (denoted as SSS) reduces wave reflections at the start of ablation consistent

with literature [79, 109], the transient responses of the tissue significantly change this behaviour. Three of the designs display an increasing reflection coefficient compared to their starting value. This reinforces the need to take account of the tissue property changes during the probe design cycle to accurately predict undesirable heating along the probe caused by reflected power. Results here suggest the magnitude of these changing reflections is markedly different between the designs, and although the SSS at times has the lowest levels of reflection, it is also the most variable throughout ablation, suggesting a higher sensitivity to changes in the tissue dielectric properties incurred as heating progresses.

The importance of transient tissue responses is further highlighted in the temperature analysis where the shape (circularity) of the ablation areas vary greatly, whilst the overall heated areas grow similarly for each probe. For example, when the material properties are taken constant, the SSS design appears to create much more circular absorption patterns outperforming the other probes as it more closely matches the typically spherical shape of tumours. However, this effect disappears the moment variable tissue properties are introduced, which makes all probes perform equally (in terms of shape) at the end of ablation. These results could question the use of a sleeve in a probe design, although further analysis and probe optimisation are required to provide a conclusive answer. The overall trend observed between the probes is that there are some profound performance differences between them in the early stages of ablation that seem to disappear towards the end of ablation.

Even though the results as presented are useful a few limitations can still be identified. The transient behaviour in these simulations is strongly dependent on the coupling between the electromagnetic and thermal problems, i.e. the material models used. More detailed and robust material models are required to get quantitative predictive ablation models. This includes the physiological changes that occur during tissue ablation, such as perfusion (in vivo) or tissue shrinkage when exposed to temperature increase.

Also, the geometries used in these simulations are chosen based on literature, but without consideration of manufacturability. This was done so that the probe diameter was consistent across all probes tested and for a more intuitive comparison. Optimisation approaches such as those presented in [88] are recommended to explore the potential of different probe types.

As this study has demonstrated, a thorough study of the dynamics is key to understanding tissue ablation. This might be emphasised even further if one considers the effects of transient thermal loading on cellular damage models.

6 Internally Cooled Probe Design

6.1 Background

As previously discussed, disadvantages to the MWA treatment also exist. One such problem is the elongated pattern of heating generated from the probes, which poses an issue when the shape of a target tumour is typically spherical. Such lengthened heating patterns increase the possibility of ablating healthy tissue away from the diseased area, therefore causing unwanted damage. Ideally, the heating pattern would match the shape of cancerous growth for optimal treatment. These elongated ablation zones are attributed to internal heating of the probe due to resistances within the coaxial region [156], in combination with electrical field patterns that extend up the probe shaft due to backward current flowing along the outer surface of the outer conductor [1], and conduction of heat along the insulating sheath material.

In chapter 5 we investigated some common design developments that have sought to mitigate these effects by yielding different SAR field patterns within the tissue they are embedded. The focus there was to compare different design concepts and explore the effect that temperature sensitive dielectric properties have throughout the ablation. Within this chapter we will investigate one particular means of absorbing the unwanted heat created from ablation that causes damage to healthy tissue, in addition to limiting the charring of tissue that can occur adjacent to the probe and increase the difficulty of removing the probe upon completion of the procedure [94]. Primarily this takes the form of fluid-cooled probe designs, a coolant fluid is circulated along the probe shaft to reduce the overheating effect. Studies have shown larger ablations are possible using this design philosophy owing to the use of higher input power being possible [119, 79]. The coolant fluid simulated here is water, which has a high specific heat capacity making for an ideal sink of thermal energy from the ablation zone extending along the antenna shaft. In addition, water acts as an effective absorber of microwaves, indicated by the characteristically high dielectric constant, introduction of cooling will thereby influence the SAR pattern created. The specific geometry of coolant structures could be used to manipulate absorption patterns and the resulting temperature field.

Shaft-cooled probes have been proven to assist ablation by aiding positioning within the patient, gas-cooled probes can freeze a small region of adjacent tissue and effectively fix the probe in place throughout the procedure, without affecting the extent of ablation achieved [116].

Experimental studies evaluating the performance of cooled probe types appear in the literature but are scarcely accompanied by computational simulation. Those existing works on cooled antennas have employed boundary conditions in their modelling to approximate the effects the coolant will have. This has been attempted through the implementation of fixed Dirichlet boundary conditions upon coolant surfaces [121], followed later by convective boundary conditions [122, 123, 124, 125, 140]. All of these assume that coolant temperature remains constant throughout the simulation, using approximate convection heat transfer coefficients. More recently an increasingly comprehensive modelling approach has appeared that included computational fluid dynamics (CFD) modelling within the probe [94].

While the use of CFD in modeling coolant dynamics within MWA probes has been established, the full potential of these models in systematically improving probe design has yet to be fully realized. The model we create here employs an in-depth fluid flow computation. Our approach achieves a velocity profile for the coolant through the probe's cooling structures, which, when combined with electro-thermal multiphysics modeling frameworks, allows for the resolution of a comprehensive advection-diffusion problem.

While recent research has begun to address the fluid dynamics within MWA probes, our work extends this by exploring the intricate effects of coolant structure design, coolant flow rate, and, notably, coolant temperature on ablation outcomes. This approach allows for an enhanced understanding of the thermal management within MWA probes, addressing not only the issue of backward heating but also the potential for optimizing probe designs to achieve more desirable heating patterns. The theoretical exploration

undertaken in this study lays a foundational groundwork for future experimental validation and practical applications, aiming to enhance the efficacy and safety of MWA therapies.

The chapter layout is as follows: Sub-section 6.2 lays out the relevant governing principles of electro-magnetics, fluid dynamics, and heat transfer required for a model of MWA with internal fluid cooling. This is followed by sub-section 6.3 an explanation of the fluid dynamics used in solving the multi-physics problem discussed. Sub-section 6.4 summarises the investigation results in each of the three areas of interest, position, flow-rate, and input temperature. Finally, Sub-section 6.5 presents a comparison to experimental data and a discussion around what can be drawn from this work.

6.2 Methodology

This section will set out the cooled probe design and overall system considered in the analysis, then a brief recap of the axisymmetric computational approach and necessary additions to incorporate coolant flow into the established multi-physics problem, finishing with an advection-diffusion equation that combines the two physical models to calculate an overall temperature distribution.

6.2.1 Probes

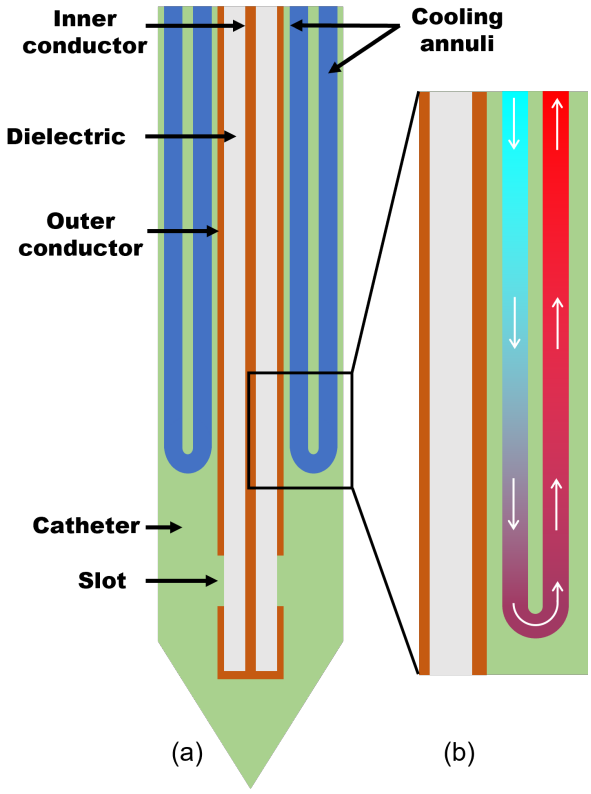

Figure 6.1: An illustration of the basic concept of internally cooled MWA probes (a) and heat exchange occurring through advection (b). In this configuration, coolant fluid enters through the inner annulus, creating a cross-flow heat exchanger

The study utilizes an axisymmetric 2D model of a cooled MWA probe, adopting a single slotted geometry as the basis for effectively applying microwave energy. Comprising mainly of a coaxial body, where concentric inner and outer conductive layers are separated by some type of dielectric material. Such coaxial structures permit electromagnetic waves to propagate transversely along the axis of the probe/feedline,

contained solely within the dielectric itself, shielded from any interfering waves that may exist outside of the cable and conversely, minimising leakage of signal to the surroundings. At the radiating end of the probe, a short gap in the outer conductor is created that spans its entire circumference, and it is through this gap that microwaves contained with the dielectric of the probe are able to propagate outwards. This entire coaxial portion of the probe described is then sealed within a catheter for insertion and hygiene purposes.

As an extension to the probe described, coolant flow is considered through annular ducts embedded in the catheter that encapsulates the main coaxial body of the probes. This approximated geometry uses two ducts that join at the distal end of the probe by a 180° bend, similar to designs seen in existing literature, such as those presented in [94], where a monopole-type antenna is used with a cooling system surrounding the coaxial structure. Fig 6.1 illustrates this concept and passage of fluid.

6.2.2 System and domain

The cooled probe is considered to be embedded within a tissue medium with properties of ex vivo bovine liver at an initial temperature of 20°C for ease of replication in future experimentation. Assuming a tissue in which the probe is inserted is homogeneous and isotropic, a reduction to a two-dimensional problem can be performed by utilizing the axisymmetric nature of the geometry. This simplification comes with the benefit of reduced computational burden. A complete summary of design variables defining the formation of the axisymmetric probe geometry is shown in Fig 6.2 and defined within Table 6.1. The dimensions chosen for the coaxial portion of this single slotted probe simulation are taken from existing computational works in the literature [105], and the additional geometry of the catheter and cooling structures diverge from current studies [122, 123, 124, 125, 140]. For this study, fixed radial dimensions of the cooling structures are used i.e. **T3** and **T2** in order to limit the number of variables and allow a constant catheter radius to be defined that encompasses all the cooling structures throughout our investigations.

The dielectric properties of water can vary depending on the ion content, in this analysis we assume that the water used is equivalent to that of drinking water, which has relatively low concentrations of dissolved minerals and ions. This is in contrast to distilled and deionized water which has an electrical conductivity several orders of magnitude smaller than that of drinking water.

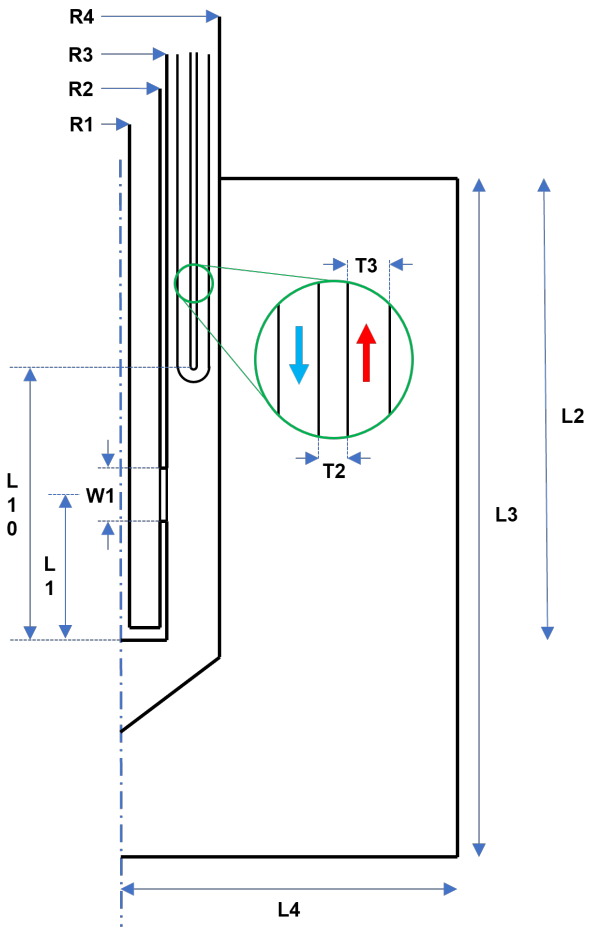

Figure 6.2: Annotated single slot cooled probe as seen in the user interface controlling simulations

During the first investigation, coolant position is the sole variable of interest, all geometric parameters apart from **L10** are kept constant during simulation. For the coolant settings investigations, a value for **L10** will be selected and a fixed geometry is defined upon which all further simulations of coolant flow rate and input temperature are ran.

Multiple materials exist within the computational domain being considered. The

Geometry description		
Dimension name	**Ref**	**Value [mm]**
Inner conductor outer radius	**R1**	0.135
Outer conductor inner radius	**R2**	0.335
Outer conductor outer radius	**R3**	0.460
Catheter outer radius	**R4**	1.500
Slot position	**L1**	3.000
insertion depth	**L2**	60.000
Tissue length	**L3**	80.000
Tissue width	**L4**	40.000
Coolant position	**L10**	-
Slot width	**W1**	1.000
Annulus separation	**T2**	0.200
Annulus thickness	**T3**	0.25

Table 6.1: Full list of geometric variables and their values used in the analysis. **L10** is the position of the apex of the coolant system relative to the end of the probe.

coaxial element itself contains copper for the conducting elements and a type of polytetrafluoroethylene (PTFE) for the dielectric, the space within the slot is an air gap that borders the catheter which is another type of PTFE, similar to the dielectric [135]. Water is the coolant fluid chosen for this analysis and models will assume that the biological tissue being ablated is bovine liver, as this carries with it a breadth of literature defining the properties relevant to this problem. The problem is multi physics, comprising both electromagnetic, fluid flow, and thermal parts. The relevant properties for solving each of these PDE problems are found in the literature. Table 6.2 gives an overview of the dielectric and thermal properties required.

Material property						
Material	$\sigma[S/m]$	$\varepsilon_r[-]$	$\mu_r[-]$	$k[W/m.K]$	$\rho[kg/m^3]$	$C_p[J/kg.K]$
Copper	-	-	-	386	8960	385
PTFE	0	2.03	1	0.25	2000	1000
Catheter	0	2.1	1	0.24	1200	1050
Water	0.05	78	1	0.6	1000	4200
Liver tissue	-	-	1	0.5	1060	3600
Air	-	-	1	1	1.2	1000

Table 6.2: Material properties for all components of the domain.

As we have shown in the preceding chapter, the temperature sensitivity of biological tissue properties can influence the outcome of ablation, but to reduce the number of variables at play within the highly multi physics problem we are proposing here, the temperature sensitivity of dielectrics is excluded for this initial analysis.

6.2.3 Basic Model - Computing Electromagnetic field

We make use of the existing methodology already covered in Chapter 3 of this thesis for modelling 2D axisymmetric probes. To recap, this can be summarised briefly.

To compute the entire electromagnetic field throughout the domain, an input wave is enforced across in boundary at the entrance to the coaxial portion of the probe. The magnitude and distribution of this input wave is proportional to the applied generator

power, which can be determined using Poyntings' theorem [157, 1]. This particular boundary condition must satisfy the requirement of exciting the system with an incident wave, whilst simultaneously absorbing any reflected microwaves. In practice this is achieved through the prescription of a waveguide port boundary condition (WPBC) [144, 145]. Truncation of the domain is necessary to form a finite domain and is attained through the appointment of absorbing boundary conditions to the tissue edges in addition to the upper bounds of the catheter and coolant annuli [145]. A simplification can be made to eliminate inner and outer conductor sub-domains from the electromagnetic problem by modelling their walls as perfect electrical conductors (PEC), as commonly practiced in MWA modelling [93, 135]. To complete the set of boundary conditions, axial symmetry is assigned to the rotational axis.

With this well defined problem, FEM is employed to compute a solution of the **E** field to then be used as a source in the later stages. A finite element solving package NGSolve [148] is utilized for solving the EM and other partial differential problems described later, our custom user interface will be used for prescribing the simulations we wish to run in this analysis, an example of how this works is shown in Fig 6.3.

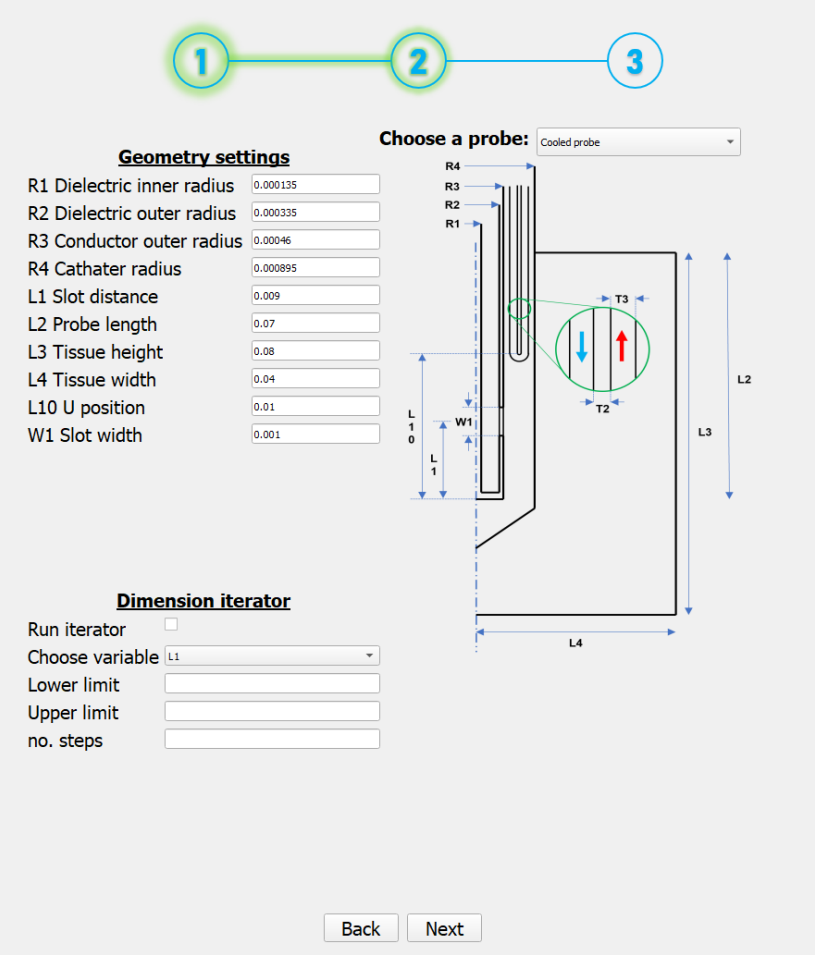

Figure 6.3: Our custom user interface was used to define the batch simulations we desired, along with experimental one-off simulations. This page of the GUI allows a cooled probe to be selected and specific dimensions defined.

6.3 Computing flow field

A full simulation of fluid flow within the coolant system can be carried out. Firstly, in order to compute the flow of coolant numerically, an input flow profile is required to drive the system, and then Navier Stokes equations can be formulated and computed for the flow velocity profile.

6.3.1 Input flow conditions

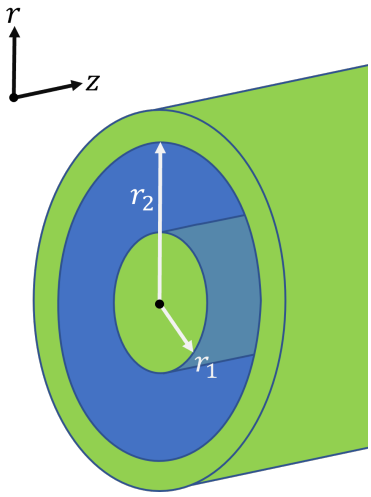

Figure 6.4: Geometry of an annulus where fluid flow is considered between the inner radius, r_1, and outer radius r_2.

	Value	Units
r_1	0.34875	mm
r_2	0.47375	mm
Q	120	$ml.min^{-1}$
	2×10^{-6}	$m^3.s^{-1}$
$\bar{u}$	6.19	$m.s^{-1}$
μ	1.7×10^{-3}	$kg.m^{-1}.s^{-1}$
ρ	1000	$kg.m^{-3}$

Table 6.3: Input flow parameters for calculation of Reynolds number and inlet flow profile.

Coolant fluid flow is typically supplied to the probe via a peristaltic pump, and circulates through two concentric annular sections within the catheter surrounding the main coaxial body, as indicated in Figures 6.1 and 6.2. In tubular geometries such as this, the Reynolds number can be defined by

$$Re = \frac{\bar{u}D_H}{\nu} = \frac{\rho\bar{u}D_H}{\mu} = \frac{WD_H}{\mu A}, \tag{6.1}$$

where D_H is the hydraulic diameter $[m]$, Q is the volumetric flowrate $[m^3.s^{-1}]$, A is the cross sectional area of the tube $[m^2]$, $\bar{u}$ is the mean velocity of fluid $[m.s^{-1}]$, μ is

the dynamic viscosity $[kg.m^{-1}.s^{-1}]$, ν is the kinematic viscosity $[m^2.s^{-1}]$ and W is the mass flowrate of the fluid $[kg.s^{-1}]$. The hydraulic diameter is defined as

$$D_H = \frac{4A}{P}, \tag{6.2}$$

where P is the wetted perimeter (total perimeter of all channel walls that are in contact with flow). For an annular duct, this can be simplified to $D_{H(Annulus)} = 2(r_2 - r_1)$ for the inside radius of the outer pipe, r_1, and outside diameter of the inner pipe, r_2. Geometric parameters used in this model for r_1 and r_2 are summarised in Table 6.3, along with a high flow rate of $120ml.min^{-1}$, since this is in alignment with the flowrate used in [94]. Given these parameters, a Reynolds number is computed as 910, indicating that flow rates even as high as this will be in the laminar regime [158].

Assuming that dimensions of the perfectly annular profile, and the volumetric flow rate is known, the magnitude of flow u that acts solely in the **z** direction can be analytically calculated as a function of radial position r, where $r_1 < r < r_2$. Fully developed flow within the annulus can be described as

$$u(r) = \Phi r^2 + c_1 \log|\mathrm{r}| + \mathrm{c}_2, \tag{6.3}$$

with $\Phi = \frac{1}{4\mu}\frac{\partial p}{\partial z}$. Assuming non-slip boundary conditions on the walls of the annulus, $u(r_1) = 0$ and $u(r_2) = 0$, constants c_1 and c_2 that can be defined, and in combination with Q, the flow profile can be solved as described fully in [158]. Equation (6.3) is used to enforce Dirichlet boundary conditions across the flow inlet, driving the fluid motion through the cooling system. The resulting flow is parabolic-like, with the peak velocity slightly closer to the inner radius. This skewing of the velocity profile towards the inner wall can be attributed to the smaller surface area at this radius, which enhances shear stress and results in a steeper initial velocity gradient. Consequently, the velocity increases more sharply near the inner radius compared to the outer, leading to the observed asymmetry in the flow profile.

6.3.2 Fluid flow governing equation

For our coolant system, considering the fluid (water) as incompressible and Newtonian, with constant density, allows us to directly employ the steady-state incompressible

Navier-Stokes equation to describe fluid behavior. This approach simplifies the analysis by focusing on the conditions most relevant to the cooling system's operation. The governing equation, omitting transient effects due to a steady-state assumption, is represented as:

$$\underbrace{\rho(\mathbf{u}\cdot\nabla)\mathbf{u}}_{Convection} = \underbrace{-\nabla p + \mu\nabla^2\mathbf{u}}_{Diffusion} + \underbrace{\mathbf{f}}_{Source}, \tag{6.4}$$

where $\mathbf{u}$ denotes the fluid velocity field, p the fluid pressure, μ the dynamic viscosity, and $\mathbf{f}$ any external force acting on the fluid. This equation concisely captures the fluid dynamics within the coolant tubes, assuming the flow reaches a steady state, an assertion supported by [158].

Fig 6.5 displays the complete set of domains and boundaries concerning the coolant flow calculation. The volume in which flow should be calculated, Ψ, is a subdomain of Ω, such that $\Psi \subset \Omega$ with boundaries

$$\partial\Psi = \Gamma_1 \cup \Gamma_2 \cup \Gamma_3. \tag{6.5}$$

These are the portions of boundary covering the flow inlet, Γ_1, pipe walls, Γ_2, and the flow outlet Γ_3. The fluid source is enforced through a boundary condition across Γ_1 that is set to the flow profile, as analytically calculated through (6.3). Conversely, a fluid sink is appropriately set on the Γ_3 boundary through a homogeneous Neumann boundary condition. Non-slip conditions apply to the pipe walls Γ_2.

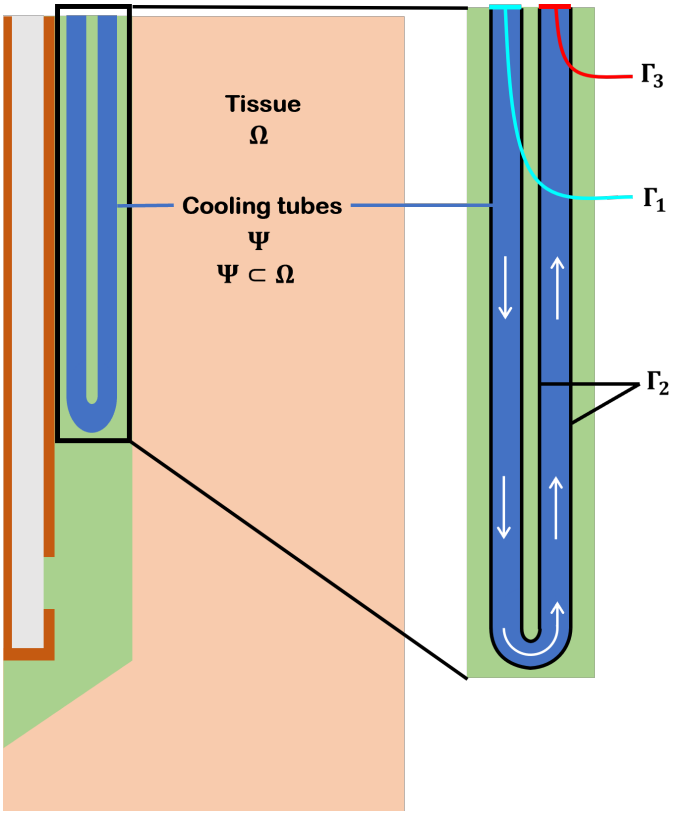

Figure 6.5: Complete domain and cooled sub-domain with accompanying boundary conditions

Therefore, the flow problem can be summarised as

$$\rho(\mathbf{u}\cdot\nabla)\mathbf{u} = -\nabla p + \mu\nabla^2\mathbf{u} + \mathbf{f} \qquad \text{in } \Psi, \tag{6.6}$$

$$\nabla\cdot\mathbf{u} = 0 \qquad \text{in } \Psi, \tag{6.7}$$

$$\mathbf{u} = \hat{\mathbf{z}}(Ar^2 + c_1\log|\mathrm{r}| + \mathrm{c}_2) \qquad \text{on } \Gamma_1, \tag{6.8}$$

$$\mathbf{u} = 0 \qquad \text{on } \Gamma_2, \tag{6.9}$$

$$\mu\frac{\partial\mathbf{u}}{\partial\hat{\mathbf{n}}} - p\hat{\mathbf{n}} = 0 \qquad \text{on } \Gamma_3, \tag{6.10}$$

Where $\hat{\mathbf{n}}$ is the surface normal vector. Using FEM, we solve this set of equations within the cooling system subdomain using a semi-implicit Euler method, which treats the convective term $\rho(\mathbf{u}\cdot\nabla)\mathbf{u}$ explicitly and the diffusive term $\mu\nabla^2\mathbf{u}$ implicitly. This approach offers a balance between numerical stability and computational efficiency.

The explicit treatment of the convective term means that it is evaluated using the velocity field from the previous time step, avoiding the need to solve a nonlinear system

of equations at each time step. Conversely, the implicit treatment of the diffusive term ensures numerical stability, allowing for larger time steps compared to a fully explicit scheme.

6.3.3 Heat Transfer

The general equation to be solved here is an adaptation of the bioheat equation for inclusion of adjective effects of the cooling system [103].

$$\frac{\partial T}{\partial t} = \underbrace{\nabla \cdot \left(\frac{k}{\rho C_p} \nabla T \right)}_{Diffusion} - \underbrace{\nabla \cdot (\mathbf{u}T)}_{\text{Advection}} + \underbrace{\frac{\sigma(T)}{2\rho C_p} |\mathbf{E}(T)|^2}_{\text{Source}} \tag{6.11}$$

where the solution variable is temperature, T. Material properties include thermal conductivity k, Density ρ, constant pressure specific heat capacity C_p, and temperature-sensitive effective conductivity, σ. The velocity field of the coolant fluid is used within the advection term, and temperature-sensitive electric field vector, $\mathbf{E}$, lies within the microwave heating source term.

During this thermal computation, insulating boundary conditions are set on the external surface of the tissue, and symmetric conditions at the axis of rotation. An implicit method is adopted to solve the heat transfer equation, and FEM is implemented across the entire domain Ω for full temperature distribution.

Additional derivations of the weak form of these fluid flow equations can be found in Appendix B.

6.4 Results

6.4.1 Simulation set-up

Three parameters of interest have been identified, the geometric position of coolant structure in design (as can be seen in Fig 6.2, controlled through dimension **L10**.), in addition to user-defined parameters for coolant such as flow rate and input temperature. Investigations were carried out by defining values for upper and lower limits for each of these parameters. The Limits used in this analysis are shown in Table 6.4.

Parameter	Lower limit	Upper limit
L10 $[mm]$	5	35
Flowrate $[ml/min]$	0	12
Temperature $[C]$	5	25

Table 6.4: Limits defined for this analysis of coolant position, flow rate, and temperature

Multiple simulations were executed, each changing the independent variable in an iterative fashion between the limits so that a complete set of data for temperature distribution throughout MWA is been created. As mentioned, investigations are readily possible through our user interface, allowing systematic MWA simulation and analysis of data. With this data, an analysis of the impact each of these variables has can be made.

6.4.2 Coolant positioning

To investigate the influence of coolant structure positioning on the thermal and SAR distributions, we systematically varied the position of the coolant channel, through **L10**, from 5mm to 35mm. Figure 6.6 shows several select points across this range to demonstrate variability in temperature distribution, with contours at 40 and 50°C.

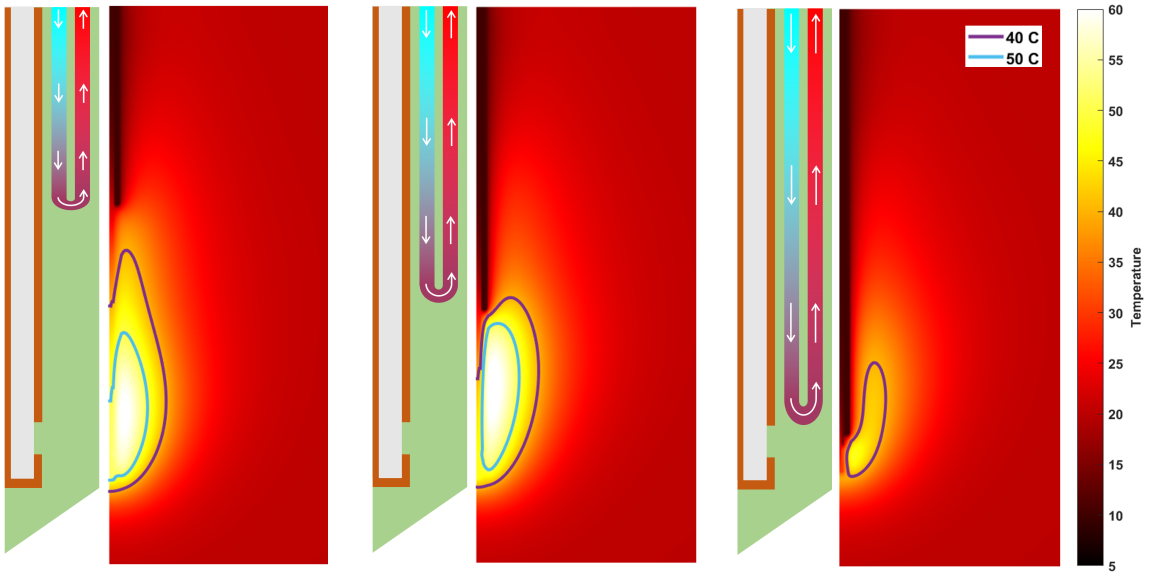

Figure 6.6: Temperature contour plot for various coolant structure positions after 150 seconds of power application. The accompanying probe illustrations indicate how fluid passes around the symmetric internal tubing and heats up as it does so. Contours of 40 and 50 °C are added to more clearly show the difference in temperature distribution, both of these temperatures are harmful to tissue depending on the length of exposure.

Although qualitative, a visual judgment can be made on the effect this change in internal design has upon the resulting temperature distribution. The cooling elements clearly confine the extent of heating to the distal end of the probe in this simulation, reducing the length of heating contours along the outer probe surface itself. However, Fig 6.6.right shows that if the cooling elements are designed such that they extend close to the slot position within the coaxial portion of the probe, significant loss of heating is experienced when compared to the other designs.

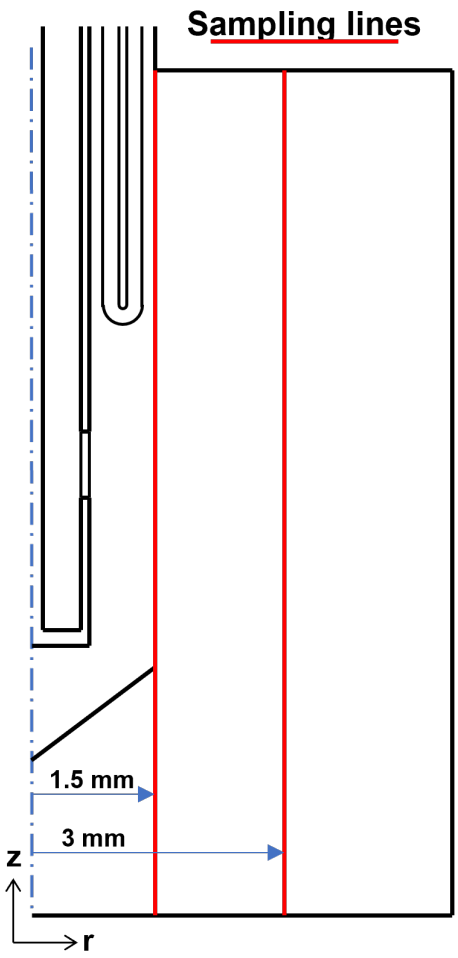

Figure 6.7: Two sampline lines, parallel to the probe axis, will be used to quantify changes in tissue temperature as a function of the longitudinal position of coolant tubes. the first line is on the probe surface at 1.5mm from the symmetric axis, the second is 3mm.

These differences between probes can be quantified through sampling temperature along a line through the domain, in parallel to the probe's longitudinal axis. This measurement becomes relevant when considering the primary objective of a cooled probe involves reducing the backward heating along the length of the probe, as such, Fig 6.7 shows the sampling method we will first present.

Figure 6.8 illustrates the temperature distribution on the probe surface for a range of different **L10** positions. Figure 6.9 similarly illustrates temperature distribution along a line parallel to the probe at 1.5mm distance from its surface, with probe slot position shown by thin black lines, and relative coolant apex for each L10 iteration highlighted

by the dashed coloured line.

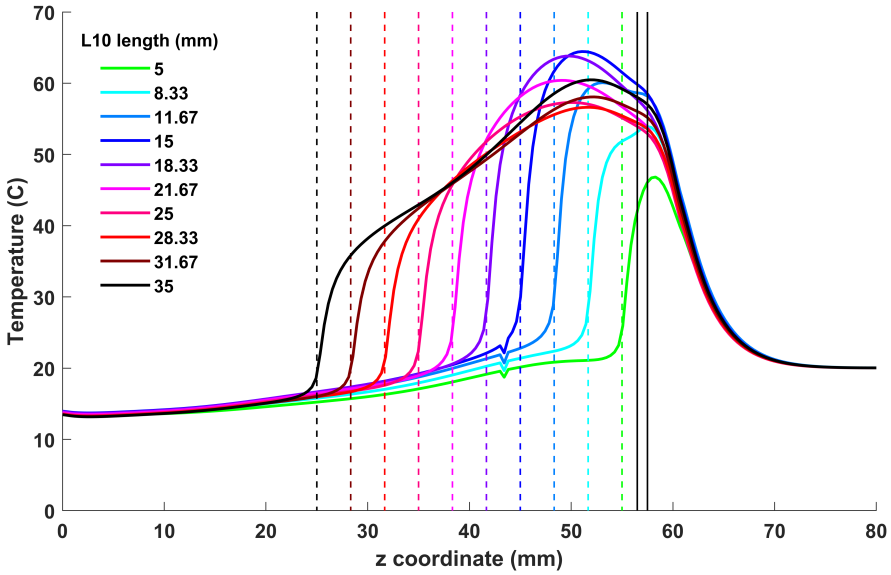

Figure 6.8: The temperature distribution along the length of the probe on the surface of the probe catheter. The center of the slot is located at the 57 mm position, and the relative coolant apex is shown by the dashed lines.

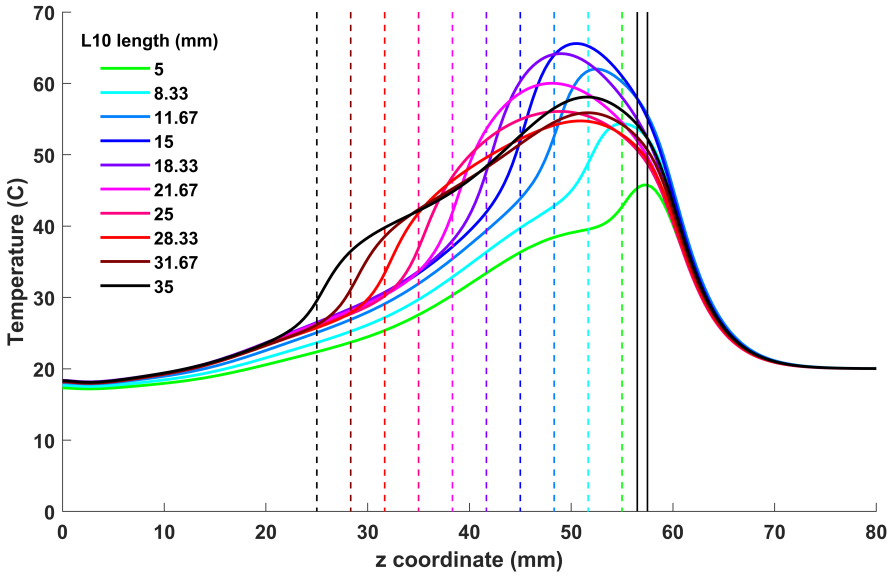

Figure 6.9: The temperature distribution along the length of the probe, at 3mm from the probe axis, 1.5mm from the catheter surface. Dashed lines again show the relative position of the coolant tube apex.

On the surface of the probe, Fig 6.8 shows the peak temperature increasing from 45°C with L10 at 5mm, to a maximum peak temperature of 65°C with L10 at 15mm,

beyond this value the peak temperatures reduce in the L10 range 15 - 25mm, before increasing again for the remaining designs simulated. Examining the location of these peaks shows between 5 - 25 mm there is a gradual shift upwards away from the probe tip, beyond this point though the peaks progress slightly towards the tip again. The distribution of the temperature is increasingly dispersed as L10 increases, showing higher temperatures at increasing lengths back along the probe.

A trend that can be seen in both datasets is the relatively steep temperature gradient that occurs close to each probe's respective cooling tube apex, indicated by the coloured dashed line. This phenomenon is more pronounced close to the probe surface as shown in Fig 6.8. Evidently, the elongated heating pattern that extends up the probe can be somewhat limited through the addition of such a cooling system, but these results alone do not explain why exactly this is. Two possible mechanisms by which the temperature profile is influenced are through absorption of thermal energy from the region, or by alteration of the SAR pattern generated from the probe. Although a combination of both of these methods contributes to the changes witnessed, plotting a similar graph for SAR values along the same sample line will show the extent to which SAR is changed. These results are shown in Fig 6.10.

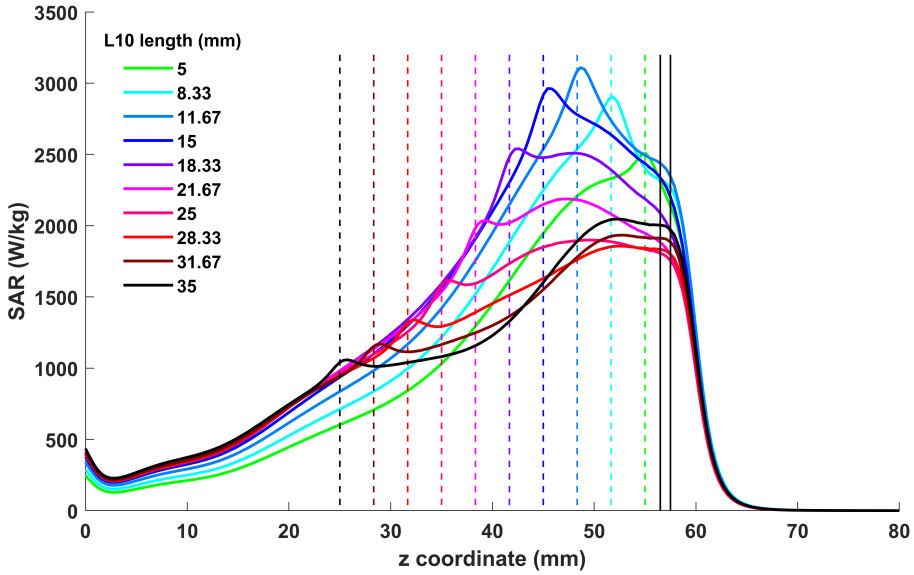

Figure 6.10: The SAR distribution along the length of the probe, at 1.5mm from the probe axis, on the catheter surface. Dashed lines again show the relative position of the coolant tube apex.

Here SAR values are shown at 3mm from the probe axis. Similarly to the equivalent temperature plots, there is a steep increasing gradient around the dotted lines that indicate the probe apex, suggesting that internal cooling has an influence on the electromagnetic field pattern within the tissue. Seeing as the SAR values are lower above the point of the coolant apex, this suggests the fluid within the cooling tubes has a dampening effect on the propagation of electromagnetic waves into the tissue, therefore acting to confine the field to the area beyond the cooling apex, towards the probe tip.

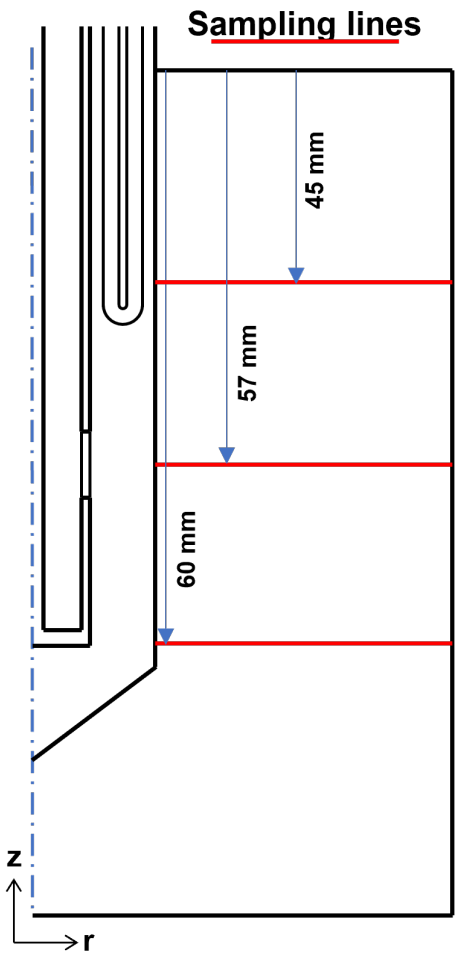

Figure 6.11: Three sample lines, in the r plane, will be used to quantify changes in tissue temperature with radius to highlight the temperature inverting nature of cooled probe designs. the first line is on the probe surface at 45mm from the base of the probe, the second is 57mm and the third is 60mm.

These results so far show how the length of temperature distributions can be somewhat truncated through the addition of a cooling system like this, with perhaps a preferable balance struck with the L10 = 15mm probe that offers a high peak temperature along with a sufficient spread of heat confined to the probe tip. We are also interested in seeing if these probe designs are capable of reducing charring at the probe-tissue interface whilst also maintaining ablative temperatures in the general locality of the probe tip. To achieve this the maximum temperature should occur a distance from the probe surface, with cooler temperatures at the interface. This kind of temperature inversion can be qualitatively seen in all sub-figures of Fig 6.6, but more detail can be drawn by sampling along a line in r-plane at various z positions,

as indicated in the line sample diagram Fig 6.11. An example of the temperature distribution measured on a non-cooled probe is shown in Fig 6.12, where it is clear the maximum temperature occurs at the points closest to the probe surface.

Three particular sample lines are taken, the first at 45mm along the probe, the second in line with the center of the slot, and the third in line with the end of the coaxial part of the probe. for conciseness of our results we picked 3 probes to investigate further, two extremes, L10 = 5mm and L10 = 35, but also the design we have just mentioned which seems to give high peak temperatures with reasonable confinement of heating, L10 = 15mm.

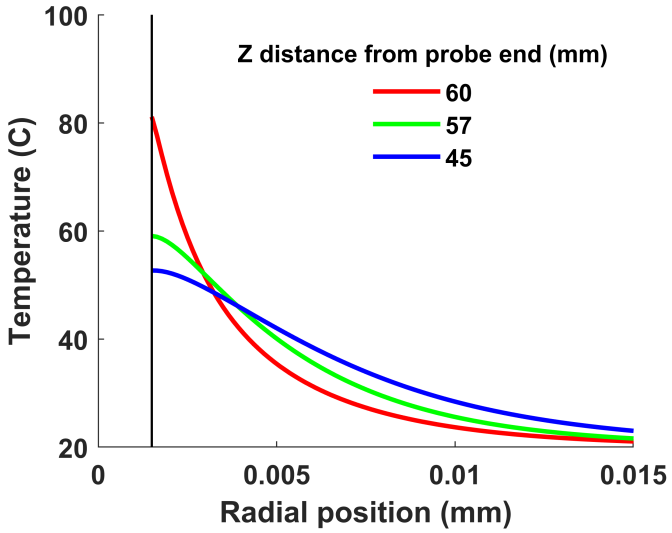

Figure 6.12: Temperature measured in the radial direction at various z positions on a non-cooled probe, the maximum temperature occurs on the probe surface, indicated by the black line, and therefore charring is likely to happen here first. Cooled probes can mitigate this effect by effectively pushing the maximum temperature point deeper into the tissue.

This uncooled case can be used as a reference when looking at the data for our three selected probes in Fig 6.13. All of these probes show a shift in maximum temperature away from the probe surface, the effect is suppressed at the z = 60mm mark due to the distance of this point from the coolant system itself. When comparing the three probes from each of the subfigures, the probe with L10 = 15mm (Fig 6.13.b) seems to maintain high temperatures close to that of the L10 = 5mm design (Fig 6.13.c), but with the

advantage of larger separation between probe surface and peat temperature. Although the L10 = 35mm (Fig 6.13.a) has the largest separation between peak temperature and probe surface, the maximum temperatures reached are significantly lower, which would limit the size and speed of ablation possible when compared to the other designs.

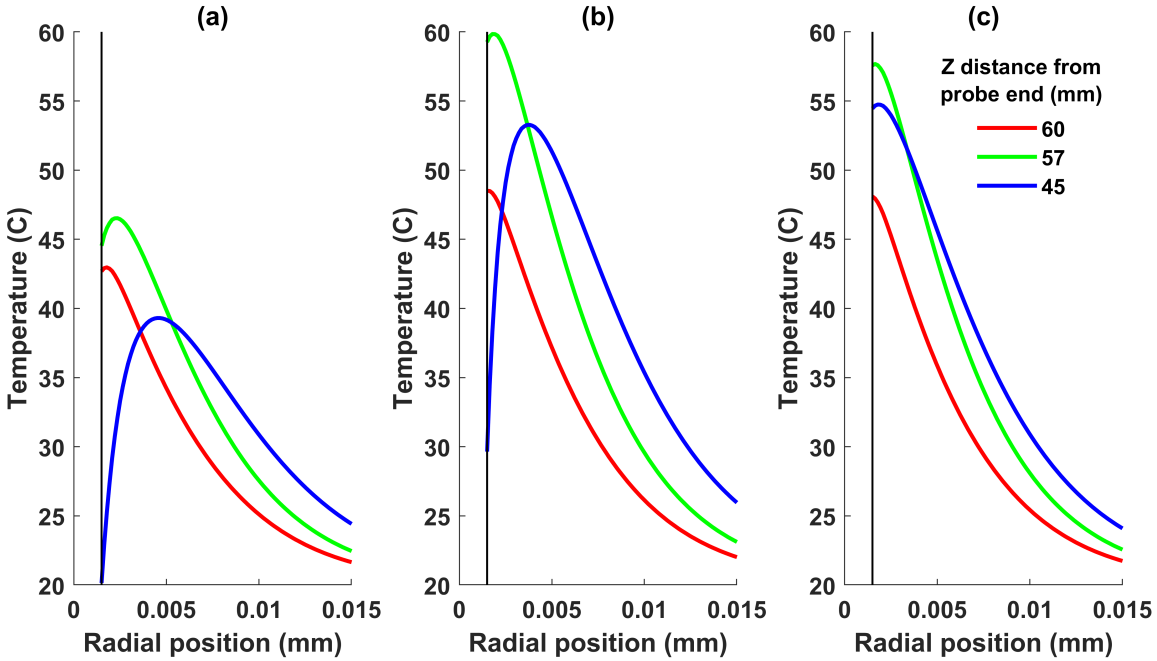

Figure 6.13: Temperature measured in the radial direction at various z positions for 3 cooled probes, a) L10 = 35mm, b) L10 = 15mm, c) L10 = 5mm. the maximum temperature occurs at various distances from the probe surface across the three sampling lines we have chosen.

6.4.3 Coolant flowrate

The second batch simulations use a spread of different coolant flow rates, from 0 to 13 ml/min. Geometry is constant throughout these simulations, with a **L10** of 15mm. Figure 6.14 shows the final temperature distributions at various flow rates, annotated with 40 and 50 °C contours.

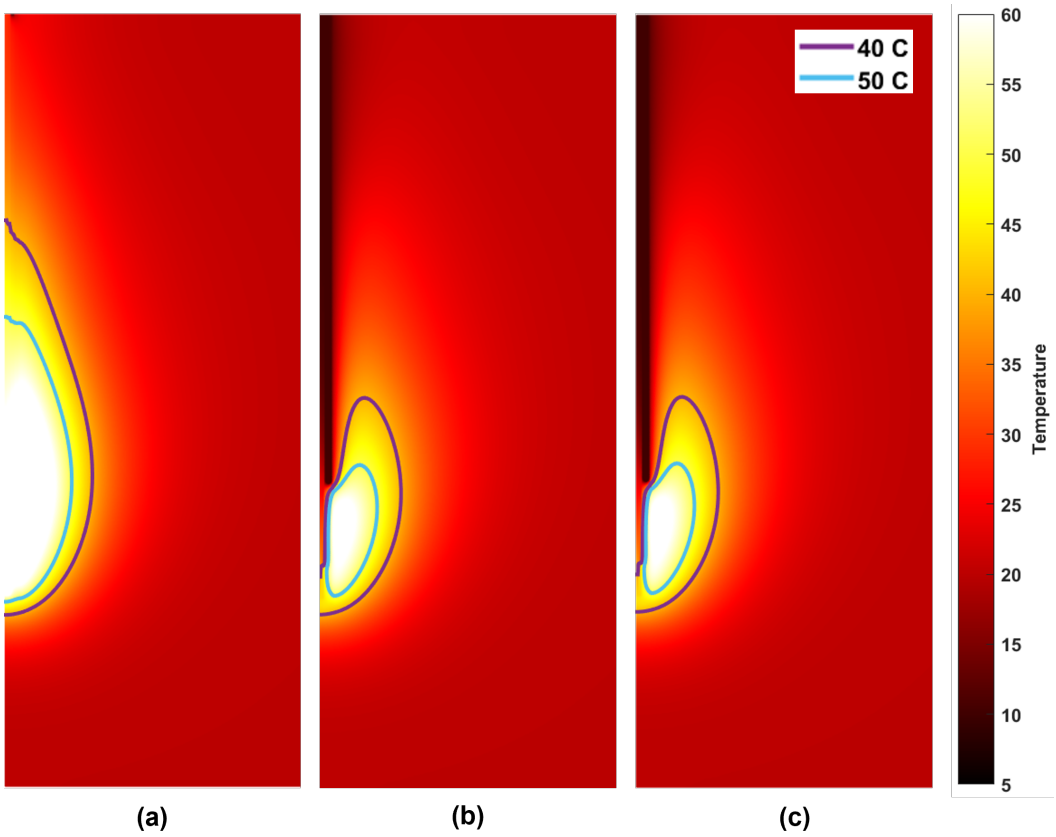

Figure 6.14: Results with changing coolant flow rate, a) 0 ml/min b) 5 ml/min c) 12 ml/min.

Visually there is a clear difference between no coolant flow and 5ml/min flow, but no differentiable between the 5ml/min and 12ml/min flow rates. To investigate this further, the data can be shown as a temperature against z coordinates along the probe surface, in Fig 6.15, or at 3mm from the axis of symmetry, Fig 6.16. These are the same sampling lines as introduced in Fig 6.7.

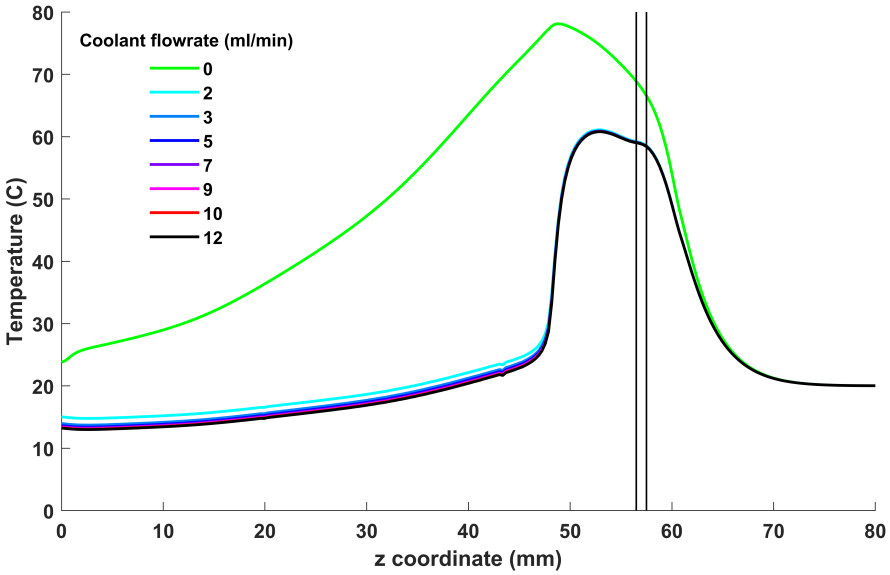

Figure 6.15: Temperature distribution along the probe surface from variable flow rate simulations.

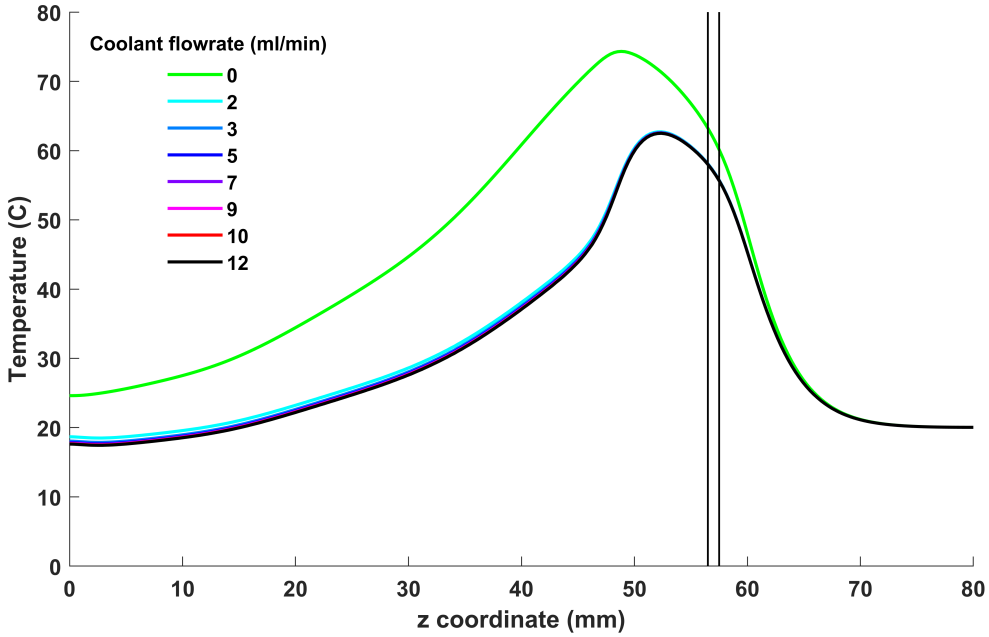

Figure 6.16: Temperature distribution along the probe surface from variable flow rate simulations.

All curves with a positive flowrate exhibit a similar shape in Fig 6.16, a gradient that steadily increases from the input at z = 0 to a peak at around z = 52mm of 60°C for positive flow rates. For the flowrate of 0 a higher peak occurs closer to the probe input at z = 48mm and with a magnitude of 75°C. Data shows a sharper drop

in temperatures on the probe surface, compared to at 3mm.

The spectrum of coolant flow rates tested reveals that a significant change in temperature distribution along the probe is caused when fluid cooling is applied, as visible by the differences between the coolant flowrates 0 and 12 in Fig 6.15. Here, heightened temperatures of between 10 and 20 °C are seen along the entire length of the probe, although this difference reduces at the distal end where cooling structures are not present. Of the flow rates tested greater than 0, the results show little difference and curves appear to converge.

6.4.4 Coolant temperature

The final variable investigated is the coolant input temperature. Like the previous simulation for flowrate analysis, a fixed geometry is used and coolant input temperature is the sole variable to be changed. Three temperatures are chosen, 5, 13 and 21°C. Figure 6.17 illustrates temperature distribution through the entire 2d domain at the conclusion of 150s of ablation for each of these temperatures.

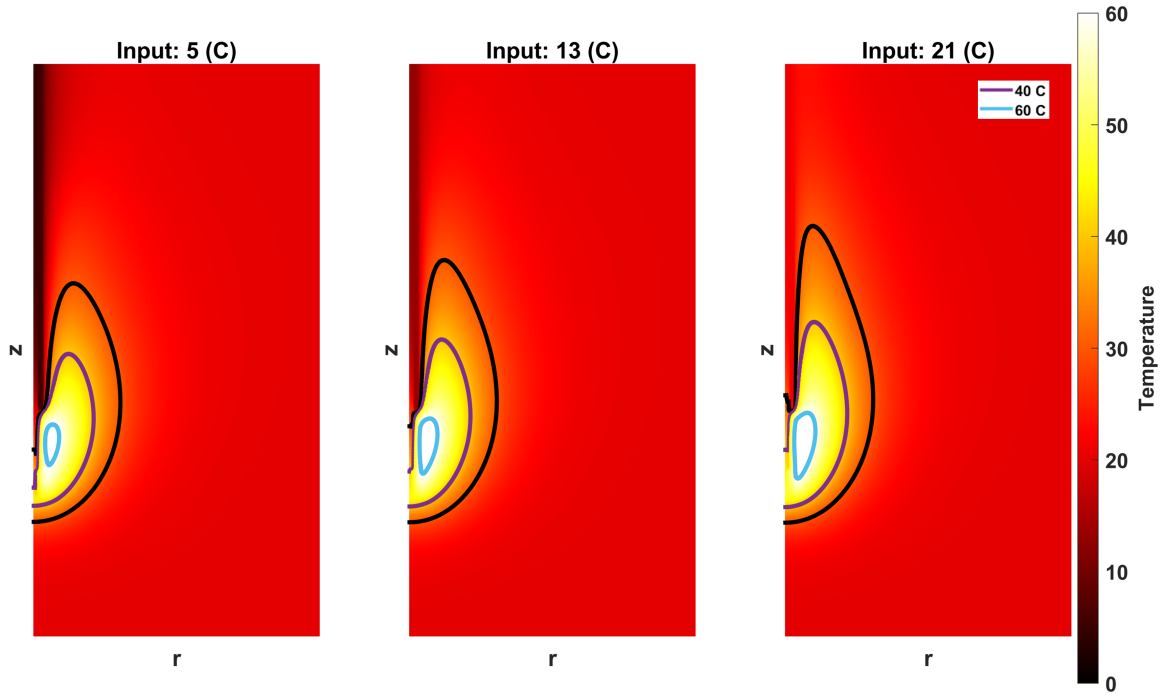

Figure 6.17: Temperature distribution with varying input coolant temperatures after 150 seconds of power application, using a coolant apex location defined by L10 = 15mm.

Temperature profile along the surface of the probe is seen to follow a similar shape, as in Fig 6.8, with the main difference being along the cooled length of the probe where lower cooling temperatures produce an associated cooler surface, this also holds true at the surface near the radiating slot portion of the probe.

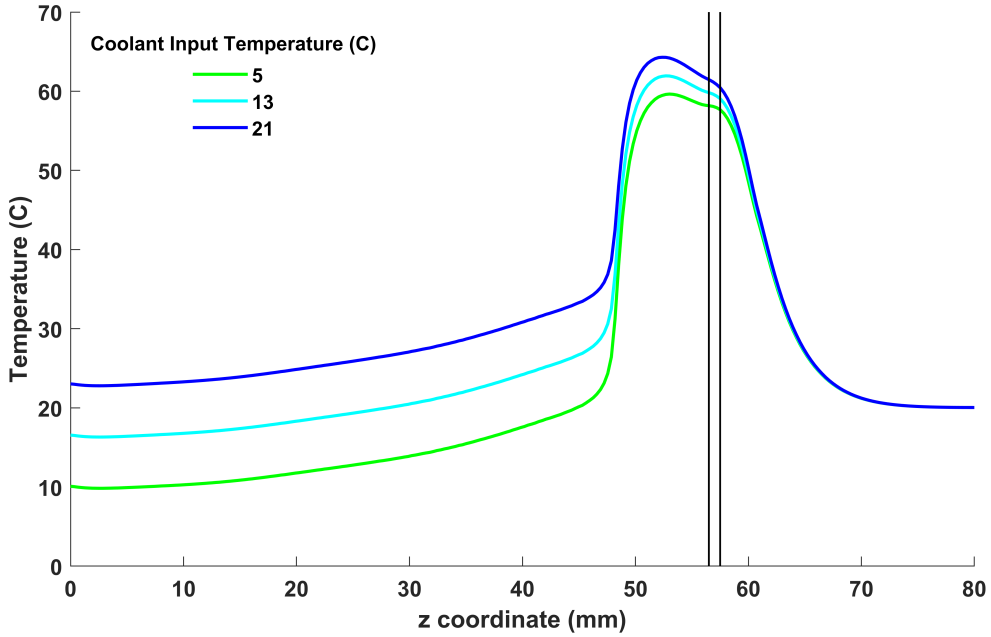

Figure 6.18: The temperature distribution, at various input coolant temperatures, along the length of the probe on the surface of the probe catheter. The center of the slot is located at the 57 mm position, indicated by the black vertical lines, and dashed lines indicate the relative position of the coolant tube apex.

At the 3mm radius curve trends are similar but with a more gradual gradient increase along the cooled probe length approaching the antenna slot, the difference between the temperature curves up to this point is lower than on the probe surface, suggesting that cooling effects are reduced with radial distance. Maximum temperatures occur at the same z position but are within a 10°C range, with the lowest coolant temperature creating the lowest peak temperature.

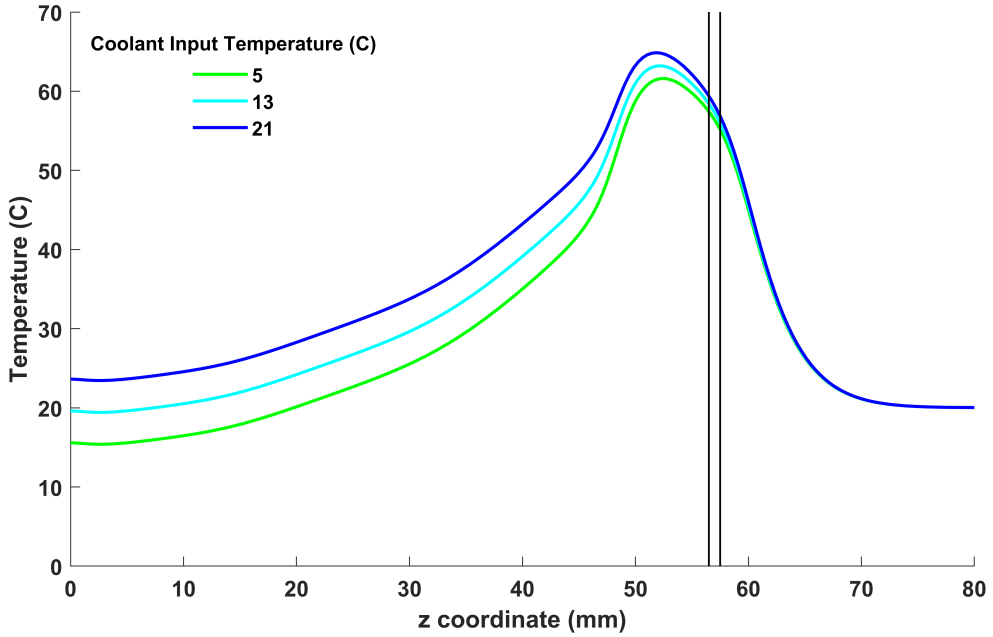

Figure 6.19: The temperature distribution, at various input coolant temperatures, along the length of the probe, at 3mm from the probe axis, 1.5mm from the catheter surface The center of the slot is located at the 57 mm position, indicated by the black vertical lines, and dashed lines indicate the relative position of the coolant tube apex.

Overall these simulations suggest lower coolant temperatures can reduce temperatures along the track of the probe at its surface and at a depth into the surrounding tissue, whilst still allowing high temperatures to be achieved in line with the probe slot.

6.5 Discussion

These simulations are consistent with the results of experimental studies on cooled ablation probes, which observed reduced levels of tissue charring adjacent to the probe surface [91][119]. This effect is illustrated in our simulations that employ variable coolant flow rates, demonstrating a significant decrease in temperature along the length of the probe when a positive flow rate (> 0 ml/min) is applied. It is this temperature reduction along the probe track that minimizes charring by maintaining the temperature at a lower, more controlled level.

To assess the validity of our cooled probe models, we compared our simulation data with findings from a study that measured temperature changes in ex vivo bovine liver during microwave thermal ablation [47]. Their study employed a cooled MWA probe operating at 2.45 GHz, with a setup involving a constant power application of 30 Watts for 10 minutes. Initial tissue temperatures were 15°C, with coolant input maintained at 10°C. Temperature was recorded using thermocouple probes positioned 5 mm from the probe surface and 10 mm from the antenna tip, corresponding to the point of maximum energy deposition.

While the detailed MWA probe design was not provided in the study, it referenced a water-cooled system described by [121], where cooling is confined to a region away from the active antenna tip. This concept aligns with our simulated probe design, making the experimental data a valuable benchmark for comparison.

In replicating these experimental conditions, we adapted our simulation setup to match key parameters, including the power settings, durations, tissue, and coolant temperatures. Based on our probe design, where maximum energy deposition occurs closer to the probe, we sampled measurements at 2 mm from the probe surface and 10 mm from the probe tip.

To refine the comparison, we replaced the Ji and Brace model [46] with a sigmoidal model fitted to experimentally derived permittivity and conductivity data from Lopresto

et al. [47]. The updated simulation results are presented in Figure 6.20, alongside the experimental temperature data from Lopresto et al. [47], which include 95% confidence intervals. The figure compares simulations using both the Ji and Brace model [46] and the experimentally fitted dielectric model.

The results demonstrate that the experimentally fitted model provides a closer match to the observed temperature progression, particularly during the phase of rapid heating. While the simulated results slightly exceed the confidence bounds of the experimental data, the overall agreement remains strong. These variations likely arise from differences in probe design or experimental setup, underscoring the importance of incorporating tissue-specific models to enhance simulation accuracy.

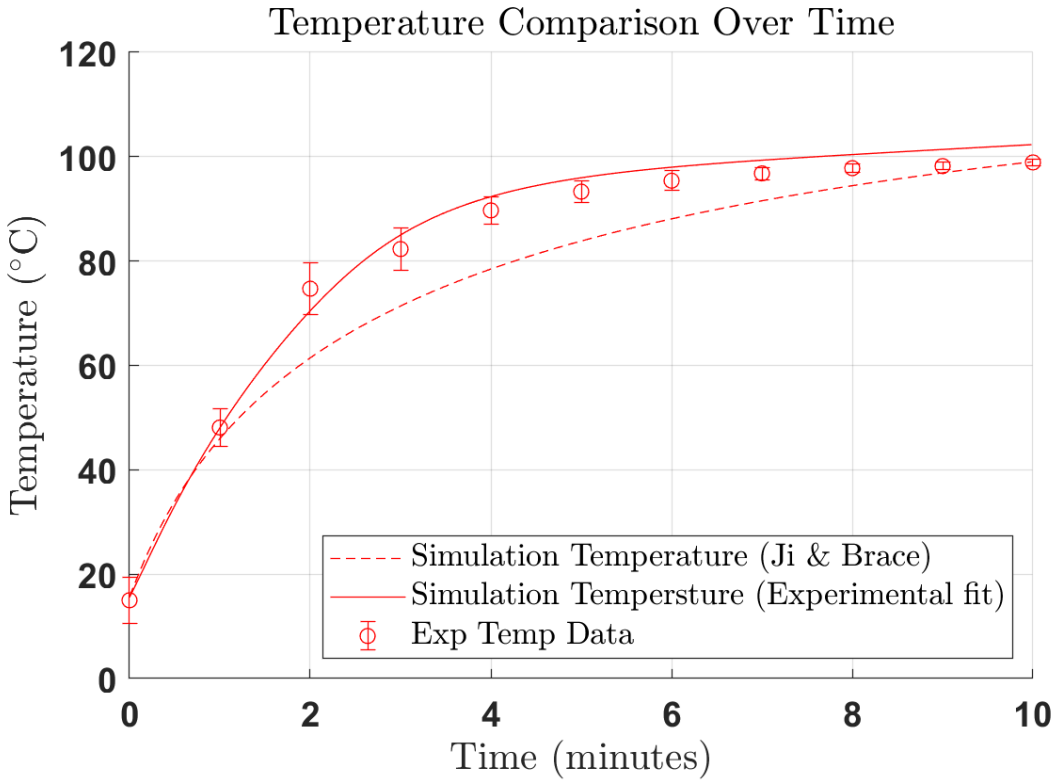

Figure 6.20: Comparison of simulated temperature profiles and experimental data [47] at the region of maximum energy deposition during ablation. Simulations were performed using the Ji and Brace model [46], which defines permittivity and conductivity as functions of temperature, and a sigmoidal model fitted to experimentally derived dielectric property data [47]. The experimental temperature data includes 95% confidence intervals.

The simulation outcomes suggest that optimizing the position of the cooling mechanism relative to the distal tip of the probe can enhance specific ablation characteristics. Specifically, a cooling system that extends close to the point of the radiating slot (L10 = 5mm) produces a peak temperature located closest to the end of the probe, which minimizes backheating effectively. On the other hand, positioning the coolant system at L10 = 15mm results in the highest maximum temperature achievable by the system, though this configuration does not confine heating as closely to the probe tip as the L10 = 5mm setup. This indicates that while L10 = 15mm maximizes the temperature, it extends the heating pattern along the probe, contrasting with the more confined heating effect seen at L10 = 5mm. These findings are in line with the work presented in [159], where a geometry was tested with two different coolant structure geometries: one close to the radiating tip of the probe and another further away. The design with coolant circulation extending close to the radiating tip yielded a shorter measured length of ablation and a more spherical ablation output.

Further analysis of the SAR values complements our temperature findings, highlighting the influence of coolant positioning on electromagnetic field dynamics within the probe. When the coolant circuit is positioned close to the radiating slot (L10 = 5mm), there is a reduction in peak SAR values. This suggests that a significant portion of the electromagnetic energy is absorbed by the coolant, attributed to the higher dielectric properties of water compared to the surrounding catheter material. Conversely, shifting the coolant structures apex to L10 = 15mm results in an increased peak and more dispersed SAR distribution along the probe length, which correlates with higher maximum temperatures and a more extended heating pattern observed in this configuration. As the coolant is moved further from the slot, beyond L10 = 15mm, the SAR pattern appears increasingly stretched. These observations underscore the importance of strategic coolant placement, taking into account its dielectric properties, for optimizing energy delivery and effectively controlling both thermal and SAR distributions.

Additionally, our simulations corroborate findings from experimental studies using variable coolant temperatures in ablation probes. These studies demonstrate that

higher coolant temperatures result in increased heating along the probe length, while lower temperatures facilitate a more controlled heating pattern, yielding experimental ablations with an axial ratio closer to 1 [125]. Similarly, our simulations indicate a notable decrease in temperature along the probe track as the coolant temperature is reduced, aligning with the experimental evidence that lower coolant temperatures can enhance the precision of the ablation process by reducing track heating.

The comparative analysis of different coolant flowrates and coolant input temperatures indicates a greater sensitivity of the temperature distribution to coolant temperature adjustments. Despite a range of flow rates tested, the variability in temperature profiles was less pronounced, suggesting a convergence in cooling efficacy at higher flow rates. This observation aligns with the findings from [94], where diminishing returns on cooling efficiency were noted beyond certain flow rate thresholds. This may be due to the observation that, while maintaining a necessary temperature gradient between the coolant and the probe is essential for heat removal, increasing the flow rate beyond a certain threshold does not enhance cooling effectiveness. This is because the rapid transit of coolant through the system limits the time it can absorb heat, thus preventing any substantial increase in heat absorption due to limited exposure time. In contrast, lowering the coolant temperature can significantly increase the temperature gradient between the coolant and the probe, therefore facilitating more effective heat removal. This highlights the significance of optimising coolant temperature for controlling probe temperature distributions.

To assess the validity of our cooled probe models, we compare our simulation data with findings from a study that measured dielectric properties and temperature changes in ex vivo bovine liver during microwave thermal ablation. This study used a cooled MWA probe at an operational frequency of 2.45 GHz. The setup involved constant power application of 30 Watts for 10 minutes, with initial tissue temperatures of 15 degrees Celsius and coolant input at 10 degrees Celsius. Permittivity measurements were taken using an open-ended coaxial probe, and temperature was measured with thermocouple probes, all of which are positioned 5mm from the probe surface and

10mm from the antenna tip, at the point of maximum energy deposition [47]. While the study does not provide detailed specifications of the MWA probe design, it does specify the use of a water-cooled system and makes reference to works by [121]. In this paper there are details of a cooled device, where the cooling system does not extend the entire length of the antenna, rather it acts in a region further along the probe, away from the active part of the antenna. This is similar to the concept used in our simulations and therefore could serve as a valuable comparison.

In attempting to replicate the experimental conditions, we adapted the simulation setup based on the specifics of our own cooled MWA probe, which indicated that maximum energy deposition occurred at a closer range. Consequently, we took measurement samples at 2mm from the probe surface and 10mm from the probe tip, where the highest energy deposition was observed. We maintained the same power settings and durations as the original experiment and initialized the tissue and coolant temperatures to match those used in the referenced study. Our results are presented comparatively with the original data, plotted with the 95% confidence interval bounds included, illustrating temperature and relative permittivity measurements throughout the procedure. Although our temperature data slightly exceeded the confidence bounds of the original measurements, they generally demonstrated close agreement, suggesting that variations may arise from differences in probe design or experimental setup. Our findings prompt further exploration into the interplay between coolant properties and probe design. Investigating the effects of cooling fluids with different dielectric properties, as well as extending simulations to encompass a wider array of probe designs, could provide deeper insights into optimizing MWA therapy. Moreover, incorporating experimental validation of these computational models would enhance the translational relevance of our research.

6.6 Conclusions

These simulations have shown that tuning of the internal design of a cooled microwave ablation probe such as the concept given here, can adjust the degree of backward-heating caused by elongated SAR patterns that hinders non cooled designs. By investigating

the effects of coolant structure positioning, flowrate, and temperature on thermal and SAR distributions, we have highlighted design parameters critical for optimizing probe performance. Notably, our results indicate a focus on coolant temperature adjustment over flowrate modulation to refine temperature control within MWA procedures.

7 Future Work

7.1 Post-ablation modelling

So far in this thesis the modeling has focussed solely on a assumption that power is applied to the probe instantaneously at the start of our simulations and remains constant throughout.

We have only focused on probe design up to this point, and the necessity to create a spherical SAR and temperature profile during the process of power application. More relevant from a clinical viewpoint would be to gain an understanding of the eventual extent of temperature distribution.

So far we have discussed data that extends only as far as the instant that power is removed, however, although less often considered in design simulations, changes in heat distribution will occur beyond the point in time where energy is no longer being transferred from the probe to the tissue volume. Simulating into this time frame beyond the active ablation would reveal how much change happen. Therefore an addition to the existing framework has been developed that allows modelling beyond the end of ablation to be conducted. This feature takes used inputs for the length of time to model after power is turned off, along with variable time stepping within that phase of ablation. The used interface used to carry out these simulations is shown in Fig 7.1.

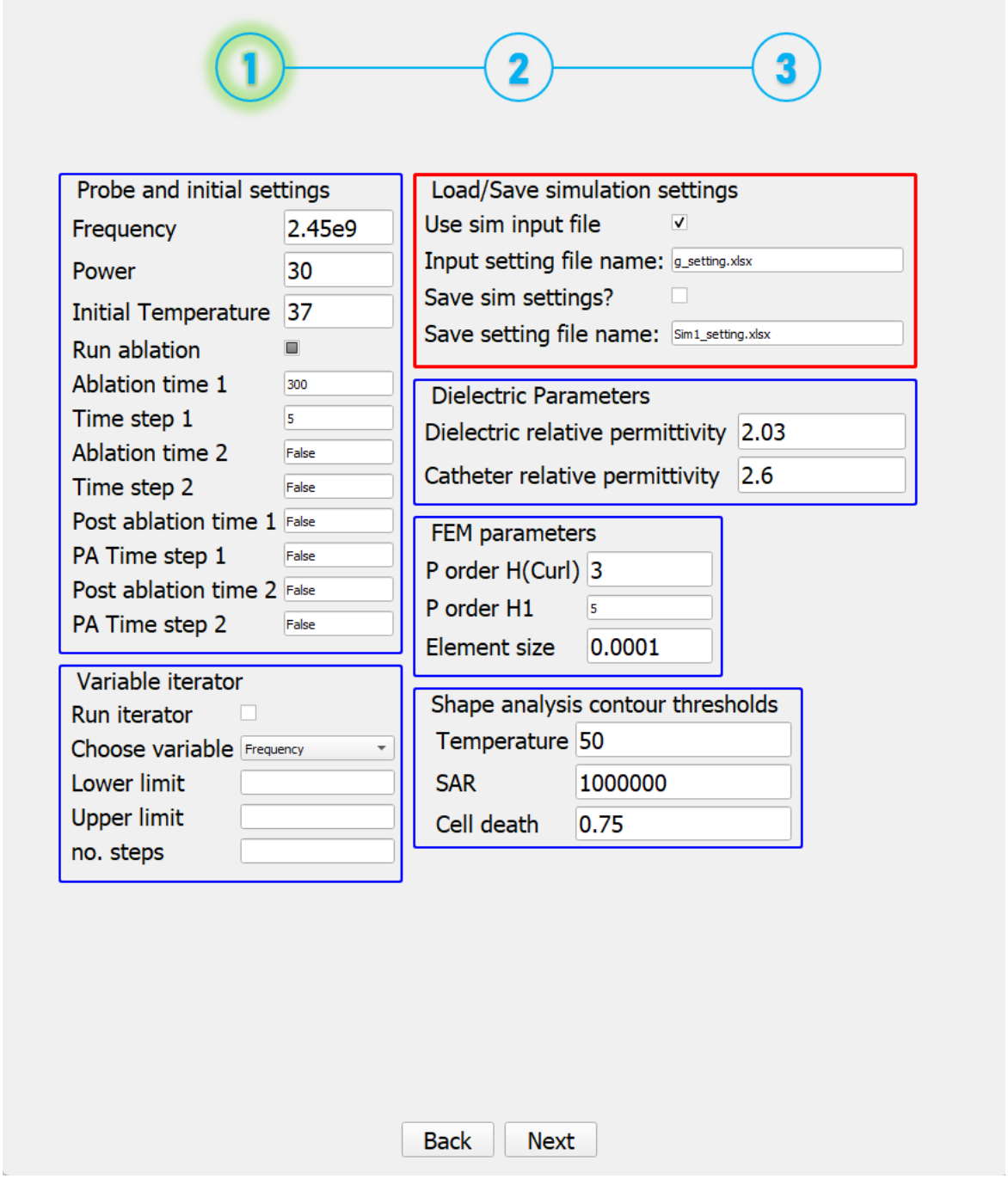

Figure 7.1: Within our user interface, variable time stepping can be specified within the block highlighted, this allows up to two different time stepping schemes during ablation, and a further two schemes that can instruct a period of post-ablation modelling. During this time the power to the probe is removed and therefore no electromagnetic source of heating is involved.

From this GUI extension, some preliminary simulations have been run and visualised in Fig 7.2. They indicate that the rate of temperature area increase reduces after power

is switched off (indicated by the vertical red line). These models could be used further in the future to build up a more complete picture of how ablation continues after probe removal.

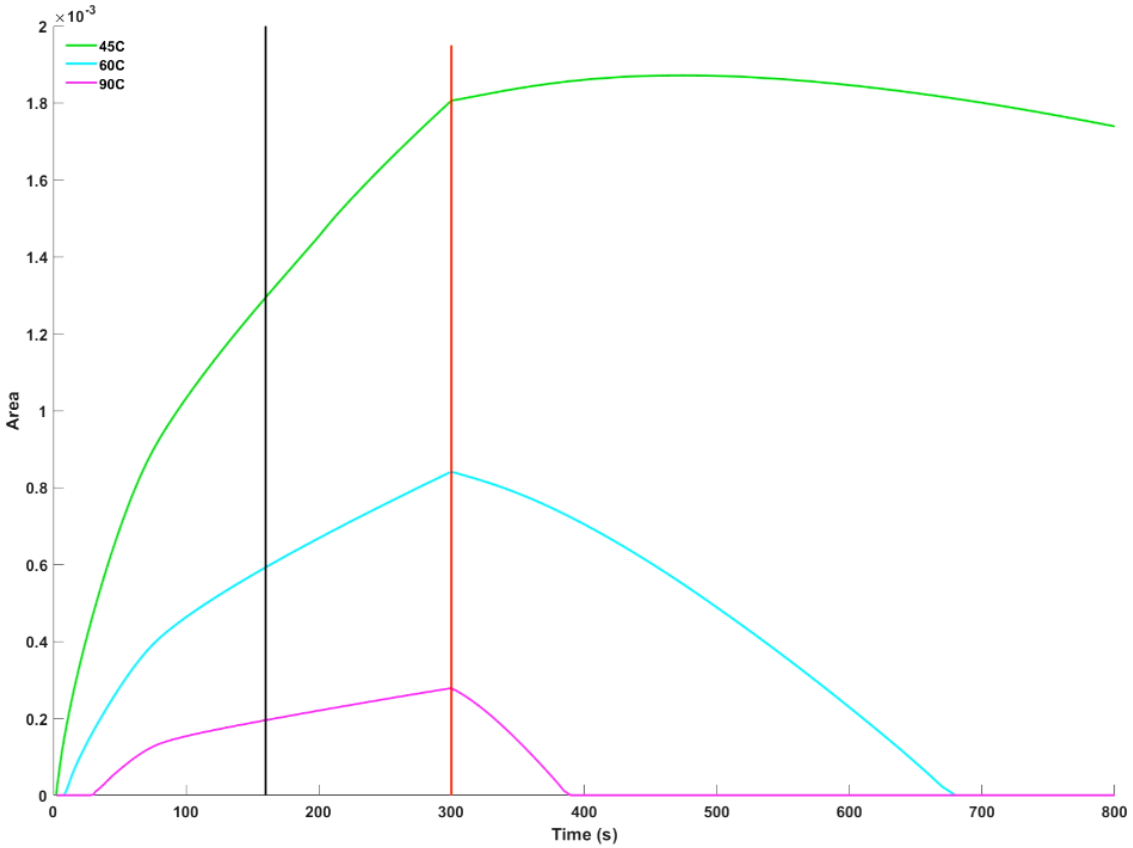

Figure 7.2: An example of the results achieved from the long ablation simulation within our visualisation codes, we have the areas bounded by these three isocontours through ablation, as discussed in chapter 5.

7.2 Integrated tissue damage models

A promising direction for future enhancements of our framework involves the integration of cell health estimation throughout the ablation process. To facilitate this, we plan to incorporate the established three-state mathematical model of hyperthermic cell death, as detailed in [160]. This model, which categorizes cells into one of three states—alive (A), vulnerable (V), or dead (D)—is widely recognized in the field of thermal therapy. Although not novel, it has been effectively applied in various microwave ablation studies to simulate the thermal stress response in cells. Our aim is not to innovate a new model but to adapt this proven model into our open-source framework to expand its analytical capabilities. This integration will allow for more comprehensive simulations, offering insights into the thermal effects of ablation on cell viability, which could significantly enhance treatment planning and outcomes. For references to other MWA studies that employ this model, see [94, 48, 161]

The transition from alive to vulnerable represents initial damage to cells, inducing a state where the cell is no longer functioning normally. Once past a critical point the cell progresses to a state from which the cell cannot return. The rate of this process is defined as k_f.

$$A \xrightarrow{k_f} V \xrightarrow{k_f} D \tag{7.1}$$

The transition from vulnerable to alive represents the self-healing process whereby an injured cell can recover to its fully functional alive state. The rate of this healing process is defined as k_b.

$$A \xleftarrow{k_b} V \tag{7.2}$$

These cell damage and recovery equations combine to form Eq 7.3. If all cells exist within one of the three possible states: $A + V + D = 1$. The ODE system can be written as

$$A \underset{k_b}{\overset{k_f}{\rightleftarrows}} V \xrightarrow{k_f} D, \tag{7.3}$$

$$\frac{dA}{dt} = -k_f A + k_b(1 - A - D), \tag{7.4}$$

$$\frac{dD}{dt} = k_f(1 - A - D). \tag{7.5}$$

For this model to work, the forward rate k_f must increase with temperature above 37°C, and reflect that the highly damaged tissue is more susceptible to further damage. Therefore, it can be written as

$$k_f = \bar{k_f} e^{\frac{T}{T_k}} (1 - A). \tag{7.6}$$

Where $\bar{k_f}$ is a scaling constant, parameter T_k sets the rate of exponential increase with temperature. $\bar{k_f}$, k_b and T_k parameters were determined by minimising error when compared to experimental datasets. The values yielded from this fitting process are give in table 7.1.

Variable	Value	Unit
$\bar{k_f}$	3.52×10^{-3}	s^{-1}
T_k	41.6	°C
k_b	8.46×10^{-3}	s^{-1}

Table 7.1: Parameters used in within the cell death equations.

Using this model, transient changes in cell health can be predicted and quantified as a fraction of all the cells at any given point. An example of this is given in Fig 7.3, where proportions of healthy, vulnerable and dead cells are shown at a given point heated at 100°C for 300s.

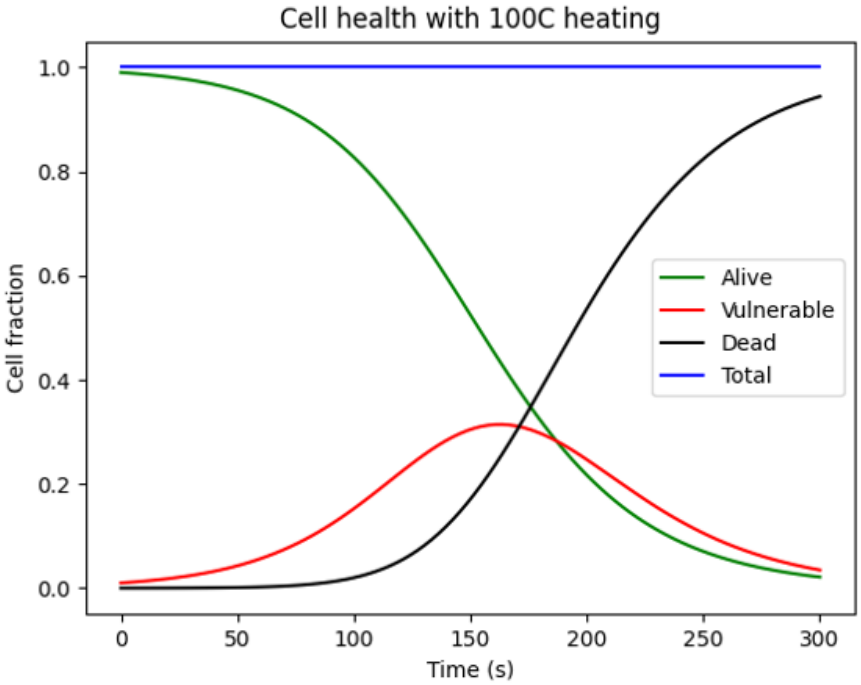

Figure 7.3: Fractions of cells throughout heating.

This ODE system can readily be built into the existing framework, and the GUI adjusted accordingly, so that cell fractions are output as another variable from our simulations along with those such as SAR and Temperature. Figure 7.4 gives an example of the results from these simulations.

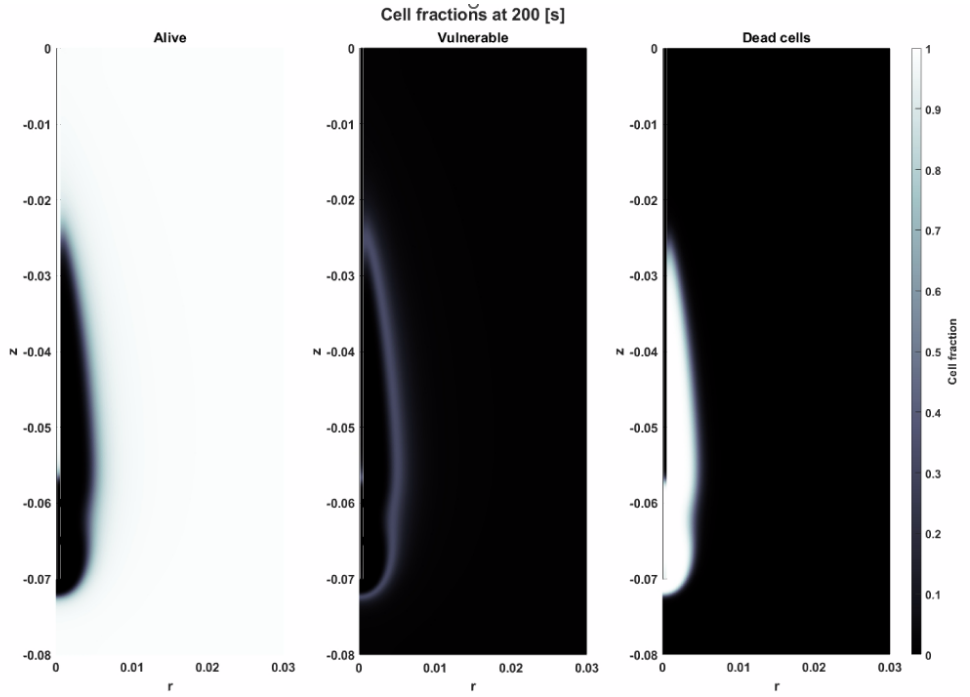

Figure 7.4: Temperature area

As you might expect, the region bounding the alive cells has a thin layer of vulnerable cells that transition into the dead cells closer to the probe where higher temperatures have been achieved for longer.

Although preliminary, these results in the future could be used in combination with the existing data outputs to further investigate cell health with time and temperature, along with relatively easy adjustment of our codes if other cell health models are to be tested.

To conclude, Modelling of microwave ablation remains a highly exciting multi-physics problem with many open avenues of potential investigation still existing. In addition to the work presented here, the natural progression of this modelling would be to expand from the current two dimensional axisymmetric model into a three dimensional domain. This would allow more complex probe designs to be explored that aren't currently possible to their non symmetric design, furthermore, a 3D model can allow features within the surrounding tissue to be modelled such as irregular shaped tumours, large blood vasculature and layers of tissue. Although these would come at a computational expense. Other Features that would be beneficial to incorporate include tissue shrinkage

and skin effect within the probe itself that contributes to the heating along the track of the probe. All of which would contribute to a more realistic simulation of ablation.

Another consideration should be design feasibility. As this project has considered purely in silico modelling, future experimental work would indicate how easily such a probe design could be constructed, and highlight how the existing framework can be improved to move closer to a realistic representation of ablation.

References

[1] H. Fallahi and P. Prakash. "Antenna Designs for Microwave Tissue Ablation". In: *Critical Reviews™ in Biomedical Engineering* 46.6 (2018), pp. 495–521. ISSN: 0278-940X. DOI: 10.1615/CritRevBiomedEng.2018028554.

[2] Mario Rubio. "Coaxial Slot Antenna Design for Microwave Hyperthermia using Finite- Difference Time-Domain and Finite Element Method". In: *The Open Nanomedicine Journal* 3 (May 2011), pp. 2–9. DOI: 10.2174/1875933501103010002.

[3] J. Ferlay et al. "Global Cancer Observatory: Cancer Today". In: (2020). Lyon: International Agency for Research on Cancer. URL: https://gco.iarc.fr/today.

[4] GBD 2019 Cancer Risk Factors Collaborators. "The global burden of cancer attributable to risk factors 2010–19: a systematic analysis for the Global Burden of Disease Study 2019". In: *Lancet* 400.10352 (2022), pp. 563–591. DOI: 10.1016/S0140-6736(22)01438-6.

[5] *Treatment For Cancer — Cancer Treatment Options.* https://www.cancer.org/treatment/treatments-and-side-effects/treatment-types.html. Accessed: 15-12-2023. American Cancer Society.

[6] *Types of Cancer Treatment.* https://www.cancer.gov/about-cancer/treatment. Accessed: 15-12-2023. National Cancer Institute.

[7] Muneeb Ahmed et al. "Principles of and Advances in Percutaneous Ablation". In: *Radiology* 258.2 (2011). PMID: 21273519, pp. 351–369. DOI: 10.1148/radiol.10081634. eprint: https://doi.org/10.1148/radiol.10081634. URL: https://doi.org/10.1148/radiol.10081634.

[8] Dr Andrew Renaut. *What are the pros and cons of laparoscopic surgery and open surgery for hernia repair?* 2018. URL: https://brisbanesurgeon.com.au/news/what-are-pros-and-cons-laparoscopic-surgery-and-open-surgery-hernia-repair.

[9] Claudius Conrad and Brice Gayet. *Laparoscopic liver, pancreas, and biliary surgery.* John Wiley & Sons, 2016.

[10] Samer Tohme, Richard L Simmons, and Allan Tsung. "Surgery for Cancer: A Trigger for Metastases". In: *Cancer Research* 77.7 (2017), pp. 1548–1552. DOI: 10.1158/0008-5472.CAN-16-1536.

[11] J. C. Coffey et al. "Cancer surgery: risks and opportunities". In: *Bioessays* 28.4 (2006), pp. 433–437. DOI: 10.1002/bies.20381.

[12] Stijn Van Esser et al. "Minimally invasive ablative therapies for invasive breast carcinomas: an overview of current literature". In: *World journal of surgery* 31 (2007), pp. 2284–2292.

[13] John G Baust et al. "Advances in cryoablation and thermal ablation therapy for treating small renal masses". In: *Current Opinion in Urology* 28.3 (2018), pp. 307–315.

[14] Christopher Brace. "Microwave Tissue Ablation: Biophysics, Technology, and Applications". In: *Critical reviews in biomedical engineering* 38 (Jan. 2010), pp. 65–78. DOI: 10.1615/CritRevBiomedEng.v38.i1.60.

[15] Chris Brace. "Thermal Tumor Ablation in Clinical Use". In: *IEEE Pulse* 2.5 (Sept. 2011), pp. 28–38. ISSN: 2154-2317. DOI: 10.1109/MPUL.2011.942603.

[16] Breastcancer.org. *Surgical Margins*. 2018. URL: https://www.breastcancer.org/symptoms/diagnosis/margins.

[17] National Cancer Institute. *Definition of resorption*. NCI Dictionary of Cancer Terms. Accessed: 2023-04-15. National Cancer Institute. URL: https://www.cancer.gov/publications/dictionaries/cancer-terms/def/resorption.

[18] Radovan Slovak et al. "Immuno-thermal ablations – Boosting the anticancer immune response". In: *Journal of Immunotherapy and Precision Oncology* 1.1 (2018), pp. 26–35.

[19] John G. Baust et al. "Defeating cancers' adaptive defensive strategies using thermal therapies: Examining cancer's therapeutic resistance, ablation, and immune response". In: *Translational Research* 204 (2018), pp. 31–47.

[20] J. Louis Hinshaw et al. “Percutaneous Tumor Ablation Tools: Microwave, Radiofrequency, or Cryoablation—What Should You Use and Why?” In: *RadioGraphics* 34.5 (2014). PMID: 25208284, pp. 1344–1362. DOI: 10.1148/rg.345140054. eprint: https://doi.org/10.1148/rg.345140054. URL: https://doi.org/10.1148/rg.345140054.

[21] J. G. Lynn et al. “A New Method For The Generation And Use Of Focused Ultrasound In Experimental Biology”. In: *J Gen Physiol* 26.2 (Nov. 1942), pp. 179–93. DOI: 10.1085/jgp.26.2.179.

[22] M. Alkhorayef et al. “High-Intensity Focused Ultrasound (HIFU) in Localized Prostate Cancer Treatment”. In: *Pol J Radiol* 80 (2015), pp. 131–141. DOI: 10.12659/PJR.892341.

[23] P. M. Hewitt et al. “A Comparative Laboratory Study of Liquid Nitrogen and Argon Gas Cryosurgery Systems”. In: *Cryobiology* 35.4 (1997), pp. 303–308. ISSN: 0011-2240. DOI: https://doi.org/10.1006/cryo.1997.2039. URL: https://www.sciencedirect.com/science/article/pii/S0011224097920393.

[24] Duke K. Bahn et al. “Targeted cryoablation of the prostate: 7-year outcomes in the primary treatment of prostate cancer”. In: *Urology* 60.2, Supplement 1 (2002). 2s1, pp. 3–11. ISSN: 0090-4295. DOI: https://doi.org/10.1016/S0090-4295(02)01678-3. URL: https://www.sciencedirect.com/science/article/pii/S0090429502016783.

[25] Masafumi Kawamura et al. “Percutaneous cryoablation of small pulmonary malignant tumors under computed tomographic guidance with local anesthesia for nonsurgical candidates”. In: *The Journal of Thoracic and Cardiovascular Surgery* 131.5 (2006), pp. 1007–1013. ISSN: 0022-5223. DOI: https://doi.org/10.1016/j.jtcvs.2005.12.051. URL: https://www.sciencedirect.com/science/article/pii/S0022522306001401.

[26] J.G. Baust et al. “Mechanisms of cryoablation: Clinical consequences on malignant tumors”. In: *Cryobiology* 68.1 (2014), pp. 1–11. ISSN: 0011-2240. DOI:

https://doi.org/10.1016/j.cryobiol.2013.11.001. URL: https://www.sciencedirect.com/science/article/pii/S001122401300396

[27] M. R. Callstrom and J. W. Charboneau. "Technologies for ablation of hepatocellular carcinoma". In: *Gastroenterology* 134 (2008), pp. 1831–1835. DOI: 10.1053/j.gastro.2008.05.037.

[28] E. M. Mazaris, I. M. Varkarakis, and S. B. Solomon. "Percutaneous renal cryoablation: current status". In: *Future Oncology* 4 (2008), pp. 257–269. DOI: 10.2217/14796694.4.2.257.

[29] R. A. McTaggart and D. E. Dupuy. "Thermal ablation of lung tumors". In: *Tech Vasc Interv Radiol* 10 (2007), pp. 102–113. DOI: 10.1053/j.tvir.2007.08.002.

[30] C. R. Ritch and A. E. Katz. "Prostate cryotherapy: current status". In: *Current Opinion in Urology* 19 (2009), pp. 177–181. DOI: 10.1097/MOU.0b013e328329c328.

[31] P. J. Littrup et al. "Cryotherapy for breast cancer: a feasibility study without excision". In: *J Vasc Interv Radiol* 20 (2009), pp. 1329–1341. DOI: 10.1016/j.jvir.2009.06.017.

[32] Kijung Kwak et al. "Recent progress in cryoablation cancer therapy and nanoparticles mediated cryoablation". In: *Theranostics* 12 (Feb. 2022), pp. 2175–2204. DOI: 10.7150/thno.67530.

[33] A. A. Gage and J. G. Baust. "Cryosurgery for tumors—a clinical overview". In: *Technol Cancer Res Treat* 3 (2004), pp. 187–199.

[34] Siti Fatimah Abdul Halim et al. "A Review on Magnetic Induction Spectroscopy Potential for Fetal Acidosis Examination". In: *Sensors* 22 (Feb. 2022), p. 1334. DOI: 10.3390/s22041334.

[35] André vander Vorst, Arye. Rosen, and Youji Kotsuka. *RF/microwave interaction with biological tissues*. eng. Wiley series in microwave and optical engineering ; 181. Hoboken, New Jersey: John Wiley & Sons, 2006. ISBN: 1-280-34967-0.

[36] Kenneth S. Cole and Robert H. Cole. “Dispersion and Absorption in Dielectrics I. Alternating Current Characteristics”. In: *The Journal of Chemical Physics* 9.4 (Apr. 1941), pp. 341–351. ISSN: 0021-9606. DOI: 10.1063/1.1750906. eprint: https://pubs.aip.org/aip/jcp/article-pdf/9/4/341/18792177/341_1_online.pdf. URL: https://doi.org/10.1063/1.1750906.

[37] Vera V. Daniel. “Dielectric relaxation”. In: *(No Title)* (1967).

[38] C. Gabriel, S. Gabriel, and E. Corthout. “The dielectric properties of biological tissues: I. Literature survey”. In: *Physics in Medicine & Biology* 41.11 (Nov. 1996), p. 2231. DOI: 10.1088/0031-9155/41/11/001. URL: https://dx.doi.org/10.1088/0031-9155/41/11/001.

[39] S. Gabriel, R. W. Lau, and C. Gabriel. “The dielectric properties of biological tissues: II. Measurements in the frequency range 10 Hz to 20 GHz”. In: *Physics in Medicine & Biology* 41.11 (Nov. 1996), p. 2251. DOI: 10.1088/0031-9155/41/11/002. URL: https://dx.doi.org/10.1088/0031-9155/41/11/002.

[40] S. Gabriel, R. W. Lau, and C. Gabriel. “The dielectric properties of biological tissues: III. Parametric models for the dielectric spectrum of tissues”. In: *Physics in Medicine & Biology* 41.11 (Nov. 1996), p. 2271. DOI: 10.1088/0031-9155/41/11/003. URL: https://dx.doi.org/10.1088/0031-9155/41/11/003.

[41] H.P. Schwan. “Electrical properties of tissues and cell suspensions: mechanisms and models”. In: *Proceedings of 16th Annual International Conference of the IEEE Engineering in Medicine and Biology Society*. Vol. 1. 1994, A70–A71 vol.1. DOI: 10.1109/IEMBS.1994.412155.

[42] Anna Bottiglieri et al. “Exploiting Tissue Dielectric Properties to Shape Microwave Thermal Ablation Zones”. In: *Sensors* 20.14 (2020). ISSN: 1424-8220. DOI: 10.3390/s20143960. URL: https://www.mdpi.com/1424-8220/20/14/3960.

[43] Marija Radmilović-Radjenović et al. “Finite Element Analysis of the Microwave Ablation Method for Enhanced Lung Cancer Treatment”. In: *Cancers* 13.14 (2021). ISSN: 2072-6694. DOI: 10.3390/cancers13143500. URL: https://www.mdpi.com/2072-6694/13/14/3500.

[44] Mariya Lazebnik et al. “Ultrawideband temperature-dependent dielectric properties of animal liver tissue in the microwave frequency range”. In: *Physics in medicine and biology* 51 (May 2006), pp. 1941–55. DOI: 10.1088/0031-9155/51/7/022.

[45] Christopher Brace. “Temperature-dependent dielectric properties of liver tissue measured during thermal ablation: Toward an improved numerical model”. In: *Conference proceedings : ... Annual International Conference of the IEEE Engineering in Medicine and Biology Society. IEEE Engineering in Medicine and Biology Society. Conference* 2008 (Feb. 2008), pp. 230–3. DOI: 10.1109/IEMBS.2008.4649132.

[46] Zhen Ji and Christopher Brace. “Expanded modeling of temperature-dependent dielectric properties for microwave thermal ablation”. In: *Physics in medicine and biology* 56 (Aug. 2011), pp. 5249–64. DOI: 10.1088/0031-9155/56/16/011.

[47] Vanni Lopresto et al. “Changes In The Dielectric Properties Of Ex Vivo Bovine Liver During Microwave Thermal Ablation At 2.45 Ghz”. In: *Physics in Medicine & Biology* 57.8 (2012), p. 2309. DOI: 10.1088/0031-9155/57/8/2309.

[48] Masoud H. H. Tehrani et al. “Use of microwave ablation for thermal treatment of solid tumors with different shapes and sizes—A computational approach”. In: *PLOS ONE* 15.6 (June 2020), pp. 1–20. DOI: 10.1371/journal.pone.0233219. URL: https://doi.org/10.1371/journal.pone.0233219.

[49] L. W. Organ. “Electrophysiologic principles of radiofrequency lesion making.” In: *Applied neurophysiology* 39 2 (1976), pp. 69–76. URL: https://api.semanticscholar.org/CorpusID:35646844.

[50] Servet Tatli et al. “Radiofrequency ablation: technique and clinical applications”. In: *Diagnostic and Interventional Radiology* 18.5 (2012), p. 508.

[51] Kelvin Hong and Christos Georgiades. “Radiofrequency Ablation: Mechanism of Action and Devices”. In: *Journal of Vascular and Interventional Radiology* 21.8, Supplement (2010). Thermal Ablation 2010: At the Crossroads of Past Success, Current Goals, and Future Technology, S179–S186. ISSN: 1051-0443. DOI: https://doi.org/10.1016/j.jvir.2010.04.008. URL: https://www.sciencedirect.com/science/article/pii/S1051044310004136.

[52] Dieter Haemmerich. “Biophysics of Radiofrequency Ablation”. In: *Critical reviews in biomedical engineering* 38 (Jan. 2010), pp. 53–63. DOI: 10.1615/CritRevBiomedEng.v38.i1.50.

[53] Kenneth R. Foster and Michael H. Repacholi. *Radiofrequency*. CRC Press, 2007.

[54] David J. Schutt and Dieter Haemmerich. “Sequential Activation of a Segmented Ground Pad Reduces Skin Heating During Radiofrequency Tumor Ablation: Optimization via Computational Models”. In: *IEEE Transactions on Biomedical Engineering* 55.7 (2008), pp. 1881–1889. DOI: 10.1109/TBME.2008.919740.

[55] Yukio Osaki et al. “Clinical effectiveness of bipolar radiofrequency ablation for small liver cancers”. In: *Journal of gastroenterology* 48 (2013), pp. 874–883.

[56] Jia-peng Wu et al. “US-guided ablation of tumors – where is it used and how did we get there, Radiofrequency”. In: *Med-X* 1 (July 2023). DOI: 10.1007/s44258-023-00002-2.

[57] Christian Stroszczynski and Gunnar Gaffke. “Use Of Imaging Modalities For The Guidance Of Minimally Invasive Tumor Therapies (mitt)”. In: *Minimally Invasive Tumor Therapies*. Ed. by Christian Stroszczynski. Berlin, Heidelberg: Springer Berlin Heidelberg, 2006, pp. 3–12. ISBN: 978-3-540-28137-5. DOI: 10.1007/3-540-28137-1_1. URL: https://doi.org/10.1007/3-540-28137-1%5C_1.

[58] Beat Künzli, Paolo Abitabile, and Christoph Maurer. “Radiofrequency ablation of liver tumors: Actual limitations and potential solutions in the future”. In: *World journal of hepatology* 3 (Jan. 2011), pp. 8–14. DOI: 10.4254/wjh.v3.i1.8.

[59] J. L. Dinerman, R. D. Berger, and H. Calkins. “Temperature Monitoring During Radiofrequency Ablation”. In: *Journal of Cardiovascular Electrophysiology* 7.2 (1996), pp. 163–173. DOI: https://doi.org/10.1111/j.1540-8167.1996.tb00511.x. eprint: https://onlinelibrary.wiley.com/doi/pdf/10.1111/j.1540-8167.1996.tb00511.x. URL: https://onlinelibrary.wiley.com/doi/abs/10.1111/j.1540-8167.1996.tb00511.x.

[60] Riccardo Lencioni et al. “CHAPTER 11 - Biopsy technique and RF ablation, Radiofrequency”. In: *Clinical Ultrasound (Third Edition)*. Ed. by Paul L. Allan, Grant M. Baxter, and Michael J. Weston. Third Edition. Edinburgh: Churchill Livingstone, 2011, pp. 167–178. ISBN: 978-0-7020-3131-1. DOI: https://doi.org/10.1016/B978-0-7020-3131-1.00011-0. URL: https://www.sciencedirect.com/science/article/pii/B9780702031311000110.

[61] Olympus sergical technologies. *CelonLab Power*. 2018. URL: https://www.olympus-europa.com/medical/rmt/media/Content/Content-MSD/Documents/Brochures/CelonLab_Power_EN_20170215.pdf.

[62] Torben Lorentzen. “A cooled needle electrode for radiofrequency tissue ablation: Thermodynamic aspects of improved performance compared with conventional needle design”. In: *Academic Radiology* 3.7 (1996), pp. 556–563. ISSN: 1076-6332. DOI: https://doi.org/10.1016/S1076-6332(96)80219-4. URL: https://www.sciencedirect.com/science/article/pii/S1076633296802194.

[63] S. Nahum Goldberg et al. “Radiofrequency tissue ablation: Increased lesion diameter with a perfusion electrode”. In: *Academic Radiology* 3.8 (1996), pp. 636–644. ISSN: 1076-6332. DOI: https://doi.org/10.1016/S1076-6332(96)80188-7. URL: https://www.sciencedirect.com/science/article/pii/S1076633296801887.

[64] David S. K. Lu et al. “Effect of Vessel Size on Creation of Hepatic Radiofrequency Lesions in Pigs”. In: *American Journal of Roentgenology* 178.1 (2002). PMID: 11756085, pp. 47–51. DOI: 10.2214/ajr.178.1.1780047. eprint: https:

//doi.org/10.2214/ajr.178.1.1780047. URL: https://doi.org/10.2214/ajr.178.1.1780047.

[65] Krishna Pillai et al. “Heat Sink Effect on Tumor Ablation Characteristics as Observed in Monopolar Radiofrequency, Bipolar Radiofrequency, and Microwave, Using Ex Vivo Calf Liver Model”. In: *Medicine* 94 (Mar. 2015), e580. DOI: 10.1097/MD.0000000000000580.

[66] SN Goldberg et al. “Tissue ablation with radiofrequency using multiprobe arrays”. In: *Academic radiology* 2.8 (Aug. 1995), pp. 670–674. ISSN: 1076-6332. URL: http://europepmc.org/abstract/MED/9419623.

[67] S. N. Goldberg et al. “Large-volume tissue ablation with radio frequency by using a clustered, internally cooled electrode technique: laboratory and clinical experience in liver metastases., Radiofrequency”. In: *Radiology* 209.2 (1998). PMID: 9807561, pp. 371–379. DOI: 10.1148/radiology.209.2.9807561. eprint: https://doi.org/10.1148/radiology.209.2.9807561. URL: https://doi.org/10.1148/radiology.209.2.9807561.

[68] S N Goldberg et al. “Radio-frequency tissue ablation: effect of pharmacologic modulation of blood flow on coagulation diameter., Radiofrequency”. In: *Radiology* 209.3 (1998). PMID: 9844671, pp. 761–767. DOI: 10.1148/radiology.209.3.9844671. eprint: https://doi.org/10.1148/radiology.209.3.9844671. URL: https://doi.org/10.1148/radiology.209.3.9844671.

[69] S. Nahum Goldberg et al. “Percutaneous Radiofrequency Tissue Ablation: Does Perfusion-mediated Tissue Cooling Limit Coagulation Necrosis?” In: *Journal of Vascular and Interventional Radiology* 9.1 (1998), pp. 101–111. ISSN: 1051-0443. DOI: https://doi.org/10.1016/S1051-0443(98)70491-9. URL: https://www.sciencedirect.com/science/article/pii/S1051044398704919.

[70] S. Nahum Goldberg et al. “Percutaneous Radiofrequency Tissue Ablation: Optimization of Pulsed-Radiofrequency Technique to Increase Coagulation Necrosis”. In: *Journal of Vascular and Interventional Radiology* 10.7 (1999), pp. 907–916.

ISSN: 1051-0443. DOI: https://doi.org/10.1016/S1051-0443(99)70136-3. URL: https://www.sciencedirect.com/science/article/pii/S1051044399701363.

[71] Alice R. Gillams and William R. Lees. "CT Mapping of the Distribution of Saline During Radiofrequency Ablation with Perfusion Electrodes". In: *Cardio Vascular and Interventional Radiology* 28 (2005), pp. 476–480. URL: https://api.semanticscholar.org/CorpusID:6918967.

[72] Yamamoto S. Loh C. McWilliams J Lee E and S. Kee. "Image-Guided Tumor Ablation: Emerging Technologies and Future Directions". In: *Seminars in Interventional Radiology* 27.3 (2010), pp. 302–313. DOI: doi:10.1055/s-0030-1261789.

[73] St. Vincent's University Hospital Radiology. *Image of Radiofrequency Ablation of HCC*. http://www.svuhradiology.ie/case-study/radiofrequency-ablation-hcc/. Accessed: Nov 2018, Image Source. 2018.

[74] Christopher L. Brace et al. "Tissue Contraction Caused by Radiofrequency and Microwave Ablation: A Laboratory Study in Liver and Lung". In: *Journal of Vascular and Interventional Radiology* 21.8 (2010), pp. 1280–1286. ISSN: 1051-0443. DOI: https://doi.org/10.1016/j.jvir.2010.02.038. URL: https://www.sciencedirect.com/science/article/pii/S1051044310003088.

[75] Meghan G. Lubner et al. "Microwave Tumor Ablation: Mechanism of Action, Clinical Results, and Devices". In: *Journal of Vascular and Interventional Radiology* 21.8, Supplement (2010). Thermal Ablation 2010: At the Crossroads of Past Success, Current Goals, and Future Technology, S192–S203. ISSN: 1051-0443. DOI: https://doi.org/10.1016/j.jvir.2010.04.007. URL: https://www.sciencedirect.com/science/article/pii/S1051044310004112.

[76] KunalB Gala et al. "Microwave ablation: How we do it?" In: *Indian Journal of Radiology and Imaging* 30 (Apr. 2020), p. 206. DOI: 10.4103/ijri.IJRI_240_19.

[77] Nader Behdad James F. Sawicki Jacob D. Shea and Susan C. Hagness. “The impact of frequency on the performance of microwave ablation”. In: *International Journal of Hyperthermia* 33.1 (2017). PMID: 27443394, pp. 61–68. DOI: 10.1080/02656736.2016.1207254. eprint: https://doi.org/10.1080/02656736.2016.1207254. URL: https://doi.org/10.1080/02656736.2016.1207254.

[78] Caroline Simon, Damian Dupuy, and William Mayo-Smith. “Microwave Ablation: Principles and Applications1”. In: *Radiographics : a review publication of the Radiological Society of North America, Inc* 25 Suppl 1 (Nov. 2005), S69–83. DOI: 10.1148/rg.25si055501.

[79] Christopher L. Brace. “Microwave Ablation Technology: What Every User Should Know”. In: *Current Problems in Diagnostic Radiology* 38.2 (2009), pp. 61–67. ISSN: 0363-0188. DOI: https://doi.org/10.1067/j.cpradiol.2007.08.011. URL: https://www.sciencedirect.com/science/article/pii/S0363018807000618.

[80] Jason Chiang et al. “A Dual-Slot Microwave Antenna For More Spherical Ablation Zones: Ex Vivo And In Vivo Validation”. In: *Radiology* 268.2 (2013). PMID: 23579048, pp. 382–389. DOI: 10.1148/radiol.13122128. eprint: https://doi.org/10.1148/radiol.13122128. URL: https://doi.org/10.1148/radiol.13122128.

[81] Paola Saccomandi et al. “Temperature monitoring during microwave ablation in ex vivo porcine livers”. In: *European Journal of Surgical Oncology* 41 (Sept. 2015). DOI: 10.1016/j.ejso.2015.08.171.

[82] Deshan Yang et al. “Measurement and Analysis of Tissue Temperature During Microwave Liver Ablation”. In: *IEEE transactions on bio-medical engineering* 54 (Feb. 2007), pp. 150–5. DOI: 10.1109/TBME.2006.884647.

[83] L. S. Poulou et al. “Percutaneous microwave ablation vs radiofrequency ablation in the treatment of hepatocellular carcinoma”. In: *World journal of hepatology* 7.8 (2015), pp. 1054–1063. DOI: 10.4254/wjh.v7.i8.1054.

[84] Ahmad F. Atanesyan L. West K. Bhardwaj N Strickland A and D. Lloyd. "A comparative histological evaluation of the ablations produced by microwave, cryotherapy and radiofrequency in the liver". In: *Pathology* 41.2 (2009), pp. 168–172. DOI: 10.1080/00313020802579292.

[85] F. Izzo et al. "Radiofrequency Ablation and Microwave Ablation in Liver Tumors: An Update". In: *The Oncologist* 24.10 (2019), e990–e1005. DOI: 10.1634/theoncologist.2018-0337. URL: https://doi.org/10.1634/theoncologist.2018-0337.

[86] Soon Kyu Lee, Dong Jin Chung, and Se Hyun Cho. "A Real-World Comparative Study Of Microwave And Radiofrequency Ablation In Treatment-Naïve And Recurrent Hepatocellular Carcinoma". In: *Journal of Clinical Medicine* 11.2 (2022). ISSN: 2077-0383. DOI: 10.3390/jcm11020302. URL: https://www.mdpi.com/2077-0383/11/2/302.

[87] Laura Crocetti et al. "Microwave Ablation of Very-Early- and Early-Stage HCC: Efficacy Evaluation by Correlation with Histology after Liver Transplantation". In: *Cancers* 13.14 (2021), p. 3420. DOI: 10.3390/cancers13143420.

[88] Sevde Etoz and Christopher L. Brace. "Analysis of microwave ablation antenna optimization techniques". In: *International Journal of RF and Microwave Computer-Aided Engineering* 28.3 (2018), e21224. DOI: https://doi.org/10.1002/mmce.21224. eprint: https://onlinelibrary.wiley.com/doi/pdf/10.1002/mmce.21224. URL: https://onlinelibrary.wiley.com/doi/abs/10.1002/mmce.21224.

[89] Z. A. Ibitoye et al. "Optimization of dual slot antenna using floating metallic sleeve for microwave ablation". In: *Medical Engineering & Physics* 37.4 (2015), pp. 384–391. ISSN: 1350-4533. DOI: https://doi.org/10.1016/j.medengphy.2015.01.015. URL: https://www.sciencedirect.com/science/article/pii/S135045331500034X.

[90] Christopher L. Brace. "Dual-slot antennas for microwave tissue heating: Parametric design analysis and experimental validation". In: *Medical Physics* 38.7 (2011), pp. 4232–4240. DOI: https://doi.org/10.1118/1.3601019.

eprint: https://aapm.onlinelibrary.wiley.com/doi/pdf/10.1118/1.3601019. URL: https://aapm.onlinelibrary.wiley.com/doi/abs/10.1118/1.3601019.

[91] Nianan He et al. "Microwave Ablation: An Experimental Comparative Study On Internally Cooled Antenna Versus Non-Internally Cooled Antenna In Liver Models". In: *Academic Radiology* 17.7 (2010), pp. 894–899. ISSN: 1076-6332. DOI: https://doi.org/10.1016/j.acra.2010.03.005. URL: https://www.sciencedirect.com/science/article/pii/S1076633210001601.

[92] I. Longo et al. "A coaxial antenna with miniaturized choke for minimally invasive interstitial heating". In: *IEEE Trans Biomed Eng* 50.1 (2003), pp. 82–88. DOI: 10.1109/TBME.2002.807320.

[93] P. Keangin, P. Rattanadecho, and Teerapot Wessapan. "An analysis of heat transfer in liver tissue during microwave ablation using single and double slot antenna". In: *International Communications in Heat and Mass Transfer* 38 (July 2011), pp. 757–766. DOI: 10.1016/j.icheatmasstransfer.2011.03.027.

[94] John Gorman, Winston Tan, and John Abraham. "Numerical Simulation of Microwave Ablation in the Human Liver". In: *Processes* 10.2 (2022). ISSN: 2227-9717. URL: https://www.mdpi.com/2227-9717/10/2/361.

[95] Christian Rossmann and Dieter Haemmerich. "Review of Temperature Dependence of Thermal Properties, Dielectric Properties, and Perfusion of Biological Tissues at Hyperthermic and Ablation Temperatures". In: *Critical Reviews in Biomedical Engineering* 42 (May 2015). DOI: 10.1615/CritRevBiomedEng.2015012486.

[96] A Bhattacharya and R L Mahajan. "Temperature dependence of thermal conductivity of biological tissues". In: *Physiological Measurement* 24.3 (July 2003), p. 769. DOI: 10.1088/0967-3334/24/3/312. URL: https://dx.doi.org/10.1088/0967-3334/24/3/312.

[97] Piotr Gas. “The S11-Parameter Analysis of Multi-Slot Coaxial Antenna with Periodic Slots”. In: *Lecture Notes in Electrical Engineering* 452 (Jan. 2018), pp. 367–376. DOI: 10.1007/978-3-319-63949-9_24.

[98] COMSOL Inc. *COMSOL Multiphysics*. Available online: https://www.comsol.com/comsolmultiphysics (accessed on 20 February 2024). Burlington, MA, USA, 1986.

[99] CST AG. *CST STUDIO SUITE 2011*. Darmstadt, Germany, 2011.

[100] James R. Baker-Jarvis et al. “Characterization of tissue-equivalent materials for high-frequency applications (200 MHz to 20 GHz)”. In: (2010).

[101] Rakhesh Singh Kshetrimayum. “Mobile Phones: Bad for Your Health?” In: *IEEE Potentials* 27.2 (2008), pp. 18–20. DOI: 10.1109/MPOT.2008.919701.

[102] Punit Prakash. “Theoretical Modeling for Hepatic Microwave Ablation”. In: *The open biomedical engineering journal* 4 (Mar. 2010), pp. 27–38. DOI: 10.2174/1874120701004020027.

[103] Harry H. Pennes. “Analysis of Tissue and Arterial Blood Temperatures in the Resting Human Forearm”. In: *Journal of Applied Physiology* 1.2 (1948). PMID: 18887578, pp. 93–122. DOI: 10.1152/jappl.1948.1.2.93. eprint: https://doi.org/10.1152/jappl.1948.1.2.93. URL: https://doi.org/10.1152/jappl.1948.1.2.93.

[104] S. Labonte et al. “Monopole antennas for microwave catheter ablation”. In: *IEEE Transactions on Microwave Theory and Techniques* 44.10 (1996), pp. 1832–1840. DOI: 10.1109/22.539941.

[105] Sundeep Singh, Ramjee Repaka, and Ahmed Al-Jumaily. “Sensitivity analysis of critical parameters affecting the efficacy of microwave ablation using Taguchi method”. In: *International Journal of RF and Microwave Computer-Aided Engineering* 29.4 (2019), e21581. DOI: https://doi.org/10.1002/mmce.21581. eprint: https://onlinelibrary.wiley.com/doi/pdf/10.1002/mmce.21581. URL: https://onlinelibrary.wiley.com/doi/abs/10.1002/mmce.21581.

[106] Deshan Yang et al. “A floating sleeve antenna yields localized hepatic microwave ablation”. In: *IEEE Transactions on Biomedical Engineering* 53.3 (2006), pp. 533–537. DOI: 10.1109/TBME.2005.869794.

[107] Punit Prakash Mark C. Converse David M. Mahvi Ann P O’Rourke Dieter Haemmerich and John G. Webster. “Current status of liver tumor ablation devices, Radiofrequency”. In: *Expert Review of Medical Devices* 4.4 (2007). PMID: 17605688, pp. 523–537. DOI: 10.1586/17434440.4.4.523. eprint: https://doi.org/10.1586/17434440.4.4.523. URL: https://doi.org/10.1586/17434440.4.4.523.

[108] Olumuyiwa Adewumi, Okechukwu Agbasi, and Oluwanifesii Fatile. “Effect of Water-Cooled Loop Monopole Antenna on Microwave Ablation Efficiency”. In: *Mehmet Akif Ersoy University Journal of Health Sciences Institute* 7 (2019), pp. 41–54. DOI: 10.24998/maeusabed.590456.

[109] A. Z. Ibitoye et al. “Analysis of efficiency of different antennas for microwave ablation using simulation and experimental methods”. In: *Egyptian Journal of Basic and Applied Sciences* 5.1 (2018), pp. 24–30. ISSN: 2314-808X. DOI: https://doi.org/10.1016/j.ejbas.2018.01.005. URL: https://www.sciencedirect.com/science/article/pii/S2314808X17305742.

[110] Sabiha Binte Aziz et al. “Effect of the antenna slot numbers and position on the performance of microwave ablation”. In: *Medicine in Novel Technology and Devices* 20 (2023), p. 100271. ISSN: 2590-0935. DOI: https://doi.org/10.1016/j.medntd.2023.100271. URL: https://www.sciencedirect.com/science/article/pii/S2590093523000668.

[111] H. Acikgoz and I. Turer. “A Novel Microwave Coaxial Slot Antenna for Liver Tumor Ablation”. In: *Advanced Electromagnetics* 3.1 (2014), pp. 20–25. DOI: 10.7716/aem.v3i1.192. URL: https://aemjournal.org/index.php/AEM/article/view/192.

[112] Surita Maini. “Design optimization of tapered cap floating sleeve antenna for interstitial microwave ablation for liver tumor”. In: Jan. 2016, pp. 305–308. DOI: 10.1109/ICCE.2016.7430623.

[113] Vlad Neagu. “A study of microwave ablation antenna optimization”. In: *2017 E-Health and Bioengineering Conference (EHB)*. 2017, pp. 41–44. DOI: 10.1109/EHB.2017.7995356.

[114] Hung Luyen, Susan C. Hagness, and Nader Behdad. “Reduced-Diameter Designs of Coax-Fed Microwave Ablation Antennas Equipped With Baluns”. In: *IEEE Antennas and Wireless Propagation Letters* 16 (2017), pp. 1385–1388. DOI: 10.1109/LAWP.2016.2637874.

[115] Surita Maini and Dilip Singh Shekhawat. “Analysis of Copper Tube Sleeve Coaxial Spiral Antenna for Interstitial Hepatic Microwave Ablation”. In: *2018 Eighth International Conference on Information Science and Technology (ICIST)*. 2018, pp. 31–34. DOI: 10.1109/ICIST.2018.8426131.

[116] Erica M. Knavel et al. “High-Powered Gas-Cooled Microwave Ablation: Shaft Cooling Creates an Effective Stick Function Without Altering the Ablation Zone”. In: *American Journal of Roentgenology* 198.3 (2012), W260–W265. DOI: 10.2214/AJR.11.6503.

[117] Jeremy C. Horn et al. “Percutaneous Microwave Ablation of Renal Tumors Using a Gas-Cooled 2.4-GHz Probe: Technique and Initial Results”. In: *Journal of Vascular and Interventional Radiology* 25.3 (2014), pp. 448–453. ISSN: 1051-0443. DOI: https://doi.org/10.1016/j.jvir.2013.10.029. URL: https://www.sciencedirect.com/science/article/pii/S1051044313015510.

[118] Yang X. Nan Q. Xiao J. Liu Y. and L. Li. “Phantom experimental study on microwave ablation with a water-cooled antenna”. In: *International Journal of Hyperthermia* 23.4 (2007). PMID: 17558737, pp. 381–386. DOI: 10.1080/02656730701397841. eprint: https://doi.org/10.1080/02656730701397841. URL: https://doi.org/10.1080/02656730701397841.

[119] Ming Kuang et al. “Liver Cancer: Increased Microwave Delivery to Ablation Zone with Cooled-Shaft Antenna—Experimental and Clinical Studies”. In: *Radiology* 242.3 (2007). PMID: 17229876, pp. 914–924. DOI: 10.1148/

radiol.2423052028. eprint: https://doi.org/10.1148/radiol.2423052028. URL: https://doi.org/10.1148/radiol.2423052028.

[120] Oscar Maximilian Mader et al. "Comparative study evaluating the efficiency of cooled and uncooled single-treatment MWA in thyroid nodules after a 3-month follow up". In: *European Journal of Radiology Open* 4 (2017), pp. 4–8. ISSN: 2352-0477. DOI: https://doi.org/10.1016/j.ejro.2017.01.004. URL: https://www.sciencedirect.com/science/article/pii/S2352047717300047.

[121] M. Cavagnaro et al. "A minimally invasive antenna for microwave ablation therapies: design, performances, and experimental assessment". In: *IEEE transactions on bio-medical engineering* 58.4 (2011), pp. 949–959. DOI: 10.1109/TBME.2010.2099657.

[122] Qun Nan et al. "Numerical Simulation on Microwave Ablation with a Water-Cooled Antenna". In: *2007 1st International Conference on Bioinformatics and Biomedical Engineering*. 2007, pp. 698–701. DOI: 10.1109/ICBBE.2007.182.

[123] Liang Li Yulin Lu Qun Nan and Youjun Liu. "Numerical study on thermal field of microwave ablation with water-cooled antenna". In: *International Journal of Hyperthermia* 25.2 (2009), pp. 108–115. DOI: 10.1080/02656730802587720. eprint: https://doi.org/10.1080/02656730802587720. URL: https://doi.org/10.1080/02656730802587720.

[124] Marta Cavagnaro, Rosanna Pinto, and Vanni Lopresto. "Numerical models to evaluate the temperature increase induced by ex vivo microwave thermal ablation". In: *Physics in medicine and biology* 60 (Mar. 2015), pp. 3287–3311. DOI: 10.1088/0031-9155/60/8/3287.

[125] Hojjatollah Fallahi et al. "Microwave antennas for thermal ablation of benign adrenal adenomas". In: *Biomedical Physics & Engineering Express* 5.2 (Feb. 2019), p. 025044. DOI: 10.1088/2057-1976/ab068b. URL: https://dx.doi.org/10.1088/2057-1976/ab068b.

[126] Deshan Yang et al. “Expanding the Bioheat Equation to Include Tissue Internal Water Evaporation During Heating”. In: *IEEE Transactions on Biomedical Engineering* 54.8 (2007), pp. 1382–1388. DOI: 10.1109/TBME.2007.890740.

[127] Marija Radmilović-Radjenović et al. “An Analysis of Microwave Ablation Parameters for Treatment of Liver Tumors from the 3D-IRCADb-01 Database”. In: *Biomedicines* 10.7 (2022), p. 1569. DOI: 10.3390/biomedicines10071569. URL: https://doi.org/10.3390/biomedicines10071569.

[128] M. S. Wall et al. “Thermal modification of collagen”. In: *Journal of Shoulder and Elbow Surgery* 8.4 (1999), pp. 339–344. DOI: 10.1016/s1058-2746(99)90157-x. URL: https://doi.org/10.1016/s1058-2746(99)90157-x.

[129] Dong Liu and Christopher L Brace. “CT imaging during microwave ablation: analysis of spatial and temporal tissue contraction”. In: *Medical physics* 41.11 (2014), p. 113303. DOI: https://doi.org/10.1118/1.4897381.

[130] Vanni Lopresto Rosanna Pinto Simone Cassarino Nevio Tosoratti S. Nahum Goldberg Claudio Amabile Laura Farina and Marta Cavagnaro. “Tissue shrinkage in microwave ablation of liver: an ex vivo predictive model”. In: *International Journal of Hyperthermia* 33.1 (2017). PMID: 27439333, pp. 101–109. DOI: 10.1080/02656736.2016.1208292. URL: https://doi.org/10.1080/02656736.2016.1208292.

[131] Dong Liu and Christopher Brace. “Evaluation of Tissue Deformation during Radiofrequency and Microwave Ablation Procedures: Influence of Output Energy Delivery”. In: *Medical Physics* 46 (July 2019). DOI: 10.1002/mp.13688.

[132] Claudio Tucci et al. “Pennes’ bioheat equation vs. porous media approach in computer modeling of radiofrequency tumor ablation”. In: *Scientific Reports* 11 (Mar. 2021). DOI: 10.1038/s41598-021-84546-6.

[133] Claudio Tucci et al. “Mathematical modeling of microwave liver ablation with a variable-porosity medium approach”. In: *Computer Methods and Programs in Biomedicine* 214 (2022), p. 106569. ISSN: 0169-2607. DOI: https://doi.org/

10.1016/j.cmpb.2021.106569. URL: https://www.sciencedirect.com/science/article/pii/S016926072100643X.

[134] Pornthip Keangin and Phadungsak Rattanadecho. "A numerical investigation of microwave ablation on porous liver tissue". In: *Advances in Mechanical Engineering* 10.8 (2018), p. 1687814017734133. DOI: 10.1177/1687814017734133. eprint: https://doi.org/10.1177/1687814017734133. URL: https://doi.org/10.1177/1687814017734133.

[135] John Bertram et al. "Antenna design for microwave hepatic ablation using an axisymmetric electromagnetic model". In: *Biomedical engineering online* 5 (Feb. 2006), p. 15. DOI: 10.1186/1475-925X-5-15.

[136] Prakash Punit et al. "An Optimal Sliding Choke Antenna For Hepatic Microwave Ablation". In: *IEEE Transactions on Biomedical Engineering* 56.10 (2009), pp. 2470–2476. DOI: 10.1109/TBME.2009.2025264.

[137] S. Curto et al. "Microwave ablation at 915 MHz vs 2.45 GHz: A theoretical and experimental investigation". In: *Medical Physics* 42.11 (2015), pp. 6152–6161. DOI: 10.1118/1.4931959. URL: https://doi.org/10.1118/1.4931959.

[138] Olumide Towoju et al. "Investigation of Influence of Coaxial Antenna Slot Positioning on Thermal Efficiency in Microwave Ablation using COMSOL". In: *Journal of Physics: Conference Series* 1378.3 (Dec. 2019), p. 032066. DOI: 10.1088/1742-6596/1378/3/032066. URL: https://dx.doi.org/10.1088/1742-6596/1378/3/032066.

[139] Amira S. Ashour et al. "Optimal Localization of a Novel Shifted 1T-Ring Based Microwave Ablation Probe in Hepatocellular Carcinoma". In: *IEEE Transactions on Biomedical Engineering* PP (June 2020), pp. 1–1. DOI: 10.1109/TBME.2020.3006010.

[140] Fernando Burdío Enrique Berjano Punit Prakash Aleksandar Radosevic Diego Prieto and Macarena Trujillo. "Short pulsed microwave ablation: computer modeling and ex vivo experiments". In: *International Journal of Hyperthermia* 38.1 (2021). PMID: 33719808, pp. 409–420. DOI: 10.1080/02656736.

2021.1894358. eprint: https://doi.org/10.1080/02656736.2021.1894358. URL: https://doi.org/10.1080/02656736.2021.1894358.

[141] Brogan T. McWilliams et al. "A Directional Interstitial Antenna For Microwave Tissue Ablation: Theoretical And Experimental Investigation". In: *IEEE Transactions on Biomedical Engineering* 62.9 (2015), pp. 2144–2150. DOI: 10.1109/TBME.2015.2413672.

[142] Dale Kernot et al. "Transient changes during microwave ablation simulation : a comparative shape analysis". In: *Biomechanics and Modeling in Mechanobiology* 22 (2022), pp. 271–280. URL: https://api.semanticscholar.org/CorpusID:253119269.

[143] L.F. Demkowicz. *Mathematical Theory of Finite Elements*. Computational science and engineering. Society for Industrial and Applied Mathematics, 2023. ISBN: 9781611977738. URL: https://books.google.co.uk/books?id=ODfZEAAAQBAJ.

[144] Zheng Lou and Jian-Ming Jin. "An accurate waveguide port boundary condition for the time-domain finite-element method". In: vol. 53. Feb. 2005, 117–120 vol. 1B. ISBN: 0-7803-8883-6. DOI: 10.1109/APS.2005.1551498.

[145] B. Chaber, R. Szmurło, and J. Starzyński. "Solution of the complex-valued Helmholtz equation using a dedicated finite element solver". In: *Przeglad Elektrotechniczny* 93.3 (Mar. 2017), pp. 171–174. DOI: 10.15199/48.2017.03.40.

[146] "Antenna Source Modeling and Parameter Calculation". In: *Finite Element Analysis of Antennas and Arrays*. John Wiley and Sons, Ltd, 2008. Chap. 5, pp. 147–186. ISBN: 9780470409732. DOI: https://doi.org/10.1002/9780470409732.ch5. eprint: https://onlinelibrary.wiley.com/doi/pdf/10.1002/9780470409732.ch5. URL: https://onlinelibrary.wiley.com/doi/abs/10.1002/9780470409732.ch5.

[147] Vanni Lopresto, Rosanna Pinto, and Marta Cavagnaro. "Experimental characterisation of the thermal lesion induced by microwave ablation". In: *International*

journal of hyperthermia : the official journal of European Society for Hyperthermic Oncology, North American Hyperthermia Group 30 (Mar. 2014), pp. 110–8. DOI: 10.3109/02656736.2013.879744.

[148] J. Schöberl. *C++11 Implementation of Finite Elements in NGSolve*. Technical Report ASC Report 30/2014, Vienna, Austria: Institute for Analysis and Scientific Computing, Vienna University of Technology. 2014.

[149] Igor Baratta et al. *DOLFINx: The next generation FEniCS problem solving environment*. Dec. 2023. DOI: 10.5281/zenodo.10447665.

[150] Christophe Geuzaine and Jean-François Remacle. "Gmsh: A 3-D finite element mesh generator with built-in pre- and post-processing facilities". In: *International Journal for Numerical Methods in Engineering* 79.11 (2009), pp. 1309–1331. DOI: https://doi.org/10.1002/nme.2579. eprint: https://onlinelibrary.wiley.com/doi/pdf/10.1002/nme.2579. URL: https://onlinelibrary.wiley.com/doi/abs/10.1002/nme.2579.

[151] COMSOL AB. *Microwave Heating of a Cancer Tumor*. Accessed: January 2019. URL: https://www.comsol.com/model/microwave-heating-of-a-cancer-tumor-30.

[152] Ping Liang et al. "Malignant Liver Tumors: Treatment with Percutaneous Microwave Ablation—Complications among Cohort of 1136 Patients". In: *Radiology* 251.3 (2009), pp. 933–940. DOI: 10.1148/radiol.2513081740.

[153] Nour-Eldin A. Nour-Eldin Benjamin Kaltenbach Boris Bodelle Julian L. Wichmann Hanns Ackermann Thomas J. Vogl Lajos M. Basten and Nagy N. N. Naguib. "Evaluation of microwave ablation of liver malignancy with enabled constant spatial energy control to achieve a predictable spherical ablation zone". In: *International Journal of Hyperthermia* 34.4 (2018). PMID: 28774210, pp. 492–500. DOI: 10.1080/02656736.2017.1358408. eprint: https://doi.org/10.1080/02656736.2017.1358408. URL: https://doi.org/10.1080/02656736.2017.1358408.

[154] COMSOL. *RF Module User's Guide*. Version 5.6. Accessed: 2023-04-29. COMSOL AB. 2020. URL: https://doc.comsol.com/5.5/doc/com.comsol.help.rf/rf_ug_theory.06.12.html.

[155] Punit Prakash et al. "Design optimization of a robust sleeve antenna for hepatic microwave ablation". In: *Physics in Medicine and Biology* 53.4 (Jan. 2008), p. 1057.

[156] B Trembley, T Ryan, and J Strohbehn. "Interstitial hyperthermia: physics, biology, and clinical aspects". In: *Hyperthermia and oncology* 3 (1992), pp. 11–98.

[157] Riadh Habash. *Bioeffects and Therapeutic Applications of Electromagnetic Energy*. Jan. 2008, p. 22. ISBN: 9781420062847. DOI: 10.1201/9781420062854.ch5.

[158] Frank M. White. *Fluid Mechanics*. 8th ed. McGraw-Hill Education, 2016. ISBN: 978-0073398273.

[159] Vincenza Portosi et al. "Low-Cost Mini-Invasive Microwave Needle Applicator for Cancer Thermal Ablation: Feasibility Investigation". In: *IEEE Sensors Journal* 21.13 (2021), pp. 14027–14034. DOI: 10.1109/JSEN.2021.3060499.

[160] David O'Neill et al. "A Three-State Mathematical Model of Hyperthermic Cell Death". In: *Annals of biomedical engineering* 39 (Oct. 2010), pp. 570–9. DOI: 10.1007/s10439-010-0177-1.

[161] Pegah Faridi et al. "Experimental assessment of microwave ablation computational modeling with MR thermometry". In: *Medical Physics* 47.9 (2020), pp. 3777–3788. DOI: https://doi.org/10.1002/mp.14318. eprint: https://aapm.onlinelibrary.wiley.com/doi/pdf/10.1002/mp.14318. URL: https://aapm.onlinelibrary.wiley.com/doi/abs/10.1002/mp.14318.

Appendices

Bespoke software document

What is normally used for microwave ablation modelling? - COMSOL

Current literature overwhelmingly uses COMSOL Multiphysics as a tool for conducting modelling of microwave ablation. COMSOL is a simulation platform with multiple modules for various physics, including electromagnetics, structural mechanics, fluid flow and heat transfer. Within this platform, these physics-based models are readily coupled for multiphysics finite element modelling. In the specific case of microwave ablation modelling, both the heat transfer and RF module products must be acquired, in addition to the basic license...

What are the advantages and disadvantages?

Although these commercial software provide a intuitive interface and fast setup, provided by demonstration for MWA simulation works, this comes at the financial cost which limits its accessibility. In addition, although setup can be easy by following the tutorial, if any alterations to the fundamental physics is required then a understanding of the governing equations and formulation is also required...

Why are we using an alternative?

With these drawbacks in mind, this part of the project aimed to create a framework with foundations on open source software, capable of executing simulations comparable to those on the commercial standards. This framework should also be simple to use, with formulations embedded into the code such that the user can select various ablation modes to model without a mathematical understanding of the formulation being necessary.

what do we use to build this?

The fundamental building blocks of such a framework will require a geometry creation and meshing tool for generation of labelled mesh objects that are appropriate for finite element analysis. this job is given to GMSH, an open source 3D finite element mesh generator. More specifically, we utilise the geometry and mesh modules within GMSH

and interact with the platform through GMSH's own scripting language using .geo files. This allows full details of geometry and mesh shape to be stored and readily edited before calling GMSH to execute the instructions, yielding a .msh file that is compatible with the rest of the FEM methods used later.

For computing the PDEs defining this problem, the versatile multiphysics solver NG-Solve is chosen. This finite element software can readily compute equations describing fluid dynamics, electromagnetics and heat transfer, along with a broad range of mathematical techniques for FEM such as higher order elements and choices of element type. Models are scripted in python which makes this solver flexible and easy to integrate with GMSH. Taking these two fundamentals, a python based user interface could then be built to house the solving framework. PYQT5 is an attractive library for graphical user interface creation because of its simplistic designer interface that allows a fast and easy way to create the basic layout of your GUI and convert that design to python code for fictionalisation.

Functionality

Emphasis on flexibility of application is made when designing this GUI, if thorough investigations are to be made then the ability to batch simulate multiple probe designs with various geometry and input variable settings will be a powerful function.

In total there are over 25 parameters and to be set for initialising the ablation model, and a further 10 defining

A Graphical user interface

Upon running the interface code, a graphical user interface opens that can guide the user through setting up a simulation. The first page handles fundamental parameters for the probe operation: the frequency and power, in addition to a toggle for simulating either a static electromagnetic solution or a full ablation with the transient coupling of physical models. If a ablation is to be simulated, the ablation time and temporal step size in for the transient computation can be specified, there are also options to add variable time step sizes at different stages of ablation. Post ablation modelling, which continues the computation for a time after power to the probe has been haulted, is also possible, with variable time stepping functionality.

Although the type of element used for the FEM analysis are fixed, the polynomial order of those elements can be altered within the FEM parameters box, as seen in Fig A.1. here the H(Curl) and H1 orders refer to the elements used in electromagnetic and bioheat calculations respectively. since the meshes are generated in a later stage, it is possible to alter the specified element size at this stage too.
Dielectric properties for the materials within the computed domains are largely pre-built into the code as their values are well known standard, however the literature suggests that the dielectric properties of the catheter and dielectric material within the coaxial structure may vary in order to achieve a desirable impedance matching. Therefore, the option to manually define these property values is given on this page.

One form of post processing built into this framework is the shape analysis previously mentioned in the third chapter. threshold values for temperature, SAR and Cell death fraction can be provided so that isocontours can be created through the results and several shape metrics can be drawn. This part does require a matlab engine and contrasts the largely open source nature of the platform to this point. A powerful tool for rapidly setting up investigations is contained within the Variable iterator box in Fig A.1, this function effectively allows a sweep of different values for a specific variable to be simulated in a single batch. Selection is made through the Run iterator check box, specific variables of interest are visible in a drop down menu before selecting an upper

and lower limit to the range that is of interest, along with the number of steps desired between these bounds.

The final part of this page involves storing and loading of all the input user inputs. In order to save time and to eliminate human error if repeat simulations are to be made, a .xlsx file template is created where all inputs can be stored, we will call this an instruction file and is shown in figs. A.2 and A.3. This instruction file can be used to save all values input through the user interface, checking the ”Save sim settings?” box will create a instruction file with the name specified in ”Save setting file name:” bar, and fill in all entries given manually through the GUI upon the completion of the simulation. Alternatively, if an instruction file already exists and is filled completely with the desired information then the ”Use sim input file” checkbox can be filled, which triggers the GUI to automatically load an instruction file with name input in the ”Input setting file name:” bar.
Within this instruction file, inputs for multiple simulations can be stored in different worksheets. Each sheet contains a full set values to be loaded to into GUI and run an independent simulation. To enable these simulations to be ran sequentially with one call on the instruction file, a ”Automate” variable is added.

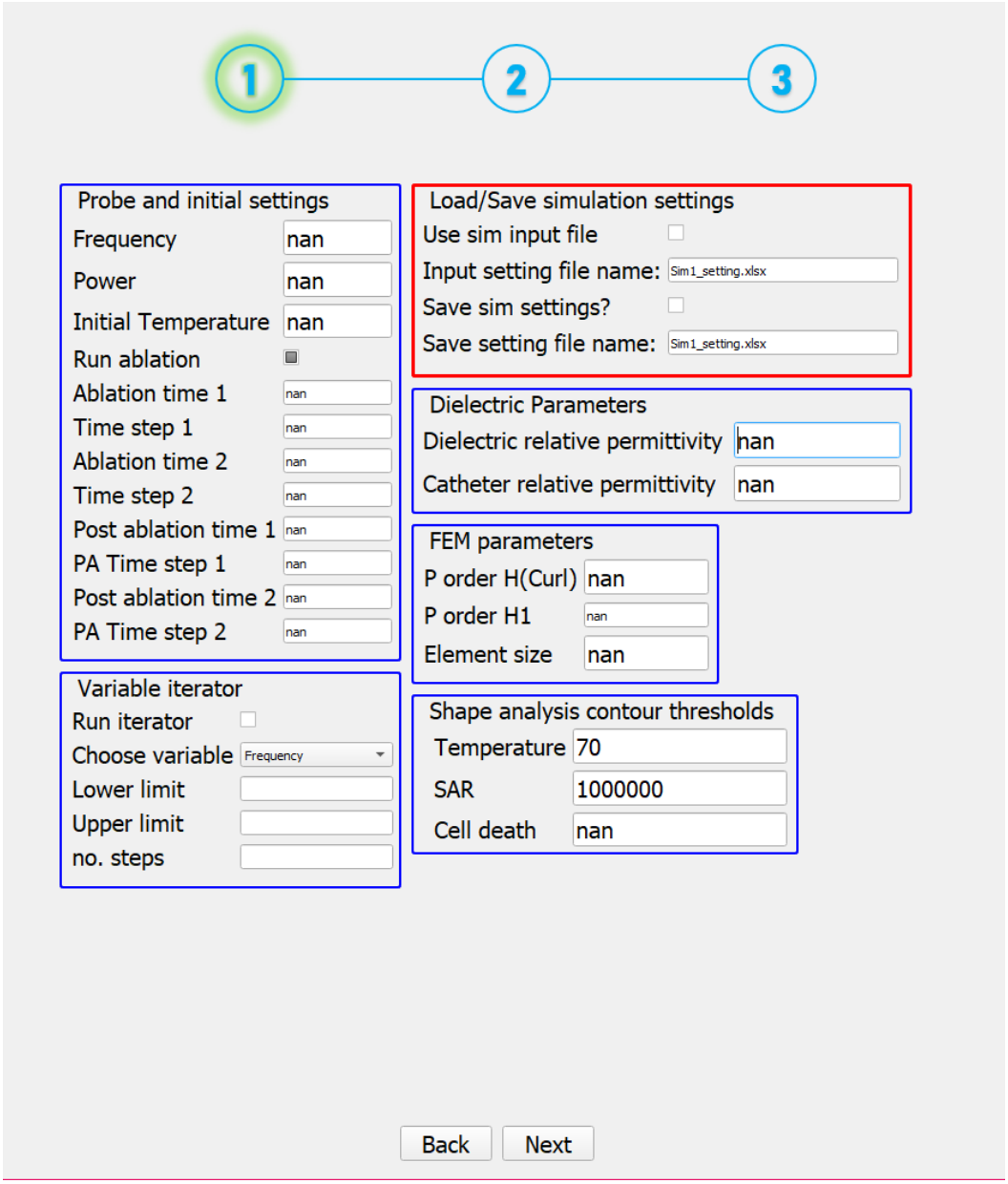

Figure A.1: First page of the GUI, enabling manual input of parameter values for initialising the ablation model. Within this page lies the option to load a pre existing settings file, or save the manually input values to create a new settings file.

Upon pressing the ”Next” button, Page 2 displays the geometric settings. Firstly the appropriate probe can be selected from the ”Choose a probe:” drop down menu, the full library of probes includes a single slotted probe, Monopole probe, Dual slotted probe, Single slotted probe with sleeve, Dual slotted probe with sleeve, and a internally cooled monopole probe. As visible in figs. A.4 and A.5, the selected probe schematic appears with full annotations of the geometric parameters that are possible to edit.

	Variable	Value
0	Automate	TRUE
1	comboBox	Cooled probe
2	Run_ablation_check	TRUE
3	Run_iterator_check	TRUE
4	Run_Dimension_iterator_check	FALSE
5	Frequency_input	2.45e9
6	Power_input	60
7	Temperature_input	37
8	Time_step_1_input	0.2
9	Ablation_time_1_input	150
10	Time_step_2_input	0
11	Ablation_time_2_input	0
12	PA_Time_step_1_input	0
13	Post_ablation_time_1_input	0
14	PA_Time_step_2_input	0
15	Post_ablation_time_2_input	0
16	P_order_Hcurl_input	3
17	P_order_H1_input	5
18	Element_size_input	0.0001
19	Dielectric_r_permittivity_input	2.03
20	Catheter_r_permittivity_input	2.6
21	Choose_Dimension_iteration_variable	
22	Choose_iteration_variable	Coolant_Temp
23	Iteration_lower_limit_input	-1.50E+01
24	Iteration_upper_limit_input	1.00E+00
25	Number_iteration_steps_input	3
26	Temperature_threshold_input	50
27	SAR_threshold_input	1000000
28	Cell_death_threshold_input	0.75
29	R1_input	0.000135
30	R2_input	0.000335
31	R3_input	0.00046
32	R4_input	0.0015
33	L1_input	0.003
34	L2_input	0.06
35	L3_input	0.08
36	L4_input	0.04
37	L5_input	
38	W1_input	0.001
39	L6_input	
40	L7_input	
41	R5_input	
42	T1_input	
43	L8_input	
44	L9_input	
45	L10_input	0.012

Figure A.2: Instruction file layout containing general settings in greys and probe geometric parameters in the blues.

Some of these parameters are common across all probes such as those defining the internal coaxial shape and surrounding catheter, these are: Dielectric inner radius (R1), Dielectric outer radius (R2), Conductor outer radius (R3), Catheter radius (R4). Probe position and tissue bounds are also generic for all designs: Probe depth (L2), Tissue height (L3), Tissue width (L4). Probe specific parameters include: Sleeve inner radius (R5), Slot distance from the end of probe (L1), Slot seperation distance (L5),

46	Path_to_folder_input	D:\NG_folder/UI_results
47	File_name_template_input	Cooled2_VarT_60W
48	Save_log_check	TRUE
49	Antenna_characteristics_check	TRUE
50	FEM_settings_check	TRUE
51	Shape_analysis_check	FALSE
52	General_settings_check	TRUE
53	Reflection_coefficient_check	TRUE
54	Save_vtk_check	TRUE
55	Electrical_conductivity_check	TRUE
56	Electrical_field_check	TRUE
57	SAR_field_check	TRUE
58	Temperature_field_check	TRUE
59	Electrical_permittivity_check	TRUE
60	Alive_Cells_check	TRUE
61	Vulnerable_Cells_check	TRUE
62	Dead_Cells_check	TRUE
63	Total_Cells_check	TRUE

Figure A.3: The remainder of the instruction file, containing information on what data should be saved in vtk and log files, along with their location.

Outer conductor length (L6), Inner conductor length (L7), Sleeve center position (L8), Sleeve lenght (L9), Coolant U position(L10), Slot width (W1), and Sleeve thickness (T1). These are summarised in Table A.1.

Probe	Parameter									
	R5	L1	L5	L6	L7	L8	L9	L10	W1	T1
Single slot		✓							✓	
Monopole				✓	✓					
Dual slot		✓	✓						✓	
Single slot sleeve	✓	✓				✓	✓		✓	✓
Dual slot sleeve	✓	✓	✓			✓	✓		✓	✓
Cooled single slot		✓						✓	✓	

Table A.1: Probe specific geometric parameters

To aid investigations into geometric changes to ablation, a dimension sweep functionality is added into this page. Similar to the variable sweep seen on the previous page, if the check box is selected then a particular geometric parameter can be picked from the drop down menu before defining upper and lower limits and a number of steps to be taken to bridge between the two. If selected, the chosen parameter will be iteratively changed in each simulation whilst the rest of the geometry remains fixed, allowing a

sequence of simulations to be ran quickly and easily.

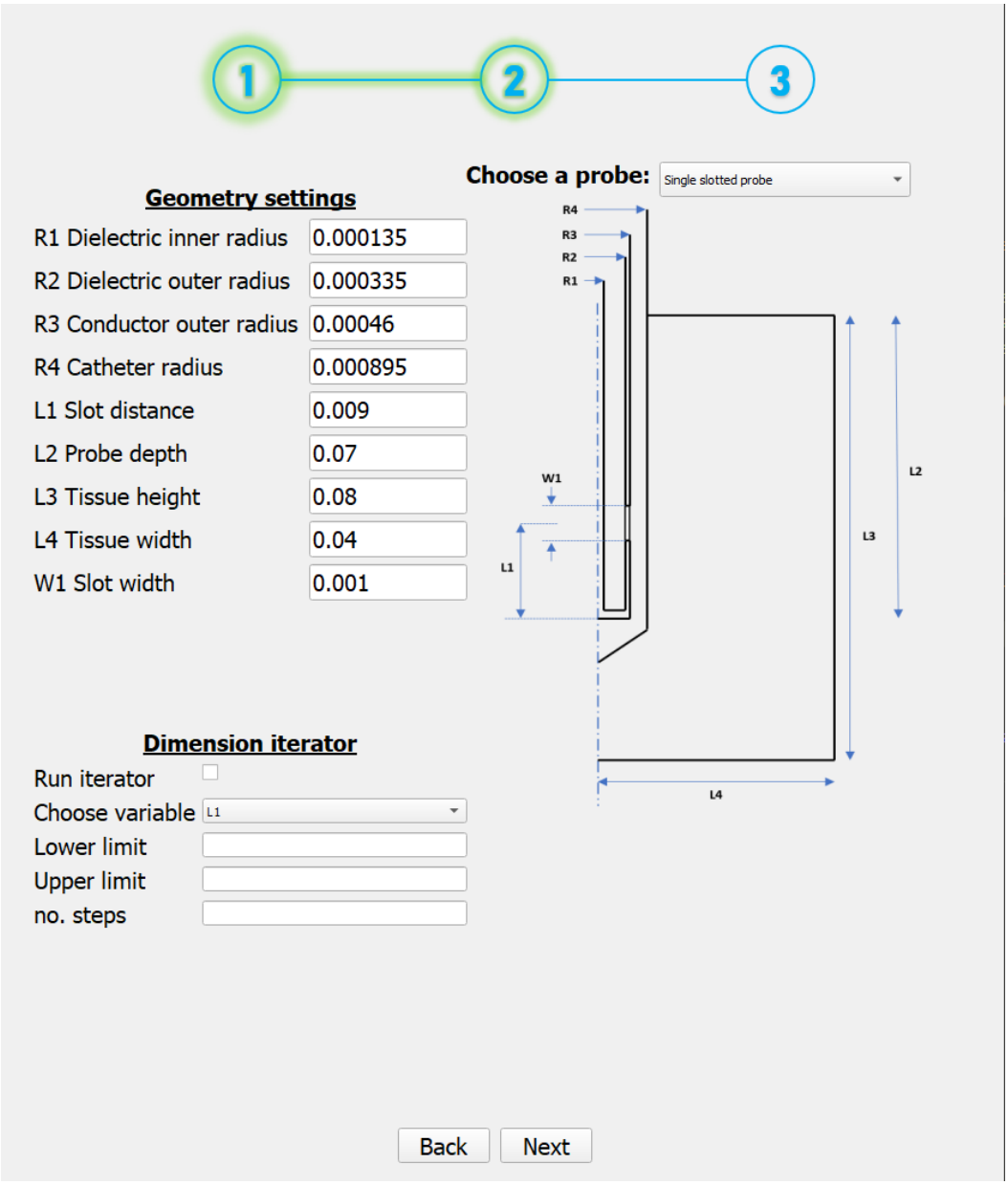

Figure A.4: Page 2 on the GUI with Single slotted probe selected from the library.

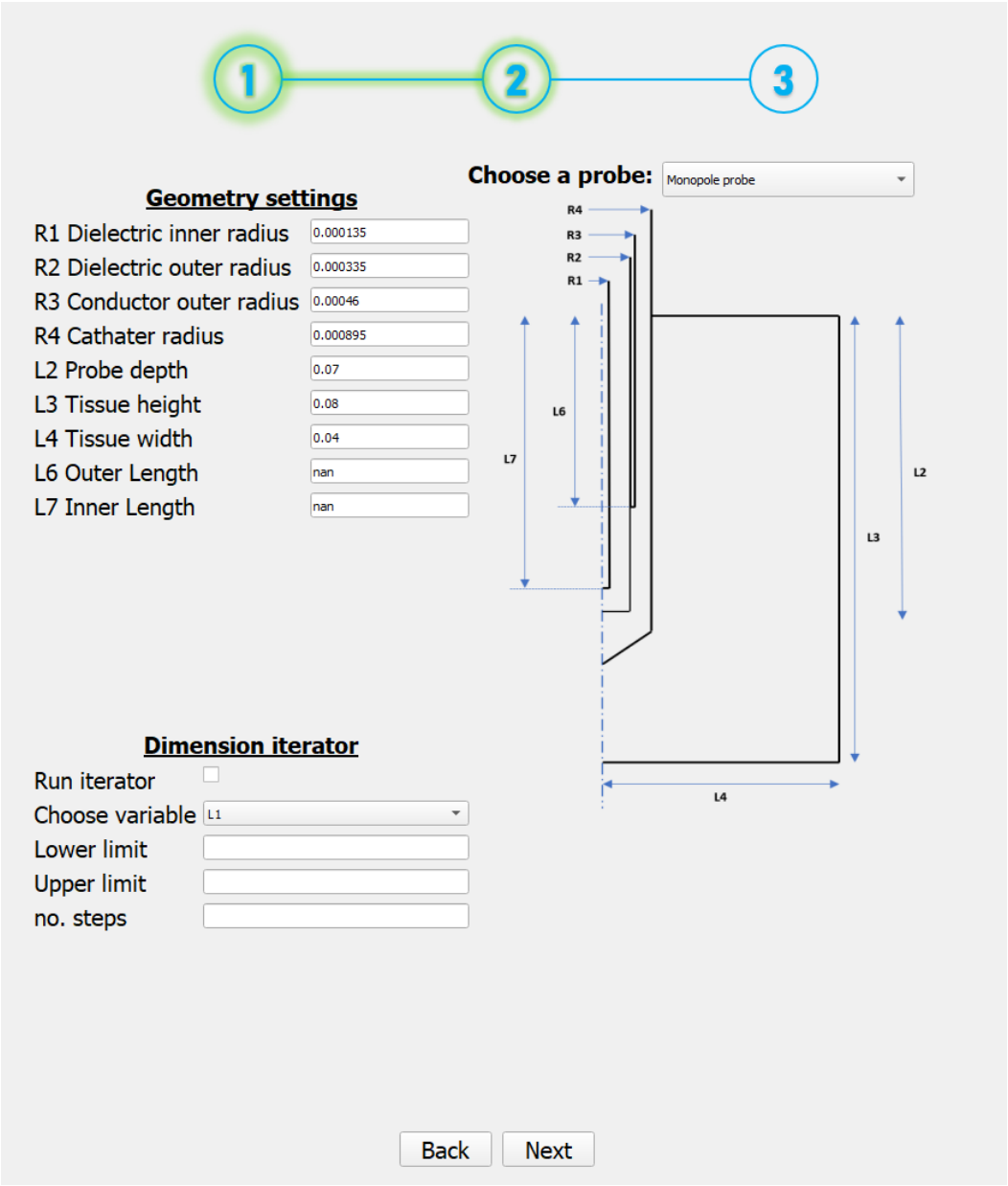

Figure A.5: Page 2 on the GUI with Monopole probe selected from the library.

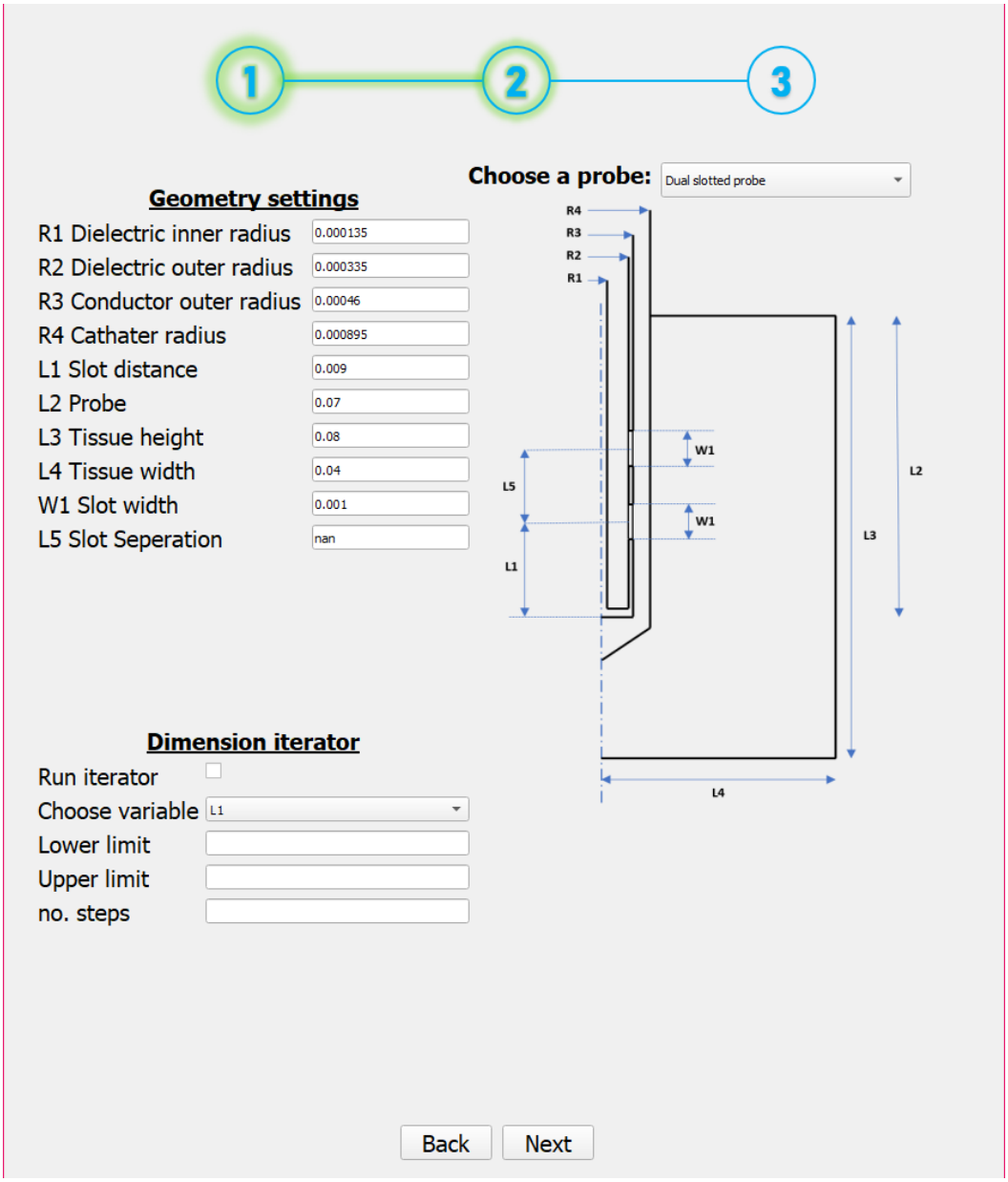

Figure A.6: Page 2 on the GUI with Dual slotted probe selected from the library.

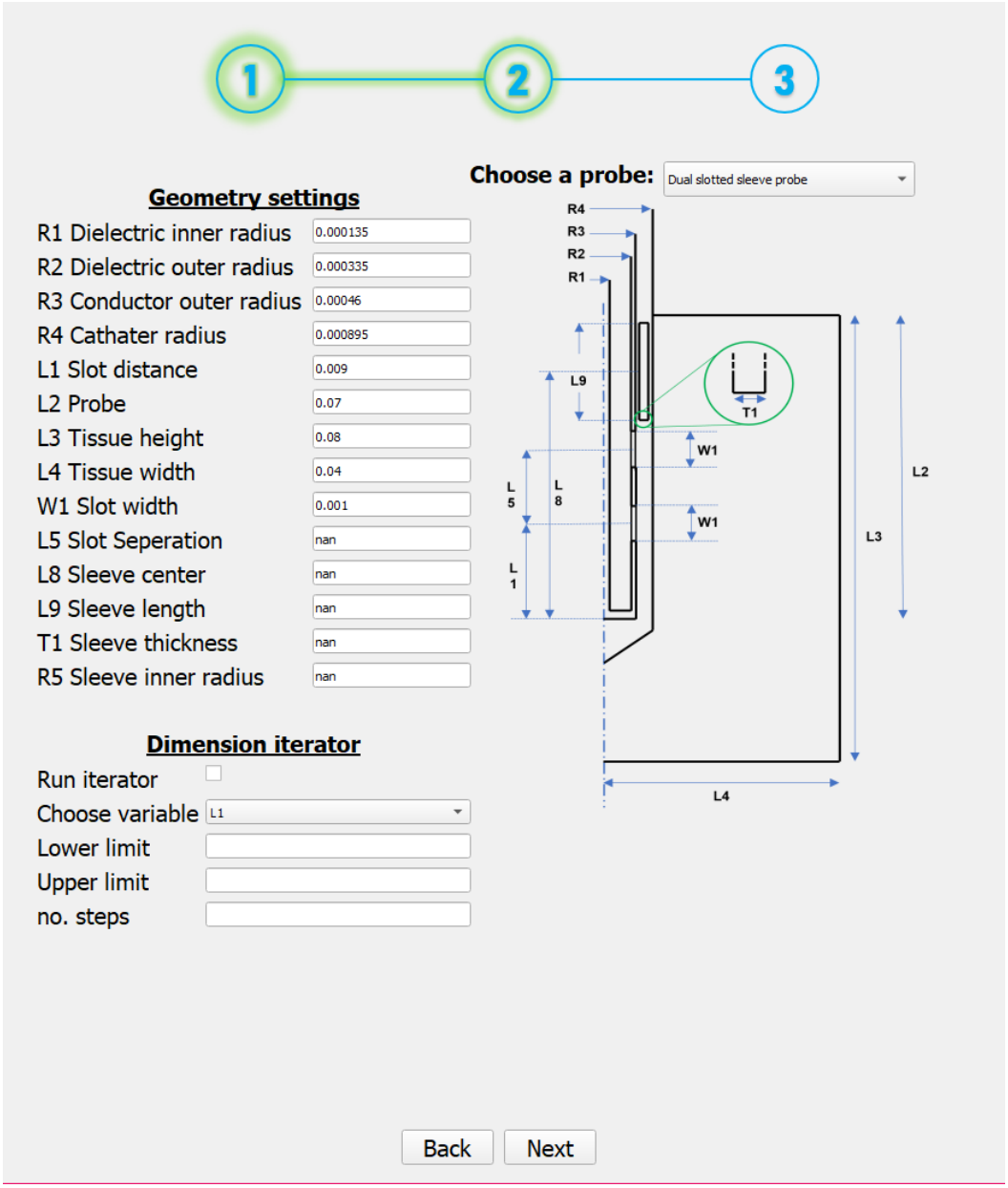

Figure A.7: Page 2 on the GUI with Dual slotted probe with sleeve selected from the library.

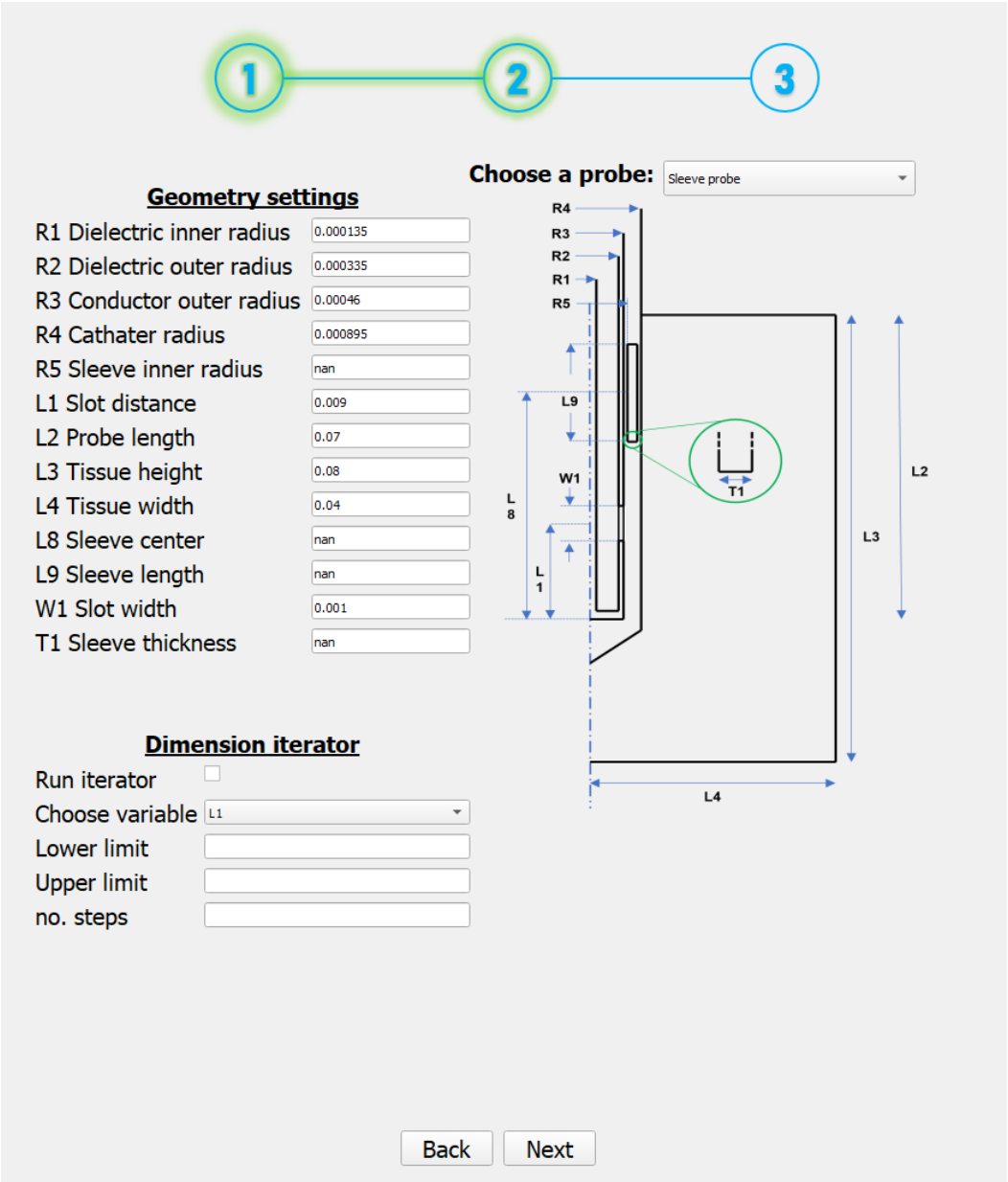

Figure A.8: Page 2 on the GUI with Single slotted probe with sleeve selected from the library.

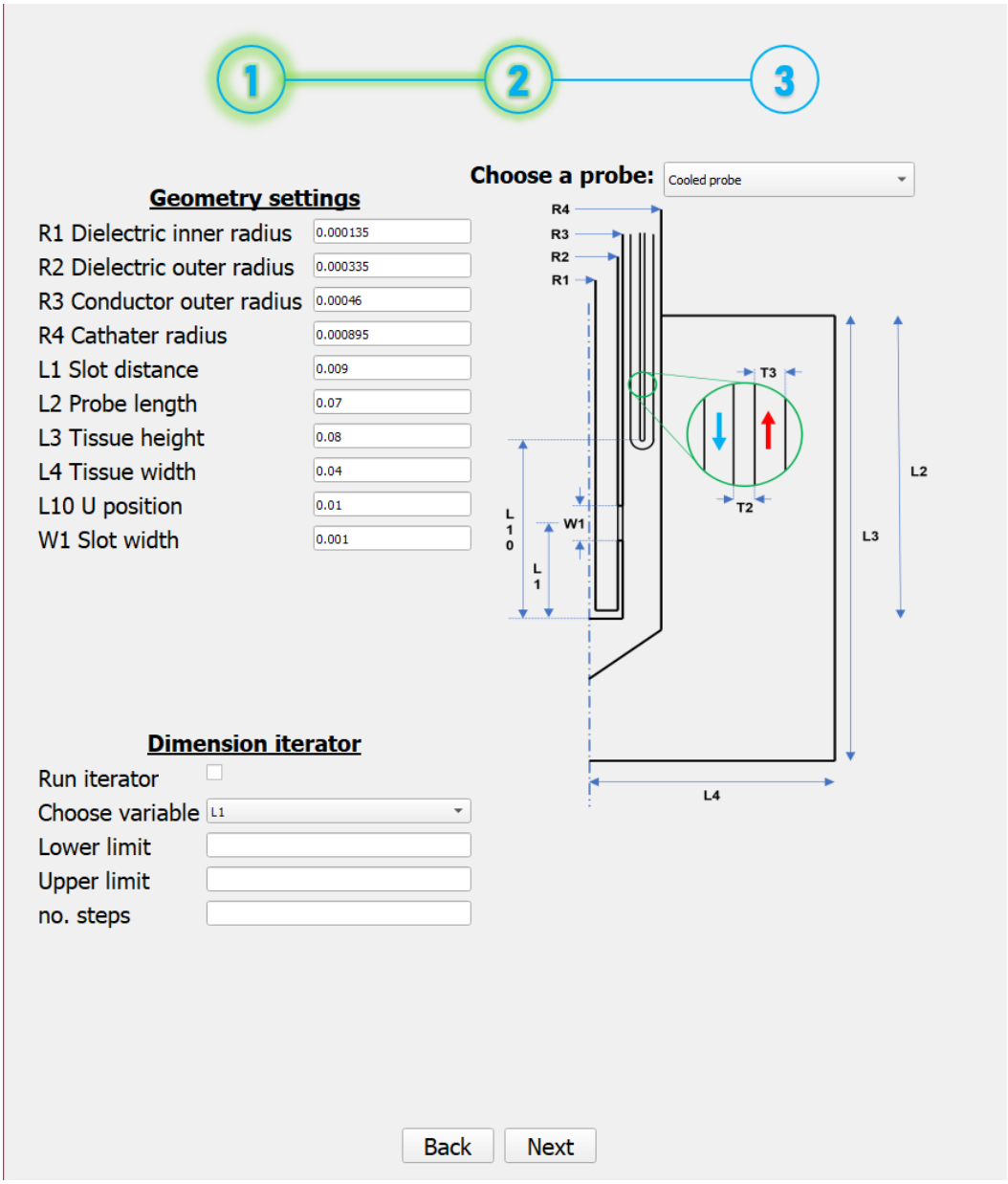

Figure A.9: Page 2 on the GUI with Single slotted probe with internal cooling selected from the library.

The last page of the GUI handles the output of data. Two types of file can be created here, the first is a log file, whose purpose serves to store global data values at each time step in the ablation. Initialised through checking of the ”Save log file” box, the desired data can be checked as seen on the right hand side of Fig A.10. This comprises of the reflection coefficient, general settings, FEM settings, antenna characteristics and shape analysis values.

The second type of file that can be saved take the form of a .vtk containing 2D distributions of various variables computed in the simulation. The possible variables this could be includes the electric field, SAR field, temperature, electrical conductivity, electrical permittivity, and the Alive/Vulnerable/Dead cell fractions. Initialized by checking the ”Save field .vtk files” boex, these files will be saved into the destination of the path entered into the ”Path to folder:” input and with the file handle specified in ”File name template:”. Once complete, the ”Run” button will execute the simulation(s) defined by user inputs.

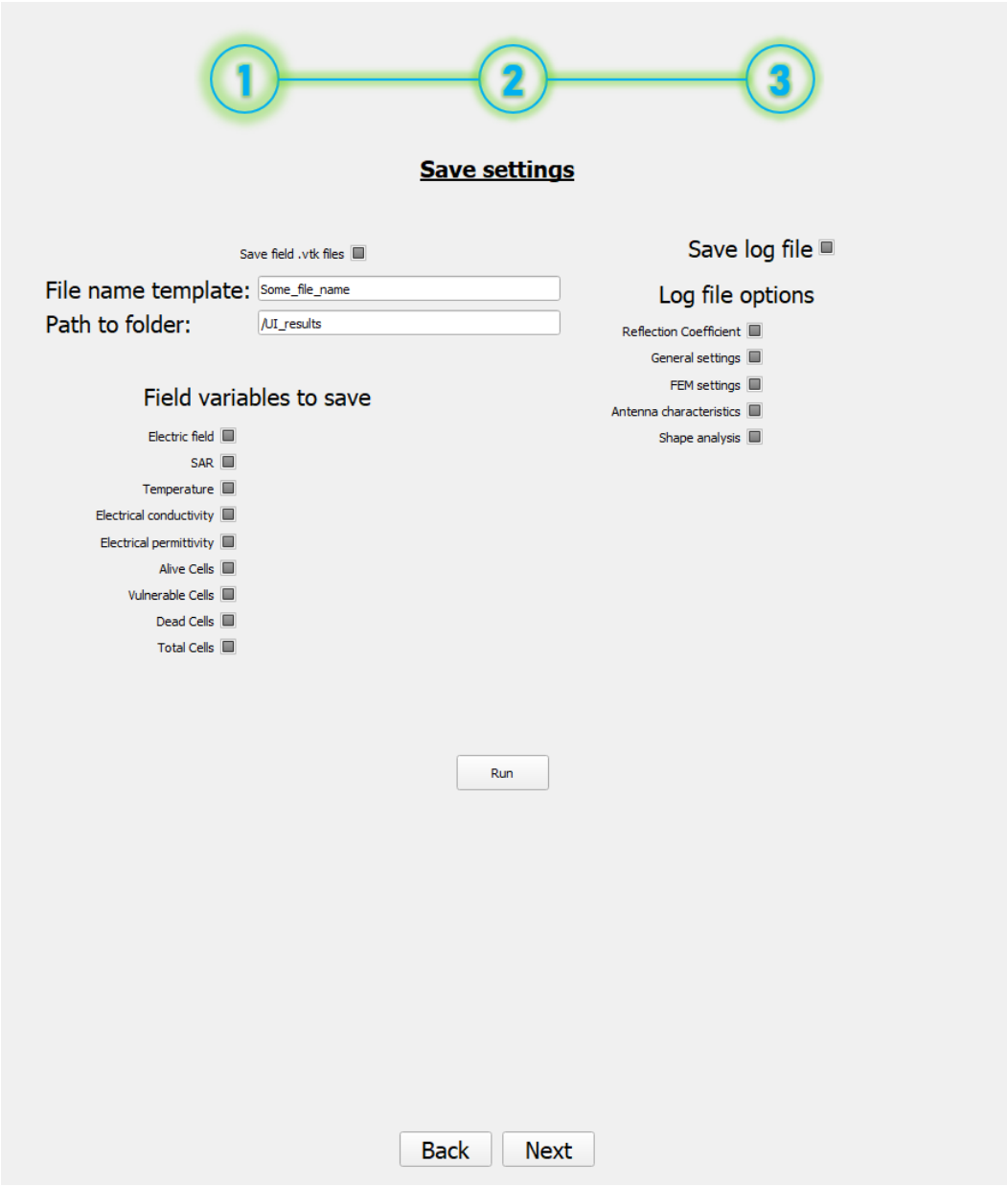

Figure A.10: Page 3 on the GUI, the left column handles file name and location, along with data to be saved into .vtk. On the right are options for setting up a log file for transient measures of global variables.

B Additional weak formulations

B.1 Weak Formulation - Fluid flow

A weak formulation of the problem can be made from the strong form in Eq 6.4. Multiplying by vector test function, $\mathbf{v}$, which vanishes on dirichlet boundaries of the domain, then integrating across subdomain Ψ.

$$\int_{\Psi} \rho(\mathbf{u}\cdot\nabla)\mathbf{u}\cdot\mathbf{v} - \int_{\Psi} \mu\nabla^2\mathbf{u}\cdot\mathbf{v} + \int_{\Psi} p\nabla\cdot\mathbf{v} = \int_{\Omega} \mathbf{f}\cdot\mathbf{v} \tag{B.1}$$

Second and third terms on the LHS can be rewritten using integration by parts and Gauss' theorem

$$\int_{\Omega} \mu\nabla^2\mathbf{u}\cdot\mathbf{v} = -\int_{\Omega} \mu\nabla\mathbf{u}\cdot\nabla\mathbf{v} + \int_{\partial\Omega} \mu\frac{\partial\mathbf{u}}{\partial\hat{\mathbf{n}}}\cdot\mathbf{v} \tag{B.2}$$

$$\int_{\Omega} p\nabla\cdot\mathbf{v} = -\int_{\Omega} p\nabla\cdot\mathbf{v} + \int_{\partial\Omega} p\mathbf{v}\cdot\hat{\mathbf{n}} \tag{B.3}$$

where $\hat{\mathbf{n}}$ is the surface normal vector. Substitution into Eq B.1 yields

$$\int_{\Omega} \rho(\mathbf{u}\cdot\nabla)\mathbf{u}\cdot\mathbf{v} - \int_{\Omega} \mu\nabla\mathbf{u}\cdot\nabla\mathbf{v} - \int_{\Omega} p\nabla\cdot\mathbf{v} = \int_{\Omega} \mathbf{f}\cdot\mathbf{v} + \int_{\partial\Omega} \left(\mu\frac{\partial\mathbf{u}}{\partial\hat{\mathbf{n}}} - p\hat{\mathbf{n}}\right)\cdot\mathbf{v}. \tag{B.4}$$

This should be accompanier by the continuity weak form, using test function q and again integrating across Ω,

$$\int_{\Omega} q\nabla\cdot\mathbf{u} = 0. \tag{B.5}$$

Boundary conditions can be enforced through the surface integral term on the RHS of Eq B.4.

B.1.1 Weak formulation - Heat transfer

Solving Eq 6.11 is approached by using the implicit Euler method, which can be written as

$$\frac{T^{n+1} - T^n}{\nabla t} = \nabla\cdot\left(\frac{k}{\rho C_p}\nabla T^n\right) - \nabla\cdot(\mathbf{u}T^n) + \frac{\sigma}{2\rho C_p}|\mathbf{E}|^2. \tag{B.6}$$

A weak formulation of Eq 6.11 can be made by multiplication by a test function a, and integration across the entire domain Ω. Coefficients can be grouped such that $\gamma = \frac{k}{\rho C_p}$ and $\eta = \frac{\sigma}{2\rho C_p}$.

$$\int_{\Omega} \frac{T^{n+1} - T^n}{\nabla t}a = \int_{\Omega} [\nabla\cdot(\gamma\nabla T^n)]a - \int_{\Omega} \nabla\cdot(\mathbf{u}T^n)a + \int_{\Omega} \eta|\mathbf{E}|^2 a \tag{B.7}$$

The first term on the RHS can be converted from second order to first order through the identity $\nabla \cdot (\phi u) = \phi(\nabla \cdot u) + (\nabla \phi) \cdot u$, which gives

$$\int_{\Omega} [\nabla \cdot (\gamma \nabla T^n)] a = \int_{\Omega} \nabla \cdot [a \, (\gamma \nabla T^n)] - \int_{\Omega} (\nabla \cdot a) \, (\gamma \nabla T^n)]. \tag{B.8}$$

Application of the divergence theorem to the second order term

$$\int_{\Omega} [\nabla \cdot (\gamma \nabla T^n)] a = \int_{\partial \Omega} [a \, (\gamma \nabla T^n)] \cdot \mathbf{n} - \int_{\Omega} (\nabla \cdot a) \, (\gamma \nabla T^n)] \tag{B.9}$$

which can be substituted to give the weak form to be computed

$$\int_{\Omega} \frac{T^{n+1} - T^n}{\nabla t} a = \int_{\partial \Omega} [a \, (\gamma \nabla T^n)] \cdot \mathbf{n} - \int_{\Omega} (\nabla \cdot a) \, (\gamma \nabla T^n)] - \int_{\Omega} \nabla \cdot (\mathbf{u} T^n) a + \int_{\Omega} \eta |\mathbf{E}|^2 a. \tag{B.10}$$